

A Proposal for a Detector 2 km Away From the T2K Neutrino Source

E. Kearns, M. Litos, J. Raaf, J. Stone, L.R. Sulak, J. Bouchez, C. Cavata, M. Fechner, L. Mosca, F. Pierre, et al.

▶ **To cite this version:**

E. Kearns, M. Litos, J. Raaf, J. Stone, L.R. Sulak, et al.. A Proposal for a Detector 2 km Away From the T2K Neutrino Source. 2005, pp.1-85. in2p3-00409176

HAL Id: in2p3-00409176
https://hal.in2p3.fr/in2p3-00409176

Submitted on 6 Aug 2009

HAL is a multi-disciplinary open access archive for the deposit and dissemination of scientific research documents, whether they are published or not. The documents may come from teaching and research institutions in France or abroad, or from public or private research centers.

L'archive ouverte pluridisciplinaire **HAL**, est destinée au dépôt et à la diffusion de documents scientifiques de niveau recherche, publiés ou non, émanant des établissements d'enseignement et de recherche français ou étrangers, des laboratoires publics ou privés.

A Proposal for a Detector 2 km Away From the T2K Neutrino Source

May 30, 2005

Abstract

We propose building a detector site 2km from the neutrino production point of the the T2K experiment. At this distance, almost the same neutrino flux is measured as that seen at Super-K 295 km away. We propose to measure this flux with both a 1 kton water Cherenkov detector which has been optimized to match Super-K resolution, and a 100 ton fiducial volume liquid argon time projection chamber which will provide fine grain imaging and low particle detection thresholds for a precise study of neutrino interactions at the relevant energies. High energy muons which exit the water Cherenkov detector will be measured by an iron muon ranger. In this document, we show that combination of a detector made with the same target as Super-K, with almost the same detector response, and an extremely fine-grained tracking chamber sited in the off-axis beam, will allow us to predict the events seen at Super-K with very little correction other than that of geometric acceptance.

AUTHOR LIST

Boston University (USA): E. Kearns, M. Litos, J. Raaf, J. Stone, L.R. Sulak

CEA Saclay (France): J. Bouchez, C. Cavata, M. Fechner, L. Mosca, F. Pierre, M. Zito

CIEMAT (Spain): I. Gil-Botella, P. Ladrón de Guevara, L. Romero

Columbia University (USA): E. Aprile, K. Giboni, K. Ni, M. Yamashita

Duke University (USA): K. Scholberg, N. Tanimoto, C.W. Walter

ETH Zürich (Switzerland): W. Bachmann, A. Badertscher, M. Baer, Y. Ge, M. Laffranchi, A. Meregaglia, M. Messina, G. Natterer, A. Rubbia

ICRR University of Tokyo (Japan): I. Higuchi, Y. Itow, T. Kajita, K. Kaneyuki, Y. Koshi, M. Miura, S. Moriyama, N. Nakahata, S. Nakayama, T. Namba, K. Okumura, Y. Obayashi, C. Saji, M. Shiozawa, Y. Suzuki, Y. Takeuchi

INFN Sezione di Napoli (Italy): A. Ereditato

Institute of Experimental Physics, Warsaw University, Warszawa (Poland): D. Kiełczewska[1]

H.Niewodniczański Institute of Nuclear Physics, Kraków (Poland): A. Szelc, A. Zalewska

Institute for Nuclear Research RAS (Russia): A. Butkevich, S.P. Mikheyev

A.Sołtan Institute for Nuclear Studies, Warszawa (Poland): P. Przewlocki, E. Rondio

Institute of Physics, University of Silesia, Katowice (Poland): J. Holeczek, J. Kisiel

Laboratori Nazionali di Frascati (LNF) (Italy): G. Mannocchi[2]

Laboratori Nazionali di Gran Sasso (Italy) : O. Palamara

Louisiana State University (USA): S. Dazeley, S. Hatakeyama, R. McNeil, W. Metcalf, R. Svoboda

Università dell'Aquila (Italy): F. Cavanna, G. Piano Mortari

University of California, Irvine (USA): D. Casper, J. Dunmore, S. Mine, H.W. Sobel, W.R. Kropp, M.B. Smy, M.R. Vagins

University of California, Los Angeles (USA): D. Cline, M. Felcini, B. Lisowski, C. Matthey, S. Otwinowski

Université Claude Bernard Lyon-1 (France) : D. Autiero, Y. Declais, J. Marteaux

[1] Also at Univerisity of California, Irvine.
[2] Also at IFSI del CNR, sezione presso LNF.

Universidad de Granada (Spain): A. Bueno, S. Navas-Concha

University of Sheffield (UK): P.K. Lightfoot, N. Spooner

Università di Torino (Italy) : P. Picchi[3]

University of Valencia (Spain): J.J. Cadenas

University of Washington, Seattle (USA): H. Berns, R. Gran, J. Wilkes

Wrocław University, Wrocław (Poland): J. Sobczyk

Yale University (USA): A. Curioni, B.T. Fleming

[3]Also at Laboratori Nazionali di Frascati (LNF), INFN, Frascati, Italy and IFSI del CNR sezione presso LNF.

Contents

1 Project Description **6**

2 Physics Goals of the J-PARC Neutrino Project **7**
2.1 Introduction . . . 7
2.2 Searching for ν_e Appearance . . . 7
2.3 The T2K Experiment . . . 8

3 The Neutrino Beam at J-PARC **11**

4 The Far Detector **12**
4.1 Super-Kamiokande . . . 12

5 Motivation for the 2KM Detector **13**

6 Overview of the Laboratory Facility **16**

7 Water Cherenkov Detector **21**
7.1 1 kton Enclosure and Substructure . . . 21
7.2 Water Purification System . . . 22
7.2.1 The primary filling system . . . 22
7.2.2 Recirculation . . . 22
7.2.3 Temperature control . . . 22
7.2.4 Logistics . . . 22
7.3 Photomultiplier Tubes . . . 23
7.4 Electronics for the Water Cherenkov Detector . . . 23
7.4.1 Water Cherenkov High Voltage System . . . 23
7.4.2 Water Cherenkov Signal Electronics and DAQ . . . 24
7.4.3 Event Time Synchronization . . . 24
7.5 Calibration Systems . . . 25

8 The Liquid Argon Detector and its Infrastructure **27**
8.1 Introduction . . . 27
8.2 The liquid argon cryostat . . . 29
8.2.1 The cryostat . . . 29
8.2.2 The inner target . . . 31
8.3 Liquid argon process . . . 32
8.3.1 Initial cooling and refrigeration . . . 32
8.3.2 Vacuum and liquid argon purification . . . 33
8.4 Liquid argon monitoring . . . 34
8.4.1 Liquid argon purity monitors . . . 34
8.4.2 UV laser calibration . . . 34
8.5 Inner detector . . . 34
8.5.1 Mechanical structure and TPC wire planes . . . 34
8.6 Light read-out system . . . 37
8.6.1 Scintillation light . . . 37
8.7 High voltage system . . . 37
8.8 Read-out electronics . . . 38

9 Muon Range Detector **40**
9.1 Overall Design . . . 40
9.2 Scintillator Detector . . . 40
9.3 Readout Electronics . . . 41

10 The 2KM Detector Simulation and Performace **42**
10.1 Water Cherenkov Simulation Results . . . 42
10.1.1 Validation and Initial Tuning using K2K 1kton Data . . . 42
10.1.2 Selection of a Configuration to Match Super-Kamiokande Resolution . . . 43
10.1.3 Event Reconstruction Performance with Selected Configuration . . . 45
10.2 Liquid Argon Simulation Results . . . 46
10.2.1 Hit, cluster and track reconstruction . . . 46
10.2.2 e/π^0 separation . . . 46
10.2.3 Hadron identification . . . 47
10.2.4 Event reconstruction, selection and classification . . . 47
10.2.5 Muon momentum resolution . . . 56
10.2.6 Neutrino and hadron energy resolution . . . 58
10.2.7 Event Kinematics Reconstruction . . . 58
10.2.8 Events in the Inner Target . . . 61
10.3 Muon Ranger Simulation Results . . . 61
10.3.1 MRD Simulation . . . 63
10.3.2 MRD Track and Energy Reconstruction . . . 63
10.3.3 Combined WC/MRD Acceptance and Resolution . . . 64

11 Physics with the Intermediate Detector **66**
11.1 Measurement of the Background for ν_e Appearance . . . 66
11.1.1 Neutral Current π^0 Backgrounds . . . 67
11.1.2 Intrinsic Beam Electron Neutrinos . . . 68
11.1.3 Misidentified Charged Current Background . . . 69
11.1.4 Prediction of the Background for ν_e Appearance at Super-K using the 2km detector. 69
11.2 Measurement of the ν_μ Neutrino Spectrum . . . 74
11.3 Physics in the 2nd Phase T2K Experiment with the 2KM Detector . . . 75

A Schedule **79**

B Budget **81**
B.1 Facilities and Civil Construction . . . 81
B.2 Water Cherenkov Detector . . . 81
B.2.1 Water Enclosure and Mechanical Support . . . 81
B.2.2 PMTs and Cables . . . 82
B.2.3 Water System . . . 82
B.2.4 Water Cherenkov HV System and Readout Electronics . . . 83
B.2.5 GPS System . . . 83
B.3 Muon Range Detector . . . 84
B.3.1 MRD Steel and support structure costs . . . 84
B.3.2 MRD Detector Costs . . . 84
B.4 Liquid Argon Detector . . . 84
B.5 Total Project Cost . . . 85

1 Project Description

The T2K experiment (Tokai-to-Kamioka) is a long baseline neutrino oscillation experiment that will measure several parameters that describe neutrino mixing at the scale set by atmospheric neutrino oscillation. These include precision measurements of Δm^2_{23}, θ_{23}, and most importantly, θ_{13}. From reactor experiments such as Chooz and Palo Verde, we believe θ_{13} to be fairly small (less than $\sim 12^\circ$), which implies that electron neutrino appearance will be a statistically small effect. On the other hand, θ_{23} is known to be nearly maximal, and it is of great theoretical interest to measure a small difference from $\pi/2$. For both cases, the T2K experiment requires detailed understanding of systematic effects.

The T2K experiment utilizes a high intensity beam being constructed at the J-PARC facility in Tokai. The far detector is Super-Kamiokande, a 50 kton water Cherenkov detector with 11,000 photomultiplier tubes, 295 km distant. For $\Delta m^2 \sim 2.5$ eV^2, the maximum oscillation effect is at a neutrino energy of 0.6 GeV. Unlike previous long-baseline experiments, T2K will use the off-axis technique to produce a sharp peak in the energy spectrum of neutrinos at the critical energy. This will maximize the signatures for the disappearance of muon neutrinos and the appearance of electron neutrinos.

To best cancel systematic uncertainties, it is desirable to measure the neutrino beam with the same type of detector near the neutrino production point before neutrino oscillations have taken place. Considering the case of a water Cherenkov detector, we find that the minimum size is set by the length needed to contain muons produced by ~ 1 GeV neutrinos, and corresponds to a volume weighing approximately 1 kton. This size also readily contains the important event categories of intrinsic beam ν_e and neutral current single-π^0. For this size, we will have one event or fewer in the water volume for every pulse of the accelerator.

Both the neutrino flux and energy spectrum change as one moves further from the beam axis. At a distance of 295 km, the far detector will sample a very narrow interval of the beam profile. A detector at 2 km will sample a somewhat larger, but very similar interval of the neutrino profile, in contrast to a detector located very near, on the J-PARC site. Therefore, the event rates measured at 2 km can be simply extrapolated to the Super-K site with little more than geometrical factors, without the need for a Monte Carlo correction for neutrino production.

A valuable event category at these energies are two-prong quasi-elastic scatters with both μ and p reconstructed in the final state. This allows a precise measurement of neutrino energy, and allows us to isolate a non-quasi-elastic sample that contributes to the background for θ_{23}. To record these events, it is also necessary to have a fine-grained detector that is sensitive to tracks which might not be seen in a water Cherenkov detector. For this purpose, we propose to include a large (150 ton) liquid argon TPC with an embedded frozen water target. Such a detector will record 200,000 events per year, affording unprecedented detail in the study of the complicated region of $E_\nu \sim 1$ GeV, where resonant pion production is significant, where the hadronic part cannot be calculated perturbatively, and where nuclear effects are important.

Finally, there is important information in the high energy tail of the neutrino spectrum. For example, the highest energy neutrinos come from the kaon component of the beam, which is also the dominant source of intrinsic beam ν_e. High energy muons exit the water Cherenkov detector, but we will measure them with a downstream muon range stack. High energy events will also be detected with high efficiency in the liquid argon detector. In this case, the high energy muons escaping the liquid argon volume can still be detected and measured in the Water Cherenkov detector.

This 2 km detector complex will be located off of the J-PARC site near the small village of Tokai. The facility to be built would extend $\sim$50 m below ground level to reach the proper position in the neutrino beam at that location. Environmental studies and sample core drilling have already been conducted and have confirmed the suitability of the chosen site. The local government, which owns the property, approved the proposed facility and granted use of the property at no cost to the experiment.

2 Physics Goals of the J-PARC Neutrino Project

2.1 Introduction

There is now a strong consensus in the neutrino physics community that neutrinos have mass and their flavor states mix with each other. Strong evidence exists from atmospheric neutrinos [1], solar neutrinos [2, 3], reactor experiments [4], and long baseline oscillation experiments [5].

The next generation of experiments must take the step towards making precision measurements of the neutrino parameters that are already known, and attempting to measure effects that have not yet been seen, because the values of the parameters that govern them are either zero or too small.

At this point in time all of the confirmed neutrino oscillation results have been measurements of neutrino disappearance. Electron neutrino appearance is an as yet unobserved aspect of neutrino oscillation; in addition, if interpreted in a three neutrino oscillation framework, the observation of electron neutrino appearance would mean that more refined measurements could explore CP violation in the lepton sector using neutrinos.

An intriguing possibility is that the origin of neutrino mass can be explained by physics of the highest energy scales which existed in the the early universe. In consequence, neutrinos may hold the imprint of actions in the beginning of our universe that determined the properties we observe today. Foremost among the questions is "Why does there seem to be more matter in our universe than anti-matter?"

It should be noted that there is one previously claimed observation of $\bar{\nu}_e$ appearance by the LSND [6] collaboration at Los Alamos. Presently, the MiniBooNE [7] experiment at Fermilab is attempting to either confirm or rule out this claim. No matter what the outcome of this important experiment, T2K will still be important. If MiniBooNE confirms the LSND result then our simple model of three-flavor mixing will be hard to reconcile with data and we may expect surprises when we run with a new more powerful beam.

2.2 Searching for ν_e Appearance

In a two-flavor framework, the probability that a neutrino transforms into another flavor by the time it has traveled a distance L, if it has an energy E, is given by:

$$P(\nu_a \rightarrow \nu_b) = \sin^2 2\theta \sin^2 \Big(\frac{1.27\Delta m^2(\mathrm{eV}^2)L(\mathrm{km})}{E_\nu(\mathrm{GeV})}\Big), \tag{1}$$

where θ is the mixing angle between the mass basis and the observed weak basis and Δm^2 is the difference of the squared masses of the mass states.

The oscillations of atmospheric ν_μ and solar ν_e can be explained separately by considering each as a two neutrino system. However, both phenomena can be explained together if we consider a 3 neutrino mass system. The relationship between the flavor and mass states of the neutrinos can be expressed with the following matrix equation:

$$\begin{pmatrix} \nu_e \\ \nu_\mu \\ \nu_\tau \end{pmatrix} = \begin{pmatrix} \mathrm{U_{e1}} & \mathrm{U_{e2}} & \mathrm{U_{e3}} \\ \mathrm{U_{\mu 1}} & \mathrm{U_{\mu 2}} & \mathrm{U_{\mu 3}} \\ \mathrm{U_{\tau 1}} & \mathrm{U_{\tau 2}} & \mathrm{U_{\tau 3}} \end{pmatrix} \begin{pmatrix} \nu_1 \\ \nu_2 \\ \nu_3 \end{pmatrix}, \tag{2}$$

where the probability for a transition from flavor a to flavor b is given by:

$$\begin{aligned} P(\nu_a \rightarrow \nu_b) = \quad \delta_{ab} \quad & -4\sum_{j>i} \mathrm{Re}(\mathrm{U^*_{ai}U_{bi}U_{aj}U^*_{bj}}) \sin^2(1.27\Delta \mathrm{m^2_{ij}L/E}) \\ & \pm 2\sum_{j>i} \mathrm{Im}(\mathrm{U^*_{ai}U_{bi}U_{aj}U^*_{bj}}) \sin^2(2.54\Delta \mathrm{m^2_{ij}L/E}). \end{aligned} \tag{3}$$

with L in km, E in GeV, and Δm^2 in eV^2. The minus sign refers to neutrinos and the plus sign to antineutrinos. Equation 1 is a limiting case of this formula for considering only a single Δm^2 between the two states.

With three neutrino masses there are two neutrino masses differences(Δm^2_{12}, Δm^2_{23}), three mixing angles(θ_{13}, θ_{23}, θ_{12}) and one CP-violating phase. From our current understanding of atmospheric and solar oscillation, if we accept this model, we know the two mass differences, and two of the mixing angles. The 3×3 matrix from Eqn. 2 can be expressed in terms of these angles and mass differences as:

$$\mathrm{U} = \begin{pmatrix} 1 & 0 & 0 \\ 0 & c_{23} & s_{23} \\ 0 & -s_{23} & c_{23} \end{pmatrix} \begin{pmatrix} c_{13} & 0 & s_{13}e^{i\delta} \\ 0 & 1 & 0 \\ -s_{13}e^{i\delta} & 0 & c_{13} \end{pmatrix} \begin{pmatrix} c_{12} & s_{12} & 0 \\ -s_{12} & c_{12} & 0 \\ 0 & 0 & 1 \end{pmatrix} \tag{4}$$

where "s" represents the sine of each mixing angle and "c" represents the cosine. In the decomposition above, the disappearance of solar neutrinos is driven by the oscillations of the 1-2 mass states which are mixed by the two dimensional sub-matrix with the θ_{12} terms, and observed atmospheric disappearance is driven by the matrix with the θ_{23} terms. The central mixing matrix, which contains θ_{13} mixing angles, will cause ν_e to appear in a ν_μ beam, and thus by searching for ν_e appearance we can hope to measure this angle. It should be noted that δ in this equation will cause CP violation, which also modifies the the ν_e appearance probability. Because of this degeneracy, a measurement of ν_e appearance must be interpreted as a joint limit on both of these variables [8].

The most pressing question in neutrino physics at this moment is whether the third unknown mixing angle is non-zero. If it is non-zero, we must measure its value. In addition to telling us whether we have a chance to measure CP violation in the neutrino sector, filling in this last piece of the mixing angle puzzle we will give an important constraint to theorists who are trying to make sense of the existing data. We know now that for at least two of the mixing angles, neutrino mixing seems to be relatively large. This is in marked contrast to the case of quarks, where the mixing angles are small [9]. Also we know that both the mass splittings and the absolute masses of neutrinos are very small compared to those of most other fundamental particles.

These questions have profound importance not only for the field of neutrino physics but also for the larger field of physics and cosmology. Theoretical attempts to explain why the neutrino masses are so small and their mixings are large often rely on physics at the GUT scale (for a recent review see [10]). One of the most popular ideas, known as the see-saw mechanism [11, 12], coupled with CP violation in neutrinos produces leptogenesis [13], where a lepton matter/antimatter asymmetry caused by the decay of heavy neutrinos is converted into a baryon asymmetry. This could explain why today we live in a matter-dominated universe. Ideally, we would like a single theory which explains both the mass of neutrinos and size of their mixings at the same time. T2K's role in meeting this goal will be measurements of both the mass splittings and mixing angles.

2.3 The T2K Experiment

The Tokai to Kamioka (T2K) experiment is the second generation accelerator based neutrino oscillation experiment involving Super-K. The first long-baseline experiment K2K [14] produced neutrinos of 1 GeV and measured them both near the production point and at Super-K on the opposite side of Japan. T2K, like K2K, will use Super-K as the target, but it will use the new 50 GeV proton synchrotron at the J-PARC accelerator complex located in Tokai, Japan for its neutrino source. T2K has a neutrino beam which is on the order of 100 times as powerful as the K2K beam. The distance from Tokai to Kamioka is 295 km. The first beam of the T2K experiment is expected in 2009.

T2K is one of a set of new long-baseline neutrino experiments that will become operational in the near future. For example, the NOνA [15] experiment proposes to use a longer baseline and higher energy to probe the same region of oscillation space. T2K and NOνA are complementary experiments. Not only do they use different detector technologies (water Cherenkov in the case of T2K, and a low Z segmented calorimeter in



Figure 1: The T2K experiment will direct a neutrino beam 295 kilometers across Japan from Tokai to Kamioka.

the case of NOνA), but the differences in baseline for the two experiments will help disentangle the effects of CP violation and matter effects in neutrino oscillation [16].

Unlike K2K, for which the neutrino beam was pointed directly at Super-K, in T2K the beam will be pointed about 2° away from Super-K. This so-called "off-axis" technique was first proposed in the Brookhaven long-baseline proposal(E889) [17]. The method takes advantage of the kinematics of pion decay to make a narrow energy band neutrino beam with the peak energy set by the off-axis angle that is chosen. The narrow band is important because it increases the flux at the oscillation maximum, maximizing the appearance signal.

The appearance signal events in T2K are interactions with a single showering Cherenkov ring and no decay electrons. The energy is reconstructed assuming quasi-elastic two-body kinematics. An excess of events over the expected background is the signal for ν_e appearance. See Fig. 53 later in this document for the expected signal for $\Delta m^2_{23} = 3 \times 10^{-3}$ eV^2. Backgrounds such as misidentified neutral current single π^0's that are incorrectly identified as electrons may arise, if both of the γ s from the π^0 decay are not reconstructed. This occurs predominantly at higher neutrino energy than the oscillation maximum, but the narrow band reduces the high energy tail, which suppresses this source of background.

The main goals of the T2K experiment are:

- to observe ν_e appearance in an oscillation experiment for the first time,
- to measure θ_{13} or improve the limit by a factor of 10 to 20,
- measure θ_{23} to better than the few percent level, perhaps resolving if it is truly maximal or not, and
- to continue to refine the precision measurements of Δm^2_{23} begun by Super-K and MINOS.

Figure 2 shows the expected sensitivity of the experiment to θ_{13} compared with the present best limit, set by the CHOOZ [18] reactor experiment. Figure 3 taken from the T2K LOI [19] shows expected sensitivities for different values of Δm^2_{23}.

The value of θ_{23} is of particular interest. Our current knowledge from Super-K tells us that $\sin^2 2\theta_{23}$ is consistent with unity but could be as small as 0.95. If the value is unity this corresponds to a mixing angle of 45°, which is an exactly equal mixture of mass states known as "maximal mixing." Maximal mixing

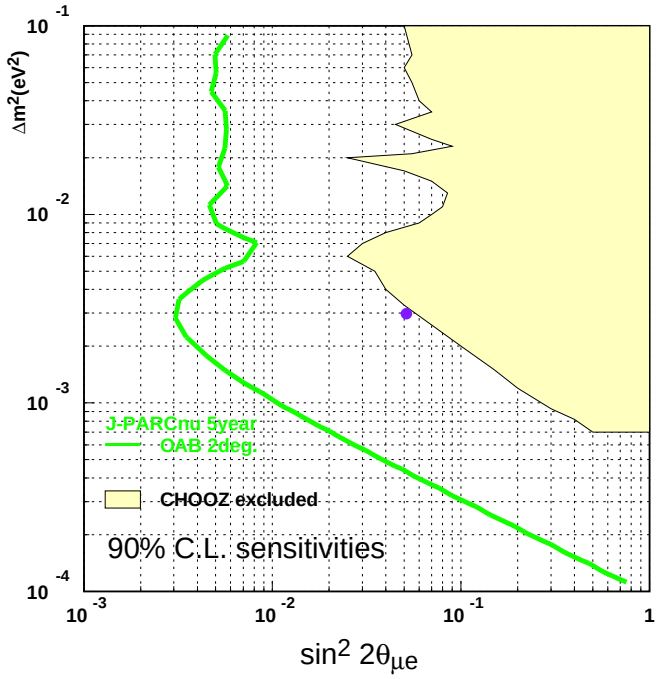


Figure 2: The current and expected limits on θ_{13} by T2K as a function of Δm^2_{23}. Note: $\sin^2(2\theta_{\mu e}) = \frac{1}{2}\sin^2(2\theta_{13})$ for maximal mixing.

may imply a underlying symmetry, which is why one of the major goals of the experiment is to measure θ_{23} to high enough precision to distinguish maximal and nearly maximal mixing.

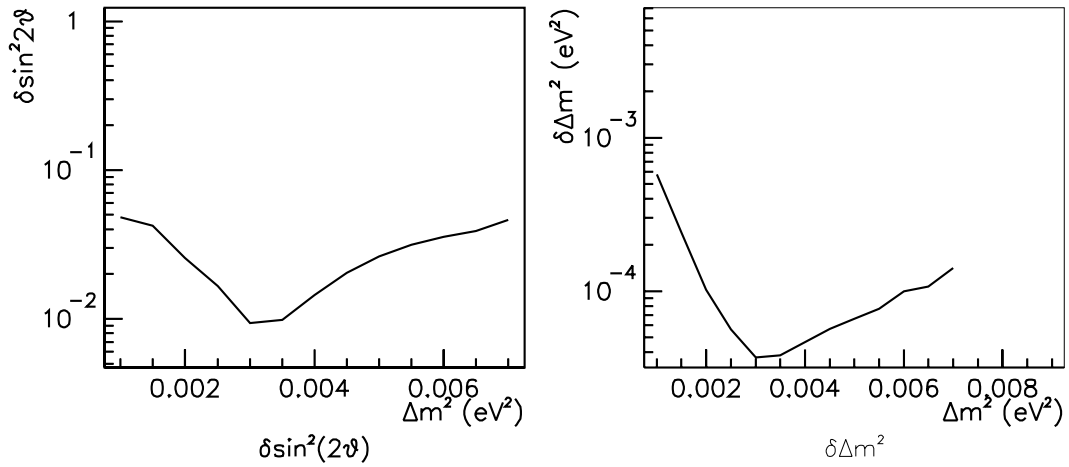


Figure 3: T2K's expected fractional sensitivity to $\sin^2(2\theta_{23})$ and Δm^2_{23} as a function of Δm^2_{23} from the T2K LOI [19].

3 The Neutrino Beam at J-PARC

The T2K neutrino beam is produced by the J-PARC [19] 50 GeV proton synchrotron (PS). A 3 GeV PS is fed by a 400 MeV linac, which then feeds the 50 GeV PS. After the protons are accelerated to 50 GeV they are transported to a graphite target by 20 normal and 28 combined-function super-conducting magnets. The cooled graphite target is located in the first of three magnetic focusing horns. The pions and kaons that are produced in the proton-graphite reaction are focused into a beam before entering a 130 m helium-filled decay region. The neutrinos produced by the decay of these pions travel 295 km across Japan to Super-K. The J-PARC site layout is shown schematically in Fig. 4.

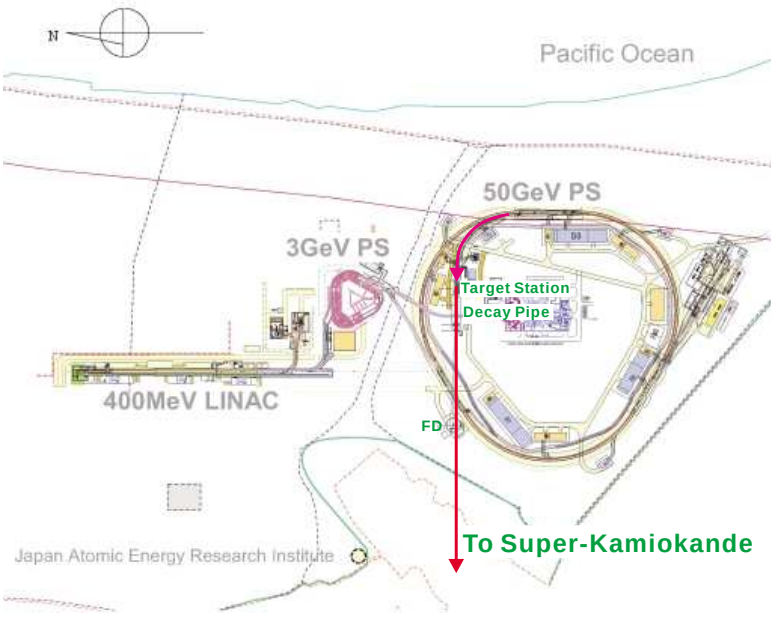


Figure 4: A schematic layout of the J-PARC accelerator complex used to produce the T2K neutrino beam from the T2K LOI [19].

There is one spill producing neutrinos every 3.53 seconds; each spills lasts for 5 μs. A spill is divided into 8 bunches each of which lasts for 58 ns. The beam produced in the decay pipe is primarily a ν_μ beam with a predicted ν_e contamination of $\sim 0.4\%$ at the ν_μ flux peak at Super-K. Fig. 5 shows the expected neutrino flux.

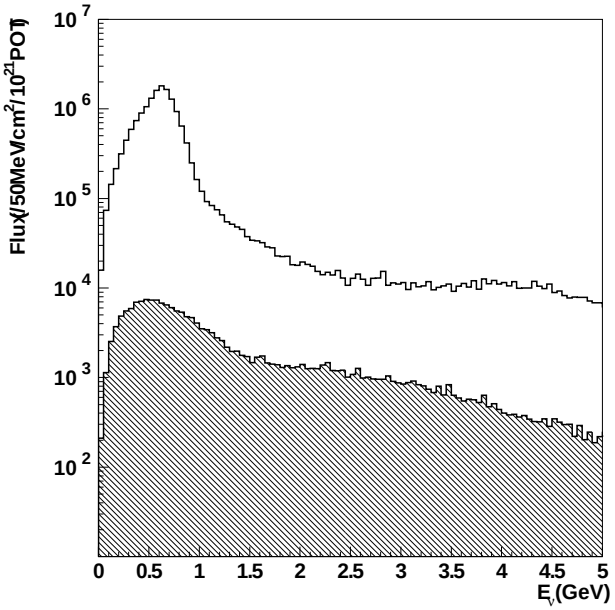


Figure 5: The expected neutrino spectrum of the T2K beam. The open histogram is the ν_μ flux and the hatched histogram is ν_e flux. At the ν_μ peak the ν_e flux is $\sim 0.4\%$ of the ν_μ flux at Super-K.

4 The Far Detector

4.1 Super-Kamiokande

As the K2K experiment did, the T2K experiment utilizes Super-K as the far detector of the neutrino beam. Super-K is a 50 kiloton water Cherenkov detector sensitive to naturally produced neutrinos from nuclear reactions in the sun and interactions of primary cosmic rays in the upper atmosphere. The response of Super-K to to both ν_μ and ν_e neutrinos of 1 GeV has been well studied with both atmospheric neutrinos and the K2K beam. The Super-K detector is described in detail in in reference [20].

There have been two phases of SK running. The first phase, Super-K I, from 1996 to 2001, produced important solar and atmospheric neutrino physics results and set stringent limits on proton decay. In November of 2001, a photomultiplier tube (PMT) imploded, causing a chain reaction which destroyed a large number of PMTs. In a period of about one year the collaboration rebuilt Super-K with one half PMT density in the inner detector, and completely refurbished the outer detector. Super-K II has been running since early 2003. In 2005 and 2006 Super-K will be restored to original PMT density to prepare for the upcoming T2K run. When T2K begins, we will need all of the Super-K PMTs in order to attain full capability for distinguishing ν_e from background.

5 Motivation for the 2KM Detector

As described in the introduction, T2K is an off-axis experiment, which is specifically designed to select a narrow energy band by exploiting the change in energy spectrum as a function of angle from the central beam axis. Since the part of the neutrino beam measured by Super-K is only a small portion of the entire beam, the neutrino energy spectrum seen at Super-K is quite different from the energy spectrum of the entire beam. Even along the off-axis angle, the finite size of any detector subtends a different fraction of the entire beam depending on the size of the detector and the distance from the production point. This is demonstrated by Fig. 6 which compares the neutrino beam spectrum 2 degress off-axis for the anticipated detectors at 280 m, at approximately 2 km, and at 295 km. Even though the proposed detector at 2 km subtends a 30× larger solid angle than Super-K at 295 km, it is distant enough so that the neutrino energy spectra at 2KM and Super-K are similar in shape.

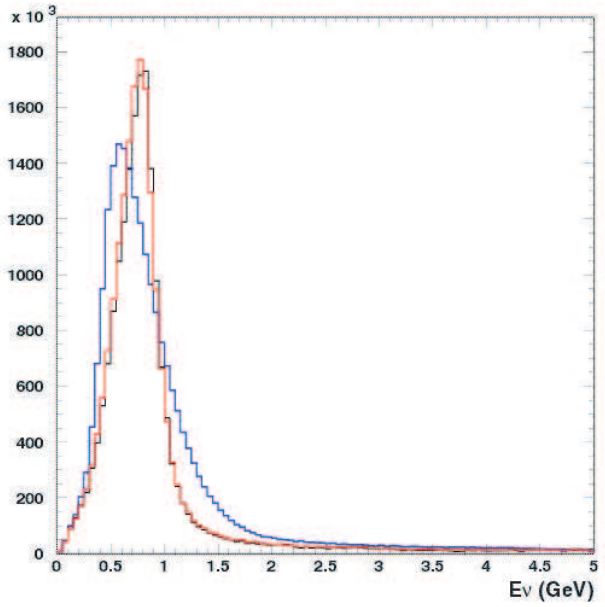


Figure 6: The expected T2K neutrino flux at 280 m(blue line), 2km(red line), and SK(black) line.

Measuring the neutrino spectrum before oscillations so as to predict what will be seen at Super-K is important to the search for ν_e appearance. The background for the ν_e search comes from both electron neutrinos that are intrinsically in the beam at production and misidentified events at Super-K that were produced by NC and ν_μ CC interactions. Therefore, in order to maximize the potential of the experiment it is important to measure carefully the expected neutrino spectrum for both ν_μ and ν_e in a place where the spectrum is as similar to that at Super-K as possible.

The differences in flux as measured at 280 m and 295 km can be seen more clearly by looking at the ratio of near ν_μ flux to far flux (N/F ratio) as a function of energy. The left and right panels of Fig. 7 show this ratio at 280 m and 2 km respectively. Because the energy of peak positions are shifted at 280 m relative to that at Super-K the N/F ratio changes drastically exactly in the region of the oscillation maximum. On the other hand, we can see that by moving to about 2 km, the N/F ratio is flat to about 2%.

There will be a set of detectors built 280 m from the neutrino source. The profile and properties of the beam near the target will be measured there. Super-K is a water Cherenkov device, and we would like to have a similar detector to measure the neutrinos before they have a chance to oscillate. However, the high

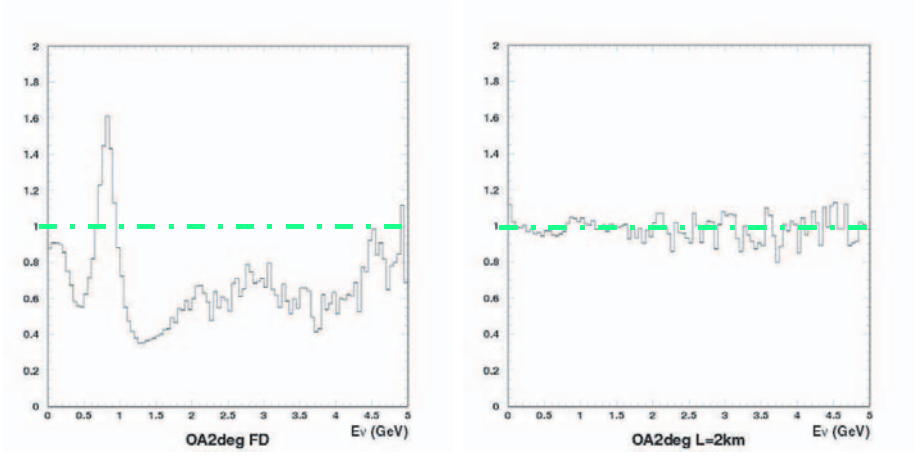


Figure 7: (left) The near/far neutrino flux ratio as a function of energy 280 m from the T2K target. (right) The near/far neutrino flux ratio as a function of energy 2 km from the T2K target.

event rate at 280 m makes this location unsuitable for an unsegmented water Cherenkov detector, due to event overlap. On the other hand, the event rate 2 km from the neutrino source is low enough that we can build a large unsegmented water Cherenkov detector. The size of the water Cherenkov detector is driven by two factors. First of all, we want to contain most muons which interact inside the fiducial volume. At the same time the detector must not be so large that there is more than one neutrino interaction per spill on average. At 2 km this sets a size of approximately 13 m with a 9 m diameter and a 100 ton fiducial volume.

To measure any neutrinos that leave the water detector, and to better match the acceptance of Super-Kamiokande, we will have a muon ranger. The muon ranger must be large enough to contain almost all of the high energy muons produced in the water Cherenkov detector that escape, and must cover enough of the solid angle to intersect most of those muons.

We wish to measure both quasi-elastic (QE) and non-quasi-elastic (non-QE) neutrino interactions at 2 km since the non-QE interactions serve as a source of background to both the ν_e appearance and ν_μ disappearance searches. The more finely-grained and low-energy threshold the detector, the better we can measure pions and other particles produced in non-QE interactions and characterize both the intrinsic ν_e in the beam and misidentified ν_e background. For this reason we are also proposing to build a liquid argon TPC.

The event and particle identification in the liquid argon detector gives clean e/μ and e/π^0 separation with an unbiased reconstruction. This will provide an independent measurement of the ν_e contamination, well separated from the π^0 background. Combined with the NC background, it will yield independent and separated ν_e and π^0 background components at the far detector. It will also be possible to measure the background for ν_e CC at high energy with high efficiency to provide an independent normalization of the background at lower energies where the oscillation signal is expected. For the muon neutrino disappearance search, the good muon identification makes the selected sample very clean; the reconstruction will be unbiased. The low momentum detection threshold in LAr compared to water Cherenkov allows for an independent classification and measurement of event samples in the GeV region. This will provide independent systematic on the non-QE/QE ratio and on the energy scale.

Since the energy spectrum measured by the water Cherenkov detector is based only on the outgoing muon, the final determination of the oscillation parameters is limited by systematic errors arising from the lack of knowledge of all the details of the neutrino interactions. The bubble-chamber-like imaging of the events will permit the study of these neutrino interactions with high quality and, given the flux and the large mass, with high statistics. This sample of events will allow the study of the deep inelastic scattering

and resonance modeling, quasi-elastic modeling including interaction form factors, and the study of nuclear effects such as binding, Fermi-motion, Pauli exclusion, NN-correlations, PDF modifications, rescattering, *etc.*

For the reasons outlined above, we propose to build a detector complex 2 km away from the neutrino source. The detectors will include a water Cherenkov detector which is the same target material as Super-K in order to cancel the neutrino interaction effects, a liquid argon tracking detector and a muon ranger. 2 km was chosen as the distance by optimizing for the measured event rate and the similarity of the near/far fluxes. Fig. 8 shows a perspective representation of the 2KM detector complex.

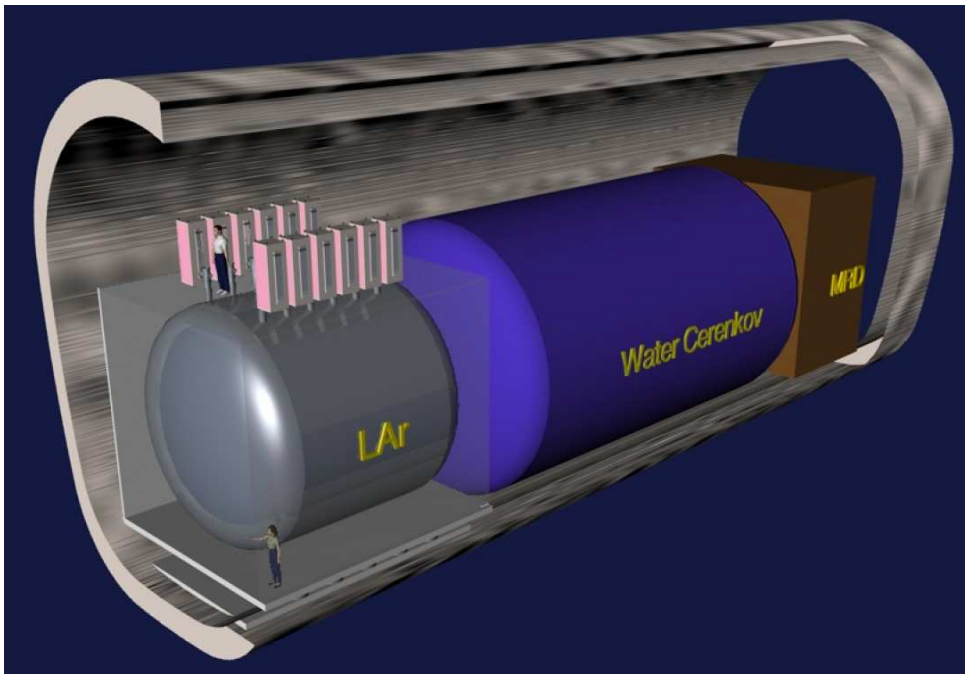


Figure 8: A schematic view of the 2KM detector complex composed of a liquid argon TPC, a water Cherenkov Detector and a muon ranger.

6 Overview of the Laboratory Facility

As with K2K, we propose to build a detector complex with a water Cherenkov detector, a fine-grained detector to measure both the QE and non-QE interactions, and a muon ranger. This detector complex must be located on the line that connects between the production target and the far detector. At about 2 km from the target, the center of the detectors must be more than 40 m below the surface. Therefore, the laboratory facility must be constructed underground, in addition to relevant surface facilities. We searched for a candidate site for this laboratory facility, and found one 1.84 km down stream from the target. (However, the candidate site is actually not on the line that connects the target and the Super-K detector. Because of the off-axis beam, the center of the beam is directed 3.0 to 4.1 degrees below the horizon and 0.75 degrees south of the projected direction to Super-K: see Figure 62. This facility is located 1.5 degrees south of the Super-K direction. Since the beam is expected to be left-right symmetric, we expect the same flux as that in Super-K. The left-right symmetry of the flux must be monitored by the detector at 280 m from the target.) Fig. 9 shows the map near J-PARC. The candidate site is located 1.84 km down stream from the target. This place is owned by the local government (Tokai-village). We had many discussions with Tokai-village, and in 2003, Tokai-village agreed to provide this place to this experiment without any cost.

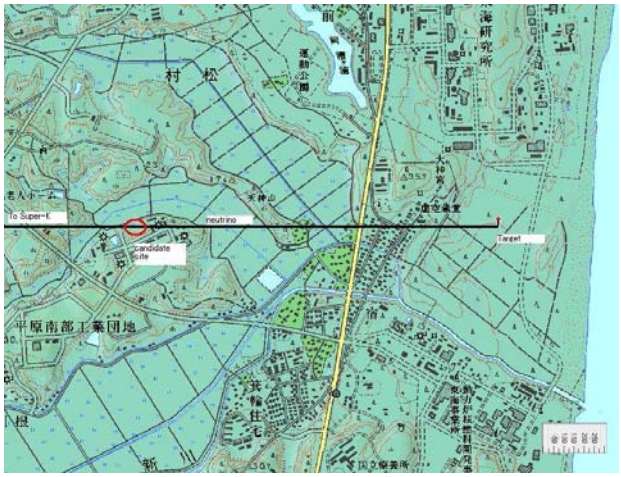


Figure 9: A map near the J-PARC accelerator facility and the candidate 2 km detector facility. The horizontal black line near the center shows the line that connects the target and the far detector. The candidate site is shown by a red circle. It is located 1.84 km from the target.

Figure 10 shows the details of the site owned by Tokai-village. The layout of the surface and the underground facilities are also shown.

In order to design the underground facility and to estimate its cost, it is necessary to know the condition of the underground soil. For this reason, in 2003 we carried out a boring measurement at the site down to 65 m from the surface. The soil is not hard down to 7.5 m from the surface. However, below this level, the soil is hard enough to excavate the underground facility. The underground facility was designed based on these data.

For cost reasons, the size of the experimental hall must not be larger than absolutely necessary. We have also used this as a constraint in our design studies. Figure 11 and 12 shows a completely designed and costed experimental hall. The floor where the neutrino detectors are installed is located 56.27 m below the surface. The center of the neutrino detectors is 51.62 m below the surface. The underground cavity is approximately 34.5 m long, 9.3 m wide and 14 m high. The liquid argon TPC, the water Cherenkov detector and the muon range detector, will be installed in this underground cavity from the up-stream to

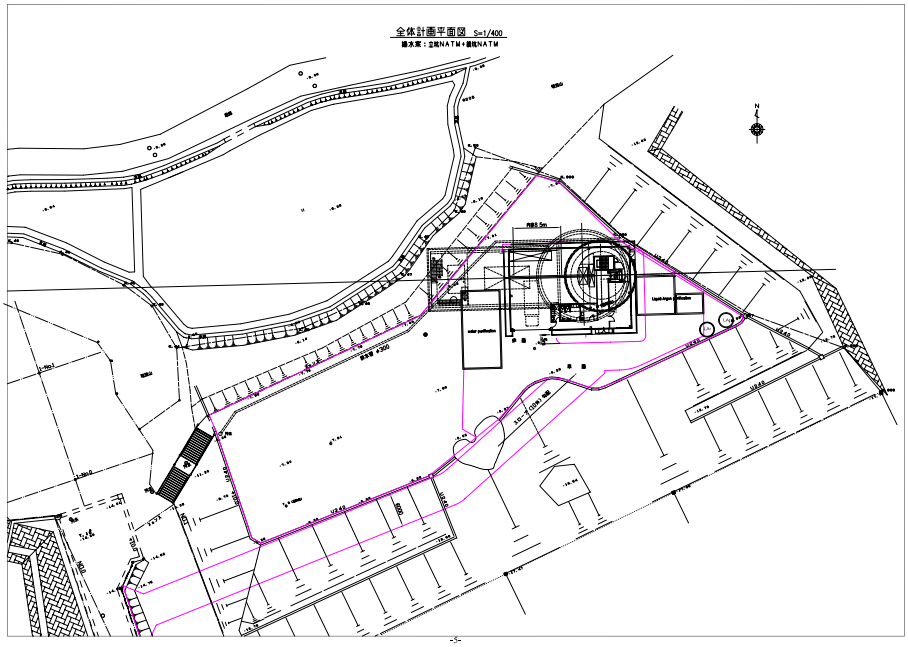


Figure 10: A map near the intermediate detector facility. The area indicated by magenta shows the flat area owned by Tokai-village. The surface buildings are shown by the solid lines. The underground facility is shown by the dotted lines. The access to the facility is from south-west (lower left corner).

the down-stream. The approximate size of the liquid argon detector is 8 m long and 7 m in diameter. The size of the water Cherenkov detector is 13.8 m long and 9.3 m in diameter. The size of the muon range detector is 7.6m ×7.6m × 5m.

The vertical access shaft will be 8.5 m in diameter. There will be one elevator for the access to the underground facility. In addition, there will be one stairway for an emergency exit. Large equipments up to either 4m×1m or 3m×1.5m can be lowered through this shaft using a crane whose maximum lifting weight is 2.8 tons. At the roof of the underground cavity, there will be another 2.8 ton crane that will run 25 m along the beam direction.

We will have a small independent vertical shaft with a diameter of about 1 meter for forced ventilation (and possibly other piping if necessary). A dedicated shaft for ventilation was considered as an important asset for safe operation in case of accidental venting of gaseous argon. Otherwise, most connections between the surface facility, such as the liquid argon production system, and the underground detectors are expected to be passing through the main shaft.

The surface facility includes three surface buildings, one for the operation and monitor of the 2 km detector complex, one for liquid argon processes and the other for water purification systems.

The surface building for the operation and monitor has dimensions of 21 m×14 m. The height should be approximately 7 m. The building has a control room where physicists take shifts, operate and monitor the detector complex. In addition, there is a crane whose lifting weight is 2.8 tons. This crane is used to lower heavy equipment to the underground facility.

The water purification system will be mostly located at the surface, with a small portion at the first floor below ground (41.77 m below the surface level) and the bottom of the facility (57.27 m below the surface level).

We plan to generate pure water from the city water. The main component of the primary pure water

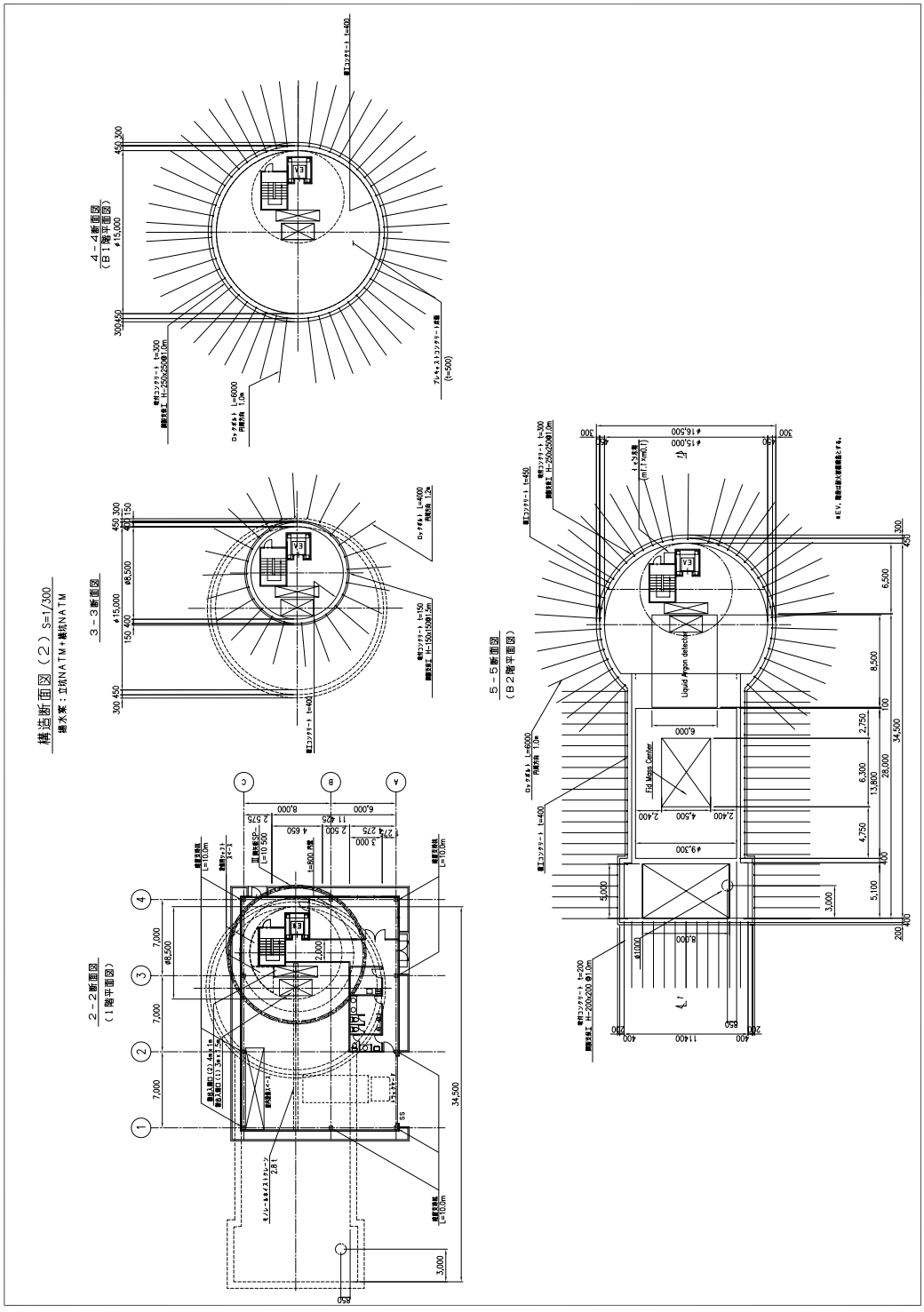


Figure 11: A designed and costed experimental hall(top view). This hall will hold a water Cherenkov detector, fine-grained tracker, and muon ranger.

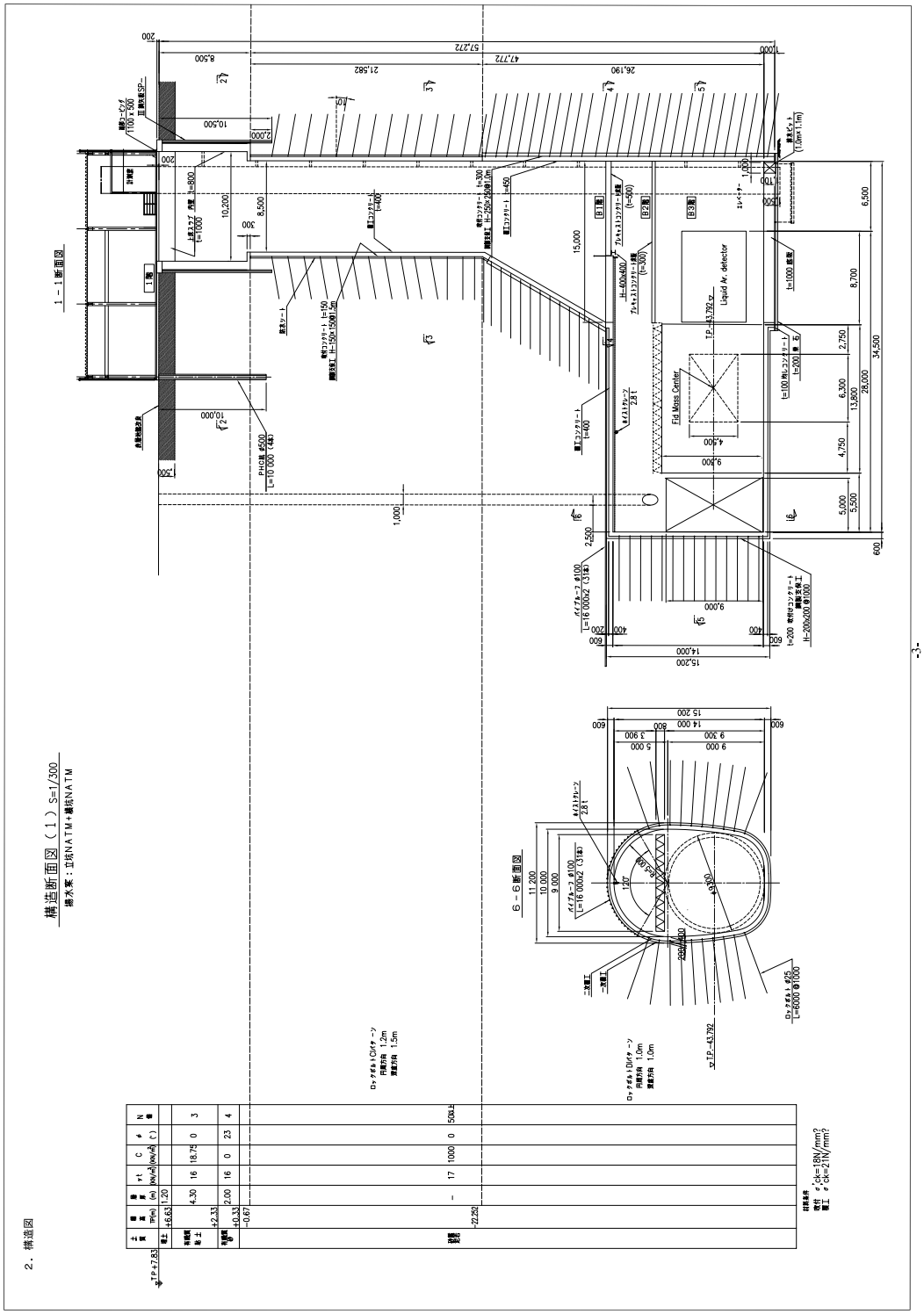


Figure 12: A designed and costed experimental hall(side view).

system will be the reverse osmosis system. Another, less favored, option is to use the primary pure water produced by the pure water system at the J-PARC accelerator facility. In this case, the primary pure water produced at the accelerator facility will be transported to this facility. (Even with this option, we think we need the primary pure water system for pure water make-up and emergency.) The primary pure water will be further purified by the ultra-pure water system, which is located on the surface and underground. The ultra-pure water thus produced will be fed into the detector enclosure. The water will be further purified through the circulation between the detector enclosure and ultra-pure water system. The surface building for the water purification system will be 10 m$\times$10 m and 5 m in height.

The complete system at the surface for the liquid argon process will comprise compressors, dedicated ventilation, external storage tanks, and vaporizers (however, the liquid phase argon purification system will be located underground). As mentioned, it is foreseen to dedicate a building for liquid argon processes (filling, cooling, venting, ...) and remote control. This surface building will be 7 m$\times$7 m plus 5 m$\times$4 m and 5 m in height. In addition, two tanks for argon storage and vaporizers will be located outside of the buildings.

The total electric power for this facility is designed to be 400 kW. The electricity needed for the water Cherenkov detector (including the water purification system), the liquid argon detector, muon range detector and the facility are approximately 120kW (40kW for the water system), 170 kW, 10 kW and 72 kW, respectively.

7 Water Cherenkov Detector

7.1 1 kton Enclosure and Substructure

The 1 kton water Cherenkov detector will be installed in a water enclosure 13.8 m long built into the 2KM hall complex. The enclosure contains a cylindrical volume of water of 9.3 m in diameter and 13.1 m in length. The enclosure will be made water-tight by the installation of a plastic lining on the concrete walls of the detector hall. The up- and downstream ends of the enclosure do not have concrete for support, and therefore the liner alone will not sustain the pressure of the water. Therefore, the up- and downstream walls will be made of 20 mm thick steel plate supported by 350 mm H-beams every 70 cm in both vertical and horizontal directions.

Inside the enclosure, there will be structures to support the photomultiplier tubes. Just as for Super-K, 12 PMTs will be mounted into a module. These modules will be installed into the detector enclosure. The present design of the water enclosure and the PMT support structure are shown in Figure 13

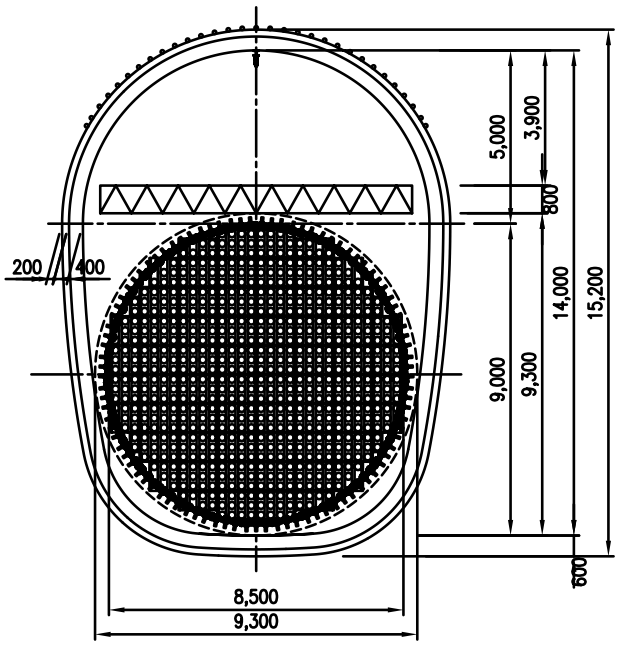


Figure 13: The front view of the water enclosure and the PMTs mounted on the detector walls. 12 PMTs are pre-assembled as a PMT module, and the module is attached to the PMT support structure in the enclosure.

The electronics system will be located at the top of the enclosure, which is 10.1 m above the bottom of the enclosure. The top of the enclosure is also to be used as an underground working space.

The water Cherenkov detector must be calibrated. Therefore, several pipes that allow entry of various calibration devices from the top of the enclosure will be prepared.

7.2 Water Purification System

We have built several water purification systems for water Cherenkov detectors so the equipment and procedures necessary are well known to us. This detector will be filled with about 1 kton of high purity water. Contaminants such as ions, organics, and particles must be excluded in order to achieve a mean free path for light which is closely matched to the mean free path in Super-K (greater than 50 m in the range of 350 - 450 nm). After filling, this high degree of purity must be maintained in spite of the unavoidable release of contaminants by all materials in contact with the water. In addition, bacterial growth must be minimized.

7.2.1 The primary filling system

In principle, reverse osmosis (R.O.), deionization (D.I.) and filtration techniques which are commercially available and actively used, are suitable to achieve the water quality required. Deionization provides very good quality water even when the supply water is very poor, but it requires large quantities of caustic chemicals when fed with untreated water. The R.O. technique will reject total dissolved solids with an efficiency of about 95%, and will reduce the particulate size to $\leq .0.001\mu$m. R.O., however, requires a large amount of electrical power, and in addition rejects some fraction of the processed water as waste. Therefore in order to conserve power and minimize waste, we will operate in a mode whereby we fill the detector using the R.O. system and recirculate using the deionizer. The system design is based on our extensive experience in this area from the operation of the IMB, Super-K and K2K experiments. Pumps will supply about 20 gallons per minute from a local source to the purification system. Depth filters, carbon filters, a water softener and pre-filters will remove silt and particles to the 10 micron level in preparation for the R.O. membranes. The output of the R.O. unit will go to a degasifier to remove dissolved gasses as a precaution against small bubble formation on the phototube surfaces and to remove radon gas. This will be followed by a sodium exchange anion resin to remove uranium and thorium and then by a mixed bed deionizer. This is followed by more filtration, ultra-violet sterilization and final ultra-filtering before the water is put into the detector. This process will fill the detector in about one week of continuous operation.

7.2.2 Recirculation

It is crucial to recirculate the water in the detector through the purification system. This is necessary due to the constant leaching out of substances which reduce the light attenuation length. In addition, the growth of micro-organisms must be inhibited by sterilization during recirculation. The water removed from the detector for re-purification will be of high quality–much higher than the quality of the original supply. As a consequence, the recirculation process will be less demanding. Therefore, we can by-pass the pre-treatment stage and the R.O. system and use only the D.I. portion of the original filling system. The water in the detector will be recirculated in about one week. This procedure will be a cost-effective solution since the chemical costs associated with D.I. of this previously purified water are much lower than the corresponding electrical power costs of the R.O. pumps. Once the detector is filled, therefore, the R.O. system will only be used for additional water that might have to be added to the detector to make up for any losses due to leaks or evaporation.

7.2.3 Temperature control

During recirculation, the water will pass through a chiller unit which will maintain the detector water temperature at 15C. At this temperature bacterial growth will be minimized. The detector enclosure will be insulated in order to require minimal use of the chiller unit.

7.2.4 Logistics

Some of the components from the water system at the K2K experiment can be reused. These pieces of equipment must be broken down and re-installed at the new location. Our budget includes the labor cost

for this procedure.

7.3 Photomultiplier Tubes

As we describe in the section on simulation, we have found that the coarse pixelization of 50 cm PMTs in a detector considerably smaller than Super-K degrades the pattern-recognition required for efficient e/μ identification and ring-finding. This introduces differences in reconstruction efficiencies that become important sources of systematic uncertainty. Our goals for T2K require us to control the systematics extremely well; hence, pixelization becomes an important parameter. Our design incorporates a larger number of smaller diameter PMTs to achieve finer pixelization, while 40% photo-cathode coverage of the detector surface provides the required energy resolution. This arrangement replicates more closely the layout of Super-K and will result in better overall performance (see section 10.1.2). Our baseline design therefore incorporates ∼5660 eight-inch Hamamatsu R5912MOD PMTs. The Super-K design of waterproof potted base, integrated voltage divider and signal/HV cable will be used; this design has been perfected over the lifetime of the Kamiokande and Super-K detectors. No problem is foreseen with timely production of these PMT assemblies. Hamamatsu has, in the past, produced more than 1000 R5912MOD per month. Details of the mounting structure for the PMTs have yet to be determined. However, with the existing Super-K and K2K (1 kton) detectors as guides, the design and installation should be relatively easily developed.

7.4 Electronics for the Water Cherenkov Detector

The 2KM Water Cherenkov detector will require high voltage supplies, signal electronics, and data acquisition equipment for approximately 5660 PMTs. The requirements and implementation are well understood by our group and carry no technological, schedule, or cost risks. The one unique requirement for long baseline experiments is the need to accurately and reliably match event triggers with the times of beam spills. For K2K this was accomplished solely by GPS time-stamping. At 2 km we will augment this with a fast signal derived from the beam in order to reduce the background event rate due to cosmic rays.

7.4.1 Water Cherenkov High Voltage System

The PMT high voltage (HV) supply system described here is based on a remote-controlled rack-mounted "mainframe" manufactured by Universal Voltronics, which acquired the product lines previously supplied by LeCroy. Comparable systems from vendors such as CAEN may also be considered.

One UV-1458 mainframe unit accommodates up to sixteen UV-1461 HV modules. In turn, each UV-1461 module provides 12 channels of HV, up to 2.5 kV, at 2.5 mA per channel. The mainframe provides setting and monitoring of each channel via computer links or manual front panel controls. Each UV-1461 channel has far more current capacity than needed for a single PMT. In order to reduce overall cost, we will multiplex 12 PMTs onto one HV channel with a custom distribution card. The distribution card will be based on an existing design successfully used in the Super-K outer detector. The critical element of the distribution boards is the ability to disable individual misbehaving PMTs that would otherwise cause the HV channel for a group-of-12 to trip.

PMT fabrication does not control the voltage required to achieve a nominal gain to better than a few hundred volts, yet we wish to apply a single voltage to a group of twelve. For the SK outer detector, we solved this problem by sorting PMTs during pre-construction calibration so as to identify groups of 12 compatible PMTs. We make individual final adjustments at the level of a few 10s of volts using zener diodes.

To handle 5660 channels, we will need 4 UV-1458 mainframes, 42 UV-1461 HV modules and 491 distribution cards. The paddle cards will be housed in 23 crates, each with a low-voltage power supply for the HV cutoff relays. These totals include 10% on-hand spares for swap-in replacements. The total cost for the HV system will be $424K (about $75/channel), as detailed in Section B.2.4 in Appendix B.

7.4.2 Water Cherenkov Signal Electronics and DAQ

The requirements for PMT signal electronics are: provide an event trigger, convert charge and hit time to digital data, and record multiple hits over microsecond timescales to record muon-decay electrons. New electronics are under development to replace the ATM boards [20] presently in use for the Super-K inner detector. We expect the new boards to have better reliability due to the decreased number of discrete components, lower power usage due to highly integrated CMOS ASICs, and most importantly much lower cost per channel. We estimate no more than $200 per channel for front-end electronics. Although the exact details of the implementation remain to be determined, including the basic DAQ architecture, we envision duplicating the electronics used at Super-K for use in the 2KM detector, and sharing economies of scale.

The trigger for a neutrino event is constructed by the coincidence of greater than a certain number of PMT hits in a narrow time window (hitsum). This will be used to determine the reference time for the PMT hit times. The trigger time is determined to several nanoseconds, and with suitable synchronization should allow resolution of the bunch structure (8 bunches in 5 μs).

The rate of cosmic rays in the WC detector is estimated to be of order 1 KHz. To reduce the amount of data saved for analysis, we wish to consider only triggers in a window of 10-50 μs around the beam spill. This could be done promptly offline using GPS information; this is similar to the technique used at Super-K although the GPS matching happens much later. A better approach is to provide a fast signal derived from beam timing. This signal can be derived up to 10 ms in advance of the spill and communicated by optical fiber or microwave link.

The recorded data will be processed by PC-based workstations. With maximum trigger rate of order KHz, and a final event rate of order Hz, there is no particular challenge in accomplishing this.

7.4.3 Event Time Synchronization

The K2K experiment demonstrated the successful application of a time synchronization system [21] which used GPS data to provide synchronized UTC time at the near and far detectors. Trigger timestamps provided 20 ns precision and 50 ns absolute accuracy, with great reliability. Regardless of the availability of a beam-derived signal by optical fiber, we wish implement GPS time stamping as a backup and redundant check.

We propose to reproduce the K2K system for T2K, taking advantage of eight years of operational experience to introduce minor improvements. The new system will have 10 ns precision, and about 50 ns absolute accuracy. The system maintains time accuracy within these limits as long as it has at least one GPS satellite in range, and its rubidium-stabilized oscillator allows it to maintain time accuracy within 100 ns for periods up to about 5000 seconds if there is a temporary loss of all satellite data (which never actually happened throughout K2K running).

The system will consist of identical installations at each site (J-PARC, 2km detector, and Super-K). Each site will be equipped with the following:

- Two independent commercial GPS receivers:
  1. TrueTime rack-mounted XL-DC GPS receiver;
  2. Motorola M12-plus OEM GPS receiver card (mounted on LTC).
- Weatherproof, lightning-protected antennas for each GPS receiver.
- Local Time Clock (LTC) board (custom VME board with rubidium-stabilized oscillator).
- VME crate with power supply.
- VME FIFO module to buffer GPS data.
- VME-PCIbus interface, to link PC to VME crate.
- PC workstation (typical 2 GHz, 512 MB RAM, 80 GB disk, ethernet ports, etc) with Linux OS.

In addition, we will supply on-hand spares for each item above, ready for swap-in replacement if needed. Costs for GPS installations at the Super-K and J-PARC sites are requested elsewhere.

For the 2KM detector site, we also propose to install a dedicated optical fiber link to the 280 m detector control room, providing a direct, calibrated-delay beam arrival trigger timing signal. The budget presented here includes the cost of the fiber cable and associated custom interface electronics, but not deployment of the cable, which must be managed by the host institute.

The total cost for the time synchronization equipment for the 2km site, including fiber-optic data link, will be $45K, including spares. These costs are summarized in Section B.2.5, Appendix B.

7.5 Calibration Systems

The timing and the gain of each PMT as well as the optical properties of the detector water and the other detector materials must be calibrated precisely. The technique to calibrate the PMTs has been developed in Super-K. Therefore, we plan to use the calibration systems similar to the ones used in Super-K. They include a laser + diffuser-ball system for the PMT timing calibration, a laser + scintillator-ball system for the PMT relative gain calibration, and a laser injection system for the water transparency calibration. In addition, cosmic ray muons and electrons from the muon decay can be used for absolute energy calibration.

In addition to these standard calibration techniques, our physics requirements demand additional calibration systems. The event rate for single-ring muon events must be measured precisely for the precise measurement of $\sin^2 2\theta_{23}$. The rate of single-ring electron-like events must also be measured precisely. From the experience in K2K and from the Monte Carlo studies, we know that the most important calibrations to achieve these goals are those of the fiducial volume and the ring-counting program.

We plan to install walls of small (2" diameter) PMTs in the up- and down-stream edges of the fiducial volume. The down-stream wall of PMTs, which are facing up stream, detect Cherenkov photons from neutrino interactions that occurred in the fiducial volume of the detector. Similarly the up-stream wall of PMTs, which are also facing up stream, detect Cherenkov photons from neutrino interactions that occurred outside (up-stream) of the fiducial volume of the detector. In This way the fiducial volume will be calibrated to an accuracy of better than a few percent. We are testing this and related ideas using the K2K 1 kton tank in 2005.

A significant background to the electron appearance signal in the Super-K detector are π^0s from neutral current interactions. A π^0 decays primarily into 2 gammas which create electromagnetic showers, each of which look similar to that from an electron. However, after event selections for the ν_e signal are applied, the dominant source of background results from asymmetric decays of the π^0, particularly when the secondary gamma has energy less than 100 MeV.

A secondary-ring fitting package has been developed to remove π^0 events from the Super-K data set; however its efficiency at removing the events of the two types described has only been studied using Monte Carlo simulations. Currently, no control sample data for ring counting studies exists. Therefore, it is important to demonstrate e/π^0 separation and compare the results between the K2K 1kt water Cherenkov detector (1kt) and Super-K using the same control sample data with known energy and direction of electron-like single ring and π^0-like two ring events.

Two types of multiple cone generators are being developed, one at UCI and one at ICRR. The ICRR cone generator will emit laser light in a ring shape. One of the UCI cone generators will utilize an LED focused through a toroidal lens, creating a fuzzy ring of light. A number of these LED/lens modules will be placed inside an icosahedron (polyhedron with 20 faces). Another UCI cone generator, based on the design of a multiple cone generator used at IMB, has already undergone preliminary testing.

Vessels made of Derlin were created to mask an isotropic laser-ball and allow light to be emitted from a cone centered about the Cherenkov angle of 42 degrees. A structure is being designed to hold two of these vessels which will allow the vessels to be moved at various angles to one another. The intensity of the light may be adjusted for each laser-ball placed inside of a vessel.

Preliminary tests have already been carried out in the 1 kton K2K water Cherenkov detector. The vessels were shown not to have light leakage other than from the cone-shaped channel and to give a stable

amount of light output over time. It was also determined that the average opening angle from the direction in which the generator is pointing to the hit PMTs does not depend on the light intensity. One goal of the testing is to optimize the design of the vessels so that they mimic electron and gamma signals as much as possible. We have decided to create a number of vessels with different channel widths to correspond to different electron and gamma energies.

A Monte Carlo for this calibration source is in development.

8 The Liquid Argon Detector and its Infrastructure

8.1 Introduction

The LAr TPC detector for the T2K 2 km site is hosted in a 8.5 m long and 7.2 m diameter stainless steel dewar positioned on mechanical shock absorbers, as schematically shown in Fig. 14. Inside the outer dewar an inner vessel of 5 m in length and 6.6 m in diameter contains the liquid argon. The volume between the two vessels is evacuated and filled with super-insulation layers to ensure adequate thermal insulation. The inner vessel contains about 315 tons of liquid. A smaller volume of about 150 tons is confined by the inner Time Projection Chamber (TPC), corresponding to a neutrino interaction fiducial volume of about 100 tons. The chamber consists of a stainless steel mechanical frame with parallelepiped shape inscribed in the inner vessel cylinder.

The cathode of the TPC is placed in the middle of the inner volume, along the longitudinal axis. There are two options for this element: filled with frozen water or with solid CO_2. The choice will depend on what decision we make about the structure of the inner target. The first option for the inner target structure is a cylindrical target structure (Fig. 15) made of a 2 mm thick stainless steel cylinder of 60 cm diameter and 5 m length. In this case, the cathode is a pierced stainless steel plane placed longitudinally along the dewar main axis holding the inner target. The second option calls for a parallelepiped shaped inner target (Fig. 15) 25 cm thick and 5 m long. In this latter case, two separate cathode planes would be placed onto the external sides of the target. In both cases, the cathode electrode defines two half-volumes. Each of the two extreme sides of the half-volumes are equipped with two or three wire planes with different wire orientations, constituting the read-out anodes.

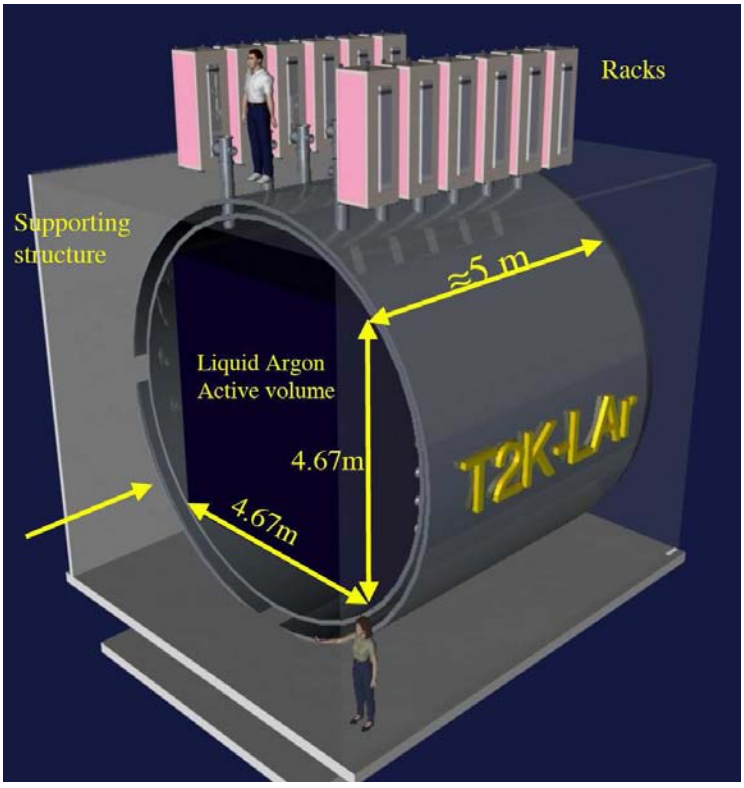


Figure 14: Artistic view of the proposed 100 ton liquid argon TPC detector (upstream endcap removed).

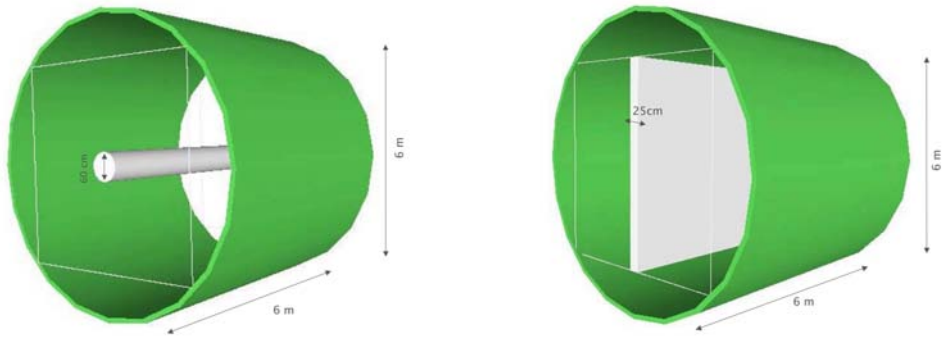


Figure 15: The inner dewar volume with (left) the option of a cylindrical inner target; (right) the option of a parallelepiped shaped inner target.

The electric field perpendicular to the wires is established in the LAr volume by means of a high voltage (HV) system. It serves to permit and guide the drift of the ionization electrons. The system is composed of the above-mentioned cathode plane parallel to the wire planes, placed in the center of the cryostat volume at a distance of about 2 m from the wires of each side, defining the maximum drift path. The HV system includes field shaping electrodes made of stainless steel tubes. These are required to guarantee the uniformity of the field along the drift direction. At the nominal cathodic voltage of about 200 kV, corresponding to an electric field of 1 kV/cm, the maximum drift time in LAr is about 1 ms. At this stage, two options are considered for polarization of the cathode and the corresponding electrodes: (a) in the first option, a HV feed-through sets the required potential on the cathode. The electrodes are placed at degrading voltage from the cathode potential to ground via a series of resistors inserted between the tubes; (b) in the second option, the use of a HV feed-through can be avoided if an oscillating low-voltage is multiplied inside the detector via a Greinacher circuit.

Large area photomultipliers are placed inside the liquid, attached to the supporting mechanical structure, outside the inner fiducial volume, behind the wire planes. The PMTs are manufactured to be sensitive to the VUV prompt scintillation of argon. These signals can be used for triggering. We are also studying the possibility that some of the PMTs could be optimized for the detection of Cherenkov light produced in LAr, a process that has been studied by the ICARUS collaboration [22].

On top of the cryostat there are flanges equipped with cryogenic feedthroughs for the electrical connection of the wires with the read-out electronics. These feedthroughs also provide passage for the internal instrumentation including PMTs, purity monitors, level meters, temperature probes, *etc.* The electronics allow for continuous read-out, digitization and wave-form recording of the signals from each wire of the TPC. The front-end electronics are hosted in crates directly placed on top of the dewar.

The detector is complemented by ancillary cryogenics systems. A gas and liquid recirculation and purification system, a heat exchanger and a LAr buffer are placed in the underground cavern, close to the detector dewar. These systems are connected through cryogenic pipes to the surface, where argon storage, compressor, ventilation and evaporation systems complete the detector infrastructure.

The basic mode of operation is outlined in the following: the passage of charged particles inside the LAr volume produces both ionization and scintillation light signals. Detection of this light by the PMTs provides a method for the absolute time measurement of the event and an internal trigger signal. Reconstruction of ionizing tracks is performed by using charge and the light signals. Ionization electrons induce detectable signals on the TPC wires during their drift towards and across the wire planes. UV photons from scintillation provide a prompt signal on the PMTs that allows the measurement of the absolute drift

time and, hence, of the distance traveled by the drifting electrons. In this way, each of the planes of the TPC provides a two-dimensional projection of the event image; one coordinate gives the wire position and the other is given by the drift distance. A 3D reconstruction of the event is obtained by combining the information from wire planes occurring at the same drift distance.

Events which occur in the inner water (CO_2) target are reconstructed by the detection of particle tracks escaping from the target into the external (instrumented) liquid argon TPC volume.

8.2 The liquid argon cryostat

8.2.1 The cryostat

The basic concept for the liquid argon cryostat has been developed and engineered (see Figure 16 and Table 1). We followed the internationally recognized codes for the design of conventional cryogenic-fluid pressure storage-vessels as covered in the ASME (American Standards of Mechanical Engineers) Boiler & Pressure Vessel Code, Sect. VIII (www.asme.org). Design and construction according to these standards should ensure reliable and safe operation.

The cryostat consists of two concentrically mounted stainless steel cylinders with D-shaped end caps. The inner cylinder contains the purified liquid argon with the drift chamber and is wrapped with layers of superinsulation. The outer cylinder acts as a thin "skin" for vacuum insulation. The heat input through these surfaces is estimated to about 100 W under high vacuum conditions (typ. 10^{-4} mbar). In case of loss of vacuum, the heat input increases to 4 kW.

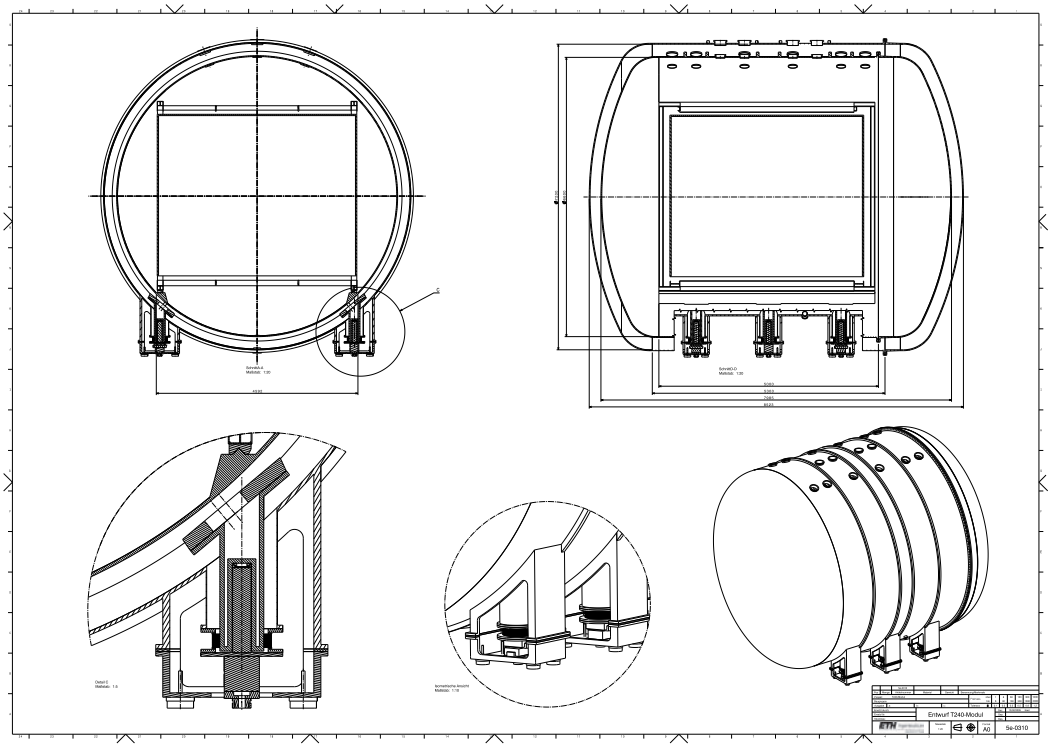


Figure 16: Drawing of the cryostat.

The total weight of the inner cylinder filled with liquid argon and the drift chamber is supported from the ground (at room temperature) so that the outer cylinder is only a shell without any mechanical support function. There are a total of 6 stands foreseen. The supports must be vacuum insulated between the

Table 1: Geometrical parameters of the cryostat.

Number of independent cylinders	2
Outer vessel	
outer diameter	7.2 m
length of cylinder	5.3 m
total length (incl. end caps)	8.5 m
wall thickness	20 mm
weight of cylinder (incl. supports)	24 t
weight of screwed end cap	9.8 t
weight of welded end cap	7.6 t
Inner vessel	
outer diameter	6.6 m
length of cylinder	5 m
total length (incl. end caps)	8 m
wall thickness	20 mm
weight of cylinder (incl. supports)	25 t
weight of screwed end cap	8.5 t
weight of welded end cap	6.6 t
material of vessels	stainless steel
thermal Insulation	super–insulation in vacuum
total (cold) internal volume	237 m^3
total LAr mass	315 t

inner and the outer cylinder and must provide adequate thermal insulation between the inner cylinder at LAr temperature (about 89 K) and the ground at room temperature. This is achieved by using ceramics to support the weight and long connections between the warm and cold parts. The thermal losses through a supporting foot have been numerically calculated and found to be below 50 W. Hence, with 6 supporting feet, the total heat input from the floor is less than 300 W.

Detailed finite element calculations have been performed in order to optimize the wall thickness, the positions and strength of the reinforcing rings and the supports, and to make sure that the ASME Pressure Vessels specifications for these tanks are actually fulfilled.

Figure 17 shows a cut view of a support. One of the supports in the center is fixed; the others can slide in the longitudinal and/or transverse direction to accommodate the thermal contraction of the inner vessel during the cooling down phase.

There are feedthrough flanges on both the inner and on the outer cylinder, *i.e.*, the cables and filling tubes are lead through the insulation vacuum from the cold inner cylinder to the room temperature outer cylinder. The heat input between the inner and outer flanges is driven by the signal cable connections. The estimated heat input through these cables is 100 W.

Pumping ports are foreseen to pump the inner cylinder before it is filled with LAr and for the outer cylinder to maintain a good insulation vacuum. An additional flange is mounted at the bottom of the dewar and can be used to drain the dewar from LAr.

The total heat input is estimated to be 500 W, or about 200 lt LAr per day, corresponding to a boil-off of 0.1% of the total contained liquid volume per day. Hence, there is no need forseen for active cooling of the dewar itself, *e.g.* with liquid N_2. The cooling is provided either by compensation of the boil-off or, preferably for long-term operation, via a standard Linde-Hampson refrigeration system (see Section 8.3.1).

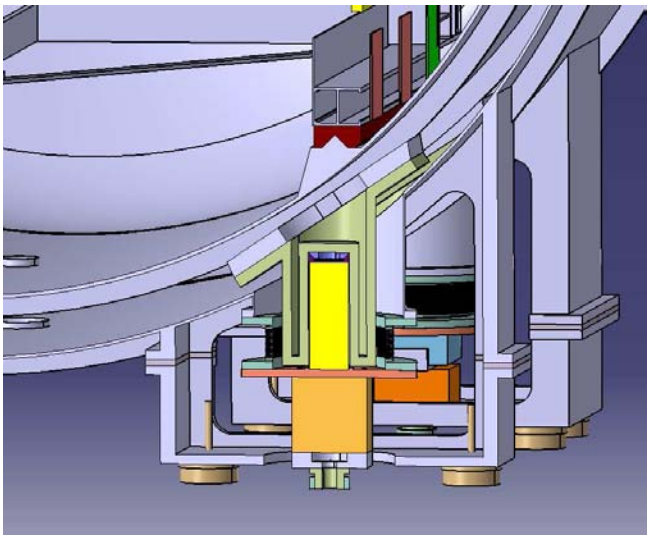


Figure 17: Cut through a support of the LAr cryostat.

8.2.2 The inner target

We expected that the knowledge of the neutrino cross-sections and nuclear effects will improve in the coming years thanks to new measurements performed for example in experiments such as K2K, MINERνA, *etc.* However, the extrapolation between argon and water targets can plagued by uncertainties, which will affect the goal of precision measurement at T2K. The "straightforward" solution is to insert an additional target within the 100 ton liquid argon detector.

This approach ("inner target" or "embedded target") is supported by kinematics of the events. At low neutrino energy, secondary particles are produced at low momentum and large angles. Hence one is forced to consider a target fully immersed into the liquid argon imaging volume; it is difficult to envision a non-immersed or upstream target whose products could be measured in the liquid argon with high efficiency.

The main motivation of the inner target is therefore to collect a sample of neutrino interactions with water or oxygen nuclei, analogous to those occurring in the Super-Kamiokande detector, but with the particle tracks entering the liquid argon imaging volume. One could then reconstruct in detail these events by exploiting the low threshold of the TPC detector and its ability in reconstructing multi-prong events.

Different media may be considered for the additional target. The most promising media are water (H_2O) or dry ice (CO_2). Other elements like pure oxygen, nitrogen, or hydrocarbons are not favored.

The additional target medium must not make contact with the pure argon, otherwise contamination could occur. We assume that the additional medium is contained in a separated volume. At this stage we consider two possibilities: (1) a specially located steel tube in the middle of the detector volume, and (2) a double-cathode structure whose inner volume is filled with the additional medium. The volume will be evacuated and filled during or after the liquid argon filling phase.

The geometrical parameters of the inner target were optimized for the case of water (ice). In the case of the parallel plane geometry, the chosen geometry provides a target mass of 5.37 tons, while the cylindrical tube would amount to 1.30 tons. The parallel plane geometry is preferred for its larger target mass, and also from the point of view of physics requirements (see Section 10.2.8). However, the cylindrical tube offers *apriori* simpler mechanical constraints. The final decision concerning the geometry will be made after detailed mechanical simulations and laboratory tests of freezing have been performed.

8.3 Liquid argon process

8.3.1 Initial cooling and refrigeration

The liquid argon filling, cooling and liquid recirculation system is schematically presented in Figure 18.

During the initial cooling, the mass of the inner detector and of the dewar must be cooled down to LAr temperature. Since no active refrigeration is foreseen, there are in total about 40 tons of steel to be cooled by liquid argon boil-off. The amount of argon needed for cooling is about 20 LAr m^3, less than 10% of the total stored argon (315 t). Hence, this simple solution is affordable and preferred.

In normal operating conditions the total heat input induces a boil-off of about 200 l of liquid argon per day (or approx. 10^{-3} of the total volume of argon), which is quite small. During forced liquid argon recirculation (see Section 8.3.2) the consumption is estimated to increase by an additional 400 l/day.

Since the cryostat is not actively cooled, *e.g.* with liquid N_2, the cold input is externally provided either by compensation of the boil-off or preferably via a standard Linde-Hampson refrigeration process.

In the latter case, the argon itself is used as medium of the heat machine. In an ideal situation, the thermodynamic cycle is the following: the argon gas is compressed reversibly and isothermally from ambient conditions to some high pressure. This high pressure is selected so that the gas will become saturated liquid upon reversible isoentropic expansion through an expander. The final condition is taken at the same pressure as the initial pressure.

In practice, high pressure argon is liquefied via a Joule-Thompson expansion valve (See Fig. 18), which for zero heat transfer (insulated valve) and zero work implies conservation of enthalpy. An ideal gas would not experience a temperature change upon expansion through an expansion valve. To our gratification, argon is imperfect at low enough temperatures and high enough pressures.

Refrigeration of the liquid argon volume is performed by means of a closed circuit with a compressor placed at the surface, operated by a feed-back on the temperature and pressure of the inner vessel. Heat losses under normal operating conditions correspond to 500 W (cold) or $\approx$ 10 kW of electric power. If we include the power required for the liquid argon recirculation/purification described in the next Section we arrive at a total of $\approx$ 30 kW of electric power to be supplied.

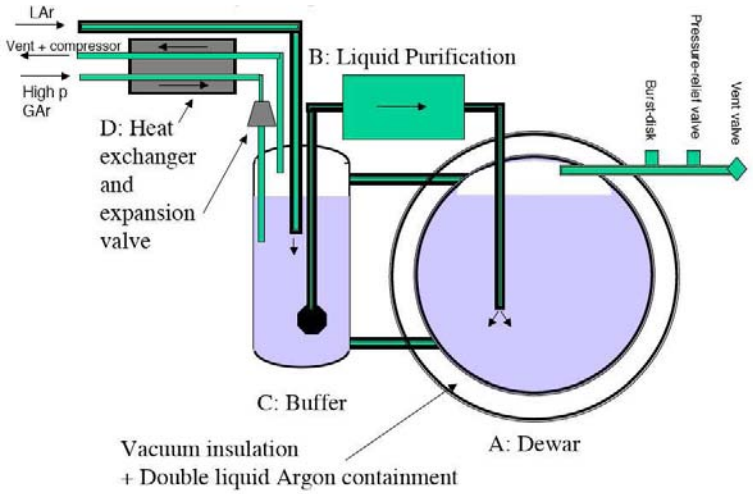


Figure 18: Scheme of the LAr cooling and recirculation system.

8.3.2 Vacuum and liquid argon purification

The liquid argon purity is a critical item for the good performance of the detector. The major electronegative impurities in liquid argon which are of importance for the TPC are electron attaching oxygen and/or fluorinated or chlorinated compounds. To achieve long electron drift paths the liquid must be free of these impurities, which will otherwise decrease the electron collection efficiency.

The maximum electron drift length for the proposed TPC detector is about 2 m. This implies that, for correct operation of the detector and in order to reach a sufficiently high value for the drifting electron lifetime (a few ms), liquid argon has to be pure with a concentration of electronegative impurities lower than 0.1 part per 10^9 (ppb) O_2 equivalent during all phases of operation. Standard commercial LAr has a much higher contamination (typically a few parts per million oxygen equivalent); moreover, LAr can be contaminated inside the cryostat from outgassing of the walls and TPC components (electrodes, cables, *etc.*).

The required purity is therefore first ensured by using suitable materials, cleaning, and careful design of the internal components. Additionally, internal surfaces must be vacuum conditioned, since during steady operation pollution of the LAr is mainly due to out-gassing of the inner surfaces and inner detector materials in contact with the gaseous argon (impurities freeze in cold).

The second requirement is that filling of the detector dewar from the external storage must be performed through sets of Oxysorb-Hydrosorb filters[4] placed in series. Each set of filters is dimensioned to allow for the purification of the LAr volume starting from standard commercial LAr (with a concentration of H_2O and O_2 of about 0.5 ppm).

The third requirement is that a recirculation system has to be implemented in order to reach the ultimate purity of the liquid at equilibrium during the detector operation compensating for sources of impurities (typically degassing of materials of the components immersed in the liquid). During the refrigeration cycle described in the previous section, the gaseous argon is passed through a purification filter before it is filled back as LAr to the main tank. Additional argon purification is also provided by a recirculation system through purification cartridges in liquid phase. We therefore foresee a liquid argon recirculation system. As expected, the liquid purification scheme is an important item. A similar system turned out for example to be very important in the ICARUS T600 operation[23].

The liquid recirculation system can be dimensioned under the requirement of a 48 hours recirculation period. This implies a recirculation rate about 3500 LAr l/hour, which corresponds to 1 l/s. This can be handled by employing 7-8 Oxysorb cartridges arranged in two parallel circuits. The scheme of the liquid argon recirculation system is shown in Fig. 18.

The operation of the system schematically consists of three logic steps. At first, vacuum is made inside the dewar at the level of (or lower than) 10^{-4} mbar. This procedure lasts from one to several weeks and allows evacuation of water, air and any other residual from the inner detector volume. In addition, one could test vacuum tightness of the detector, needed for stable and efficient operation, since it ensures that the rate of contamination of the liquid, and hence the ultimate achievable purity, will be determined by degassing of internal materials and not by leakage. The initial cooling and filling with liquid argon follows and also lasts for about one week. This is needed to cool down the inner vessel and the inner instrumentation, for a total steel mass of about 20 tons. This procedure should proceed quite rapidly in order to limit the amount of degassed impurities from dewar walls and inner detector components. During this phase efficient gas recirculation is beneficial. Once the detector is cold, the level of liquid argon can be increased and the actual filling could start. At this point, the liquid continuous recirculation begins. It will take nearly one month to reach the required high-purity level which slowly improves with time. The slope of the improvement increases as the out-gassing decreases with time. The asymptotic level of purity is finally reached when the speed of recirculation balances the potential rate of input of impurities, which should be zero in the ideal case. We observe that the liquid argon phase recirculation should be minimized in order to reduce the heat input due to viscosity, to the pump operation, *etc.*

[4]Hydrosorb and Oxysorb are registered trademarks of Messers-Greisheim.

8.4 Liquid argon monitoring

8.4.1 Liquid argon purity monitors

The method to determine the lifetime of electrons consists of measuring the attenuation of the charge of an electron cloud drifting under the action of an electric field as a function of the drift time. Different types of liquid argon purity monitors have been developed for existing LAr detectors and for future experiments. Traditionally, the problems encountered in designing these monitors have been related to the creation of a sufficiently large drift electron cloud (in order to produce clean signals) above noise and to the determination of the purity level with sufficiently high precision and sensitivity.

Purity monitors with a sensitivity to a level below 0.3 ppb as needed here, were built for the ICARUS detector [23]. More recently, a novel liquid argon purity monitor was developed [24] with a sensitivity to electronegative impurities of the order of ppb (O_2 equivalent) as needed for the operation of a LAr TPC. Also here, the principle is to measure the lifetime of quasi-free electrons in LAr, since this is the important parameter for the operation of a drift chamber. Free electrons are produced by ionizing the LAr with α-particles emitted by the ^{210}Po chain daughter of an isotope ^{210}Pb source. From the measurement of the charge of the electron cloud at the beginning and at the end of a drift path, together with the drift time itself, the lifetime of the electrons can be derived. In a series of measurements performed with a dedicated setup, drift electron lifetimes of the order of 100 μs were measured with a precision of 2-5%.

8.4.2 UV laser calibration

The principle of laser calibration relies on the possibility of producing tracks inside the LAr volume that are similar to those created by ionizing particles and of which one knows (*apriori*) the ionization yield, the position and the time. These 'tracks' are not affected by multiple Coulomb scattering and Landau fluctuations.

A multi-photon process is one which occurs through the simultaneous absorption of two or more photons via virtual states in a medium. These processes require high peak powers which are easily available from pulsed lasers. Bound electrons may absorb several laser photons simultaneously to excite the atom to high energy levels or even to overcome their ionization potential. The absorption of multiple photons makes this process highly non-linear (fourth-order for Ar); its cross-section strongly reduces with the order of the process, thus making its effectiveness largely dependent on the laser operating frequency. In order to produce a significant ionization in a target medium (typically gaseous), for high-order processes it is necessary to have very high intensities. This is typically achieved by focusing the laser beam. Interaction of laser with matter in the liquid phase has been comparatively less studied with respect to gas and solid phase. In particular, no measured energy level diagrams are available for elements in liquid phase, whereas *abinitio* calculations are made difficult by the lack of an order. Nevertheless, some important features are well understood and reported in [25].

A proposal to employ UV laser calibration has been made for the ICARUS detector and a R&D program is underway. If successful, we plan to use this calibration method for the LAr TPC detector in T2K by sending the laser beam through some of the dewar top flanges, suitably equipped with quartz windows, which are transparent to the laser UV light.

8.5 Inner detector

8.5.1 Mechanical structure and TPC wire planes

The inner detector is composed of a rigid mechanical frame made of stainless-steel beams that is based on the cryostat floor by means of a system of rails and adjustable feet. The structure is made independent from possible deformations of the cryostat occurring during the initial cooling and it is also self-supporting. The stainless-steel frame has dimensions of about 5 m in length, 4.5 m in width and 4.5 m in height.

Two lateral wire-frames with the task of supporting the two (left and right) TPCs are positioned on the vertical longitudinal sides of the mechanical structure. The structure is designed in order to sustain the

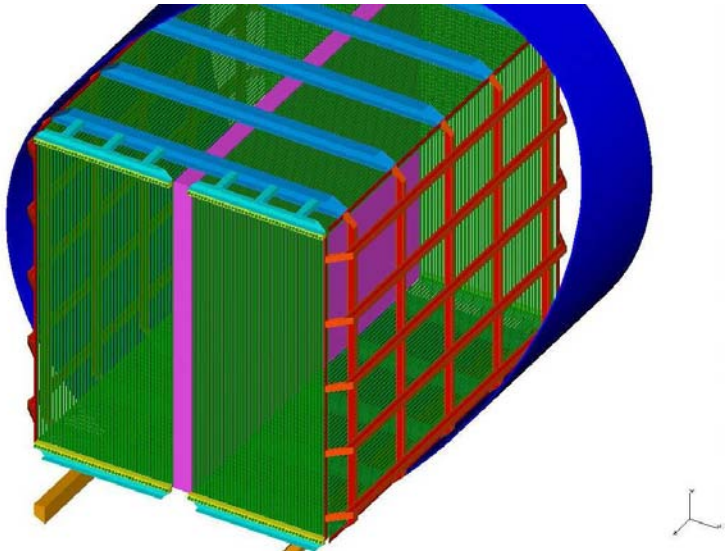


Figure 19: Layout of the inner detector supporting structure. One can notice the central inner target, the race-tracks, the sustaining rails and one of the two chamber supporting frames.

total force applied by the TPC wires without appreciable deformations. In the option of two wire planes per each detector half, this force amounts to about 9 ton.

Materials of the mechanical structure are chosen and treated to guarantee the LAr purity and low level of radioactive elements. The beams and the pillars of the structure are built with AISI 304L stainless-steel. Non-metallic components are made of Peek, Vespel or similar plastic material with excellent thermomechanical properties at low temperature.

Figure 19 shows a view of the supporting mechanical structure. The race-tracks field-shaping electrodes, electrically separated from the conducting beams by Peek or Vespel pieces, surround the mechanical supporting structure.

The structure is also designed to hold the signal and HV connectors, the PMTs, and the monitoring devices. Once assembled, the structure equipped with TPC planes and the other devices will be moved into the dewar by means of the bottom rails and subsequently aligned and placed in its nominal position.

The main features of the TPC wire planes are listed in Table 2. In the baseline detector design there are two TPCs (Left and Right chamber) placed inside the cryostat along the beam direction. Each TPC consists of a system of two parallel wire planes separated by 3 mm. Wire directions in the planes run at $\pm$ 45° with respect to the horizontal direction. The planes closer (farther) to the cathode are called Induction-1 (Induction-2) planes. The wire pitch normal to the wire direction is 3 mm. We are also considering a third wire plane in each chamber, in order to increase redundancy in the event reconstruction and to help in solving possible ambiguities. The increase in mechanical complexity and in the number of electronics chambers is considered to be affordable.

Wires are made of AISI 304V stainless steel with a diameter of 150 μm. They are stretched in the frame supported by the mechanical structure previously described. Each of the two-wire-plane chambers contain about 4500 wires, some of which of decreased in length (see Table 2). The tension applied to each wire corresponds to 10 N in the baseline option. This value will be further optimized by test measurements and by a global optimization of the thermomechanical response of the detector and of the sustaining mechanical structure.

Wires are individually mounted on the supporting frame, after having been pre-tensioned with the required force, anchored by slipknots and pins onto the wire frame. A printed circuit establishes the

Table 2: Main parameters of the internal detector mechanics. In the baseline option, two planes will be instrumented for each TPC chamber. Optionally a third vertical plane could be considered.

number of read-out chambers	2
number of wires planes per chamber	2 (all read-out)
number of optional wires planes per chamber	1 vertical
wires orientation respect to horizontal	$\pm 45^0$
wires orientation respect to horizontal	90^0 (optional)
wires pitch (normal to the wires direction)	3 mm
wires length:	
wires @ $\pm\, 45^0$	6.4 m
wires at the borders ($\pm 60^0$)	0 m to 6.4 m
optional vertical wires (90^0)	4.5 m
wires diameter	150 μm
wires nominal tension	10 N
number of wires / plane:	
wires @ $\pm\, 45^0$	118
wires at the borders ($\pm 45^0$)	2120
optional vertical wires (90^0)	1666
number of wires / chamber:	
@ $\pm\, 45^0$	236
at the borders ($\pm 45^0$)	4240
optional vertical wires (90^0)	1666
total	4476 (6142)
total number of wires	8952 (12284)
maximum drift length	2.21 m
maximum drift time @1000 V / cm	$\approx$ 1.1 ms
distance between race-tracks axes	40 mm
Imaging volume :	$\approx$ 100 m^3
length	5 m
width	4.5 m
height	4.5 m
total imaging LAr mass	**140 ton**

electric connection between wires and connector pins, in turn connected to signal cables linked to the cryostat feedthroughs.

8.6 Light read-out system

8.6.1 Scintillation light

The prompt scintillation light yield is quite high, of the order of 10^4 photons/MeV. If we assume a detection energy threshold of $\sim$ 10 MeV, this corresponds to a minimum of 200000 detected photons. Since the cathode plane and the inner target system located in the middle of the detector can conservatively be assumed to be non-transparent, the minimum number of photons to be detected reduces to 100000. The reflecting properties of the cathode could be improved by the deposition of any reflective material such as teflon which would not perturb the electric field.

In order to detect this light efficiently, one can employ a system of PMTs directly immersed in the liquid, as already implemented for the ICARUS experiment [23]. Glass window PMTs are however not sensitive to the 128 nm scintillation light. There are two solutions to this problem: (1) select PMTs with large photocathodes sensitive to the DUV region, or (2) standard large PMTs can be made sensitive to scintillation light by coating the windows with a proper fluorescent wavelength shifter (WLS), *i.e.*, a compound which absorbs and reemits UV radiation with an emission probability peaked in the convenient region (*e.g.* blue), where the transmittance of the glass window and the photo-cathode quantum efficiency are sufficiently high.

The practical and economical solution of ICARUS consists in adopting large surface 9357FLA Electron Tubes PMTs: 12-stage dynode PMT with hemispherical 200 mm diameter glass window, manufactured to work at cryogenics temperature. It was shown that TetraPhenyl-Butadiene (TPB) can be used as wavelength shifter on these PMTs, resulting in a total quantum efficiency of the system (PMT + TPB) to be about 8%. However, the long term stability of this solution and a measurement of this QE during actual detector operation needs to be further demonstrated. When defining the number of necessary phototubes, we conservatively assume an QE $\simeq$ 1%. Other solutions with different WLS and various coating methods are currently being investigated.

Other devices able to detect directly the light at 128 nm are manufactured by the same company (ElectronTubes). The new PMTs (model 9425B) are foreseen to run in the cold and according to the data sheet, have a QE of $\sim$ 7% at $\sim$ 128 nm. These tubes are however almost five times more expensive than the previously considered 9357FLA PMTs.

The number of 9357FLA 8" TPB coated PMT would be $\sim$ 60. Given their smaller area but larger QE, the number 9425B PMTs would be $\simeq$ 150. This second solution is considered to be more reliable, however, currently its practicability is limited by the cost of the tubes. The final choice will be made later when results from tests with WLS and coating methods are finished. With the market of PMTs still evolving, we can expect that the price of 128 nm sensitive photo-devices will decrease with time.

The high voltage system for polarizing the PMTs has been designed to reduce the number of HV feedthroughs and to minimize power dissipation in the liquid.

The PMT read-out system is structured as a multi-channel recorder that stores the anode current information during the drift of the free electrons. Each channel is equipped with an amplifier that integrates over 10 μs followed by a 10-bit ADC, sampling the signal every 50 ns. For this purpose a custom analog board will be designed and employed.

8.7 High voltage system

In the LAr TPC, each wire collects signals from a large detector volume, defined by its length, by the total drift length and by the wire spacing. The task of the HV system is to produce a stable and uniform electric field over the $\approx$ 2 m maximum drift length. At the nominal drift field of 1 kV/cm, one requires a voltage supply delivering of the order of 200 kV.

The electric field in the drift volumes is kept uniform by means of field shaping electrodes, called the race-tracks. In order to investigate the field uniformity, numerical calculations were performed assuming different distances between field shapers. The computed field amplitude along the drift path shows that a field variation of ‰ is noticeable at 4 cm distance, while at 8 cm no field nonuniformity is observable. Further investigations have also shown that incorrect positioning up to few centimeters does not appreciably affect the uniformity of the field value within the fiducial volume.

Two options are considered at this stage for the polarization the cathode and the corresponding electrodes: (a) in the first option, a HV feed-through connects an external HV power supply able to produce 200 kV to the cathode. The electrodes are placed at degrading voltage from the cathode potential to ground via a series of resistors inserted between the tubes; this solution, adopted for the ICARUS T600 setup[23], has been proven up to 150 kV; (b) in a second option, the use of a HV feed-through can be avoided if an oscillating low-voltage is multiplied inside the detector via a Greinacher circuit. Hence we consider the possibility of generating the required HV in the vicinity of the cathode, within the liquid argon, with the use of a Greinacher/Cockroft-Walton generator, as used in most commercial HV power supplies. In this configuration, each stage of the Greinacher circuit is feeding one electrode of the race track. One advantage of this solution is the absence of a resistive voltage divider. However, a drawback is the necessity to find high voltage diodes and high voltage, high capacitance capacitors which working at cold temperatures.

In preliminary tests with 20 cells we have been able to reach about 40 kV. Nearly 2 kV/cm were reached with the circuit successfully operating in liquid nitrogen. A filter was built with two RC circuits in series in order to attenuate the ripple of the DC output by $\sim$ 20 dB. These measurements indicate a very low noise level induced to the read-out acquisition channels. However, in order to solve the problem of noise generation by the AC input signal of the HV circuit, some other solution can be envisaged. One foresees the use of an input signal at 50 Hz, a frequency very far from the bandwidth of any commercial preamplifier that can be used for the wire read-out. A second possibility is to stop the AC signal when an event trigger is issued, as long as the full drift and acquisition time last.

Further tests to reach 200 kV are ongoing and long-term stability studies in cold are foreseen. The final solution will be adopted later.

8.8 Read-out electronics

A minimum ionizing particle perpendicularly crossing the wire planes induces a signal on the wires, corresponding to a charge of about 18000 electrons (depending on the wire pitch, the drift path and the drift field) per wire. The read-out electronics works as a continuous wave form digitizer for each wire.

In its baseline version, the readout system could consist of a VME-like analog board similar to that developed for the ICARUS experiment in collaboration with CAEN[5] (commercially available as CAEN V791 module), and an interface between the V791 module and the DAQ computer. Such an interface was for example developed for a test of a prototype LAr TPC in magnetic field [26, 27].

In ICARUS, each of the V791 board channels is equipped with a low-noise current integrating preamplifier followed by a flash ADC with 10 bit resolution. All channels are sampled with a rate of 2.5 MHz, *i.e.*, every 400 ns. The digitized data are continuously stored in a circular buffer in the interface, which is large enough to contain the data of all channels for a time interval corresponding to the maximal drift time (t_{dmax}). When a trigger is issued, the filling of the buffer continues for at least t_{dmax}, in order to have all the samples of the event stored in the buffer. Before the next trigger can be accepted, all the data in the buffer are transferred to a computer and stored.

The charge signal is decoupled from the wire planes, which are at a bias potential HV by a resistor and a ceramic capacitor, with a capacitance large compared to the one of the wire plus the cable. The wires are connected by Teflon insulated twisted pair cables to the the feedthroughs. Twisted pair cables are suited to be used in vacuum and in high purity liquid argon. The low capacitance of the twisted pair cables helps in suppressing the electronic noise. The same type of cables can be used to connect the read-out electronics to the feedthroughs.

[5] www.caen.it

The signal cables are connected to the backplane of a VME crate housing the CAEN V791 modules with the preamplifiers and the ADCs. One module has 32 input channels. Its function is to amplify, shape and digitize the signals coming from the detector and transmit the digitized data via a fast serial link.

The 32 input signals are sent to 32 low-noise preamplifiers and shapers. The amplifier is an integrator with a feedback time constant, with short compared to a typical signal width of about 3 μs (for ICARUS) in the "quasi current" mode and long in "quasi charge" mode, resulting in an overall decay time of about 3 μs for the "quasi current" mode and of about 30 μs in "quasi charge" mode. These time constants could be adjusted to the specific needs of the T2K LAr detector.

The amplified and shaped signals are then multiplexed and fed into four flash ADCs and then transmitted via the serial link for further digital processing. The section digitizing the signals consists of four 8-channel blocks. Each block is made of two 4-channel analog multiplexers and a 20 MHz Flash ADC. Each channel is sampled at a rate of 2.5 Ms/s and digitized with 10-bit resolution.

Recently, CAEN announced new commercial modules to be available in the beginning of 2006, which would contain up to 128 channels with 40 MHz sampling rate and 10 bits. This opens new opportunities to reconsider the design in time for exploitation at T2K. In particular, in this case the choice of ICARUS to embed both low-noise front-end electronics and the fast analog-to-digital conversion within a single electronic board could have a viable alternative in having the front-end electronics decoupled from the commercially available high-density flash-ADC boards mentioned above. Preliminary discussions with CAEN have been undertaken and also the production of hybrid boards for the front-end preamplifier has been considered. Obviously, given the relatively straightforward task of reading out signals from a liquid argon TPC, the expected time interval before commissioning of the detector, and the rapid evolution of commercial digital and analog electronics, other new electronic-readout approaches could well be considered in the near future and compared to the baseline solution outlined above, in terms of cost and performance.

9 Muon Range Detector

9.1 Overall Design

In order to increase the accuracy of the incident neutrino beam energy measurement, the WC and LAr detectors can be complemented with a Muon Range Detector (MRD). The main requirements for the MRD are as follows: the detector has to measure muon energy in the range of the expected neutrino spectrum with reasonable resolution, and the length of MRD cannot be more than 5 m due to the limited space in the underground lab.

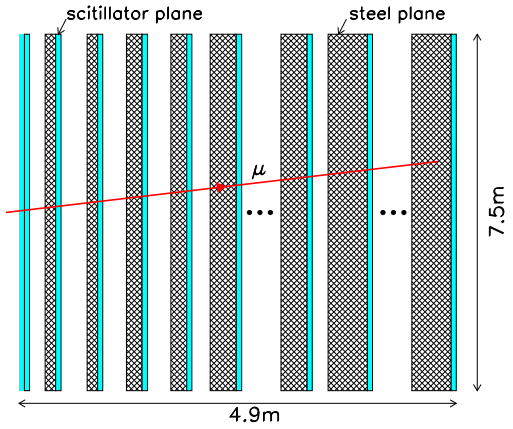


Figure 20: Setup of the Muon Range Detector.

The MRD consists of 22 steel planes, each followed by a scintillator plane. In addition, two additional 9 cm scintillator planes are placed before the first steel plane. The setup is shown in Fig. 20. The size of the MRD is 7.5 m × 7.5 m × 4.9 m. In order to maintain a relatively constant energy resolution ($\Delta E/E$) over the entire range of energies considered, the steel plane thickness increases as muon penetration increases. The first two upstream steel plates are 2.5 cm thick, the next two planes are 5 cm, the next ten layers are 10 cm thick, and the downstream eight are 20 cm. A setup with four 5 cm thick upstream steel plates was also considered. A center-to-center spacing between the upstream fourteen steel planes is 19.1 cm, with 29.1 cm between the downstream eight planes. The tracks of muons (or, more generally, charged particles) are detected by planes of plastic scintillators. The total MRD thickness (including scintillator) of 2185 g/cm^2 corresponds to muon energy of ≈3.5 GeV.

9.2 Scintillator Detector

Each scintillator plane is made up of 187 strips, each 4 cm wide by 1 cm thick and 7.5 m long. The orientation of the strips alternates by 90° in successive planes (X and Y modules) as shown in Fig. 21. Each scintillator strip has a wavelength-shifting fiber embedded in it to capture, wavelength-shift, and transport the light to either end. Both ends of each fiber are coupled through clear fibers and multiplexing boxes to multi-anode photomultiplier tubes.

Since access to the bottom of the detector is not possible after the full installation of the MRD, the multi-anode PMTs are placed to the side of the MRD steel planes. Our baseline design uses the Hamamatsu H8804, which is a 8×8 multi-anode PMT with each anode measuring 2 mm×2 mm. This PMT has been

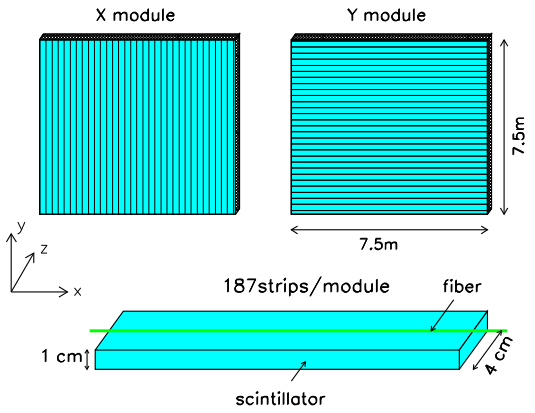


Figure 21: Sketch of the scintillator planes and plastic strips.

used for the K2K SciBar detector successfully. 144 such PMTs are used to read out all MRD scintillators, if signal multiplexing is not performed.

9.3 Readout Electronics

The readout electronics system will be similar to that of the K2K SciBar detector. In our baseline design, the readout electronics system consists of front-end electronics attached to the multi-anode PMT and a back-end VME module.

A combination of ASICs (VA32HDR11 and TA32CG made by IDEAS) are used on the front-end electronics. VA is a 32 channel preamplifier chip with shaper and multiplexer. TA provides timing information after taking the OR of the 32 channels. Two packages of VA and TA are mounted on a custom-designed PCB board (Front-End Board, FEB) to read out signals from the 64 anodes from a PMT.

A back-end electronics board (DAQB), which is a standard VME-9U board, controls and reads out 8 FEBs. The charge information from the PMT is digitized with a 12-bit flash ADC and read out through the VME bus. The timing information is processed and recorded by a multi-hit TDC.

Performance of the MRD has been evaluated with a simulation study; results are given in Section 10.3.

10 The 2KM Detector Simulation and Performace

This section describes the simulation software and the determination of detector sensitivities for the various subdetectors of the 2KM detector complex. The application of these studies towards evaluation of efficiency and purity of the reconstructed ν_e samples will be covered in Section 11.

10.1 Water Cherenkov Simulation Results

The water Cherenkov simulation code is based on Geant4, and reads input neutrino and particle vector files and outputs ROOT files which can then be processed by ROOT or converted and processed by the standard K2K and Super-Kamiokande reconstruction software [28].

10.1.1 Validation and Initial Tuning using K2K 1kton Data

The water Cherenkov part of the code has been made flexible: we can adjust both detector size and layout including the size of the PMTs. This allows us to simulate any water Cherenkov detector, and to compare against the 1kt tank at K2K, for which we already have a large data set of beam neutrinos as well as cosmic ray muons. We are presently using these to validate the GEANT4 MC by:

- simulating the K2K 1kt tank's configuration with our GEANT4 MC,
- comparing the output between the GEANT4 1kt-configured code for cosmic ray data and K2K beam neutrino interactions,
- tuning various parameters such as water scattering to get reasonable agreement, and
- comparing the tuned GEANT4 output against K2K neutrino interactions.

In order to do this we have generalized the Super-Kamiokande/K2K reconstruction code and converted the ROOT output from our MC into a format readable by the Super-Kamiokande tools. We were then able to run the full Super-Kamiokande reconstruction suite on the output of the MC.

We first compared the MC performance by comparing with 1kt vertical through-going muon data. Vertical through-going muons are minimum ionizing particles and produce a clear Cherenkov cone; they are a well-known calibration source at Super-Kamiokande and the K2K 1kton detector. We used the same input for the GEANT4 MC as is used at K2K for simulating through-going muons, and the same through-going muon fitter. An example of this comparison is shown in Figure 22, where the total charge collected by all of the PMTs in the tank is shown for the GEANT4 MC and actual 1kt data. This first stage allows us to tune the charge scale (amount of Cherenkov light emitted by a minimum-ionizing particle per unit track length) and measure the amount of indirect light (scattered and reflected light outside the Cherenkov cone). The results are shown in Figure 22. After this initial tuning, the charge scale difference between data and MC was $1.8\% \pm 0.2\%$.

For the second stage of the validation, we simulated K2K beam ν_μ events using the same neutrino flux and neutrino interaction simulation as the K2K 1kton group. These events were processed using the full 1kton reconstruction suite. In order to check the energy scale, neutrino-induced π^0 events were selected: a single π^0 enriched event sample was obtained by selecting 2-ring e-like events (*i.e.* events where two tracks are found and identified as electromagnetic showers). Figure 23 shows the invariant mass distribution for those events with π^0 mass peak. The relative difference between the data and GEANT4 MC peak is $-6.0\% \pm 0.7\%$. The peaks for both the data and MC are shifted slightly higher than the true π^0 mass, which can be accounted for by vertex reconstruction biases and extra energy deposited by γ's from deexcitation of oxygen nuclei. The differences between data and MC for through-going muons and neutrino events are mostly caused by a slight excess of indirect light in the MC, which affects the Cherenkov ring patterns and energy determination. They can be corrected for by adjusting the reconstruction software[6]. These results confirm that the GEANT4 simulator is suitable for studying other detector geometries.

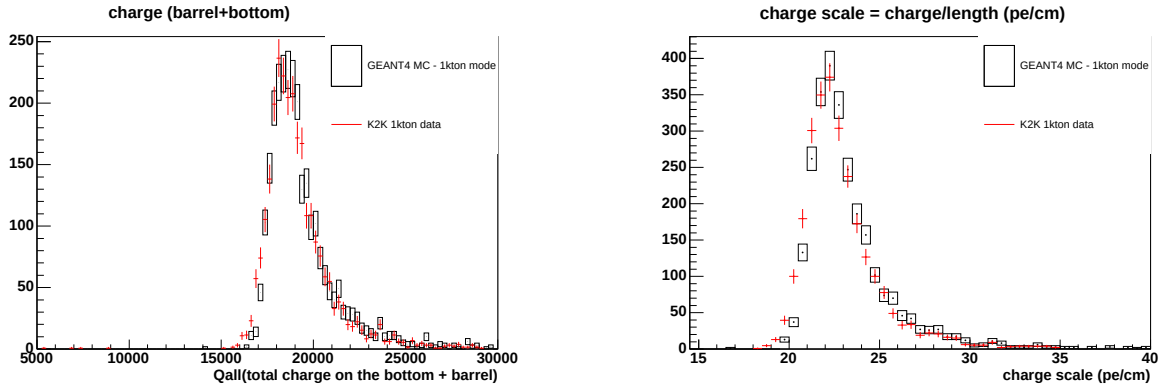


Figure 22: Left: Comparison of collected charge from the PMTs in events between the GEANT4 simulation configured with the geometry of the K2K water Cherenkov tank and real downward going muon data. Right: similar comparison for the charge per track length distribution.

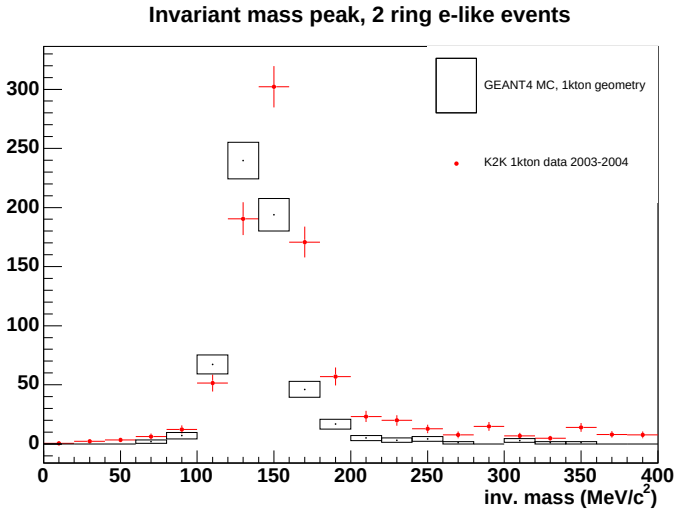


Figure 23: Comparison of the invariant mass peak for 2-ring e-like events from K2K 1kton data and GEANT4 MC configured with the geometry of the K2K water Cherenkov detector. ν_μ MC events were simulated using the K2K spectrum and neutrino-water interaction model.

As can be seen, after our initial tuning, there is quite good agreement. After tuning and comparing with K2K 1kton data, the GEANT4 simulator was used to simulate the geometry relevant for the T2K experiment.

10.1.2 Selection of a Configuration to Match Super-Kamiokande Resolution

The philosophy behind the design of the K2K water Cherenkov detector was to use exactly the same hardware and electronics as in Super-Kamiokande so as to cancel out as many systematic errors between the two detectors as possible. For T2K we have adjusted this philosophy slightly. We are designing the

[6]This is not done for the comparison with K2K data, in order to check the performance of the simulator itself.

detector to match the response of the near detector at 2 km with Super-Kamiokande, even if it means using a different hardware configuration. This means choosing a configuration which has the most similar response to Super-K when reconstructing physics quantities. An example of this philosophy is the choice of the size and number of PMTs. One option is to use the same size PMTs as K2K and Super-Kamiokande. However, the number of PMTs, and hence the ring resolution is greatly reduced due to the relatively large "pixel" size. Another option is to use a larger number of 8-inch PMTs. Although the physical size of the PMT is different, the number (5660 vs. 841) is much closer to Super-Kamiokande's, and the relative pixel sizes are similar. Figure 24 demonstrates this effect. In these figures, a π^0 is simulated decaying in the Super-Kamiokande detector, and in a 2KM water Cherenkov detector with 8-inch and 20-inch PMTs. As can be seen, qualitatively the 8-inch case looks more like Super-Kamiokande.

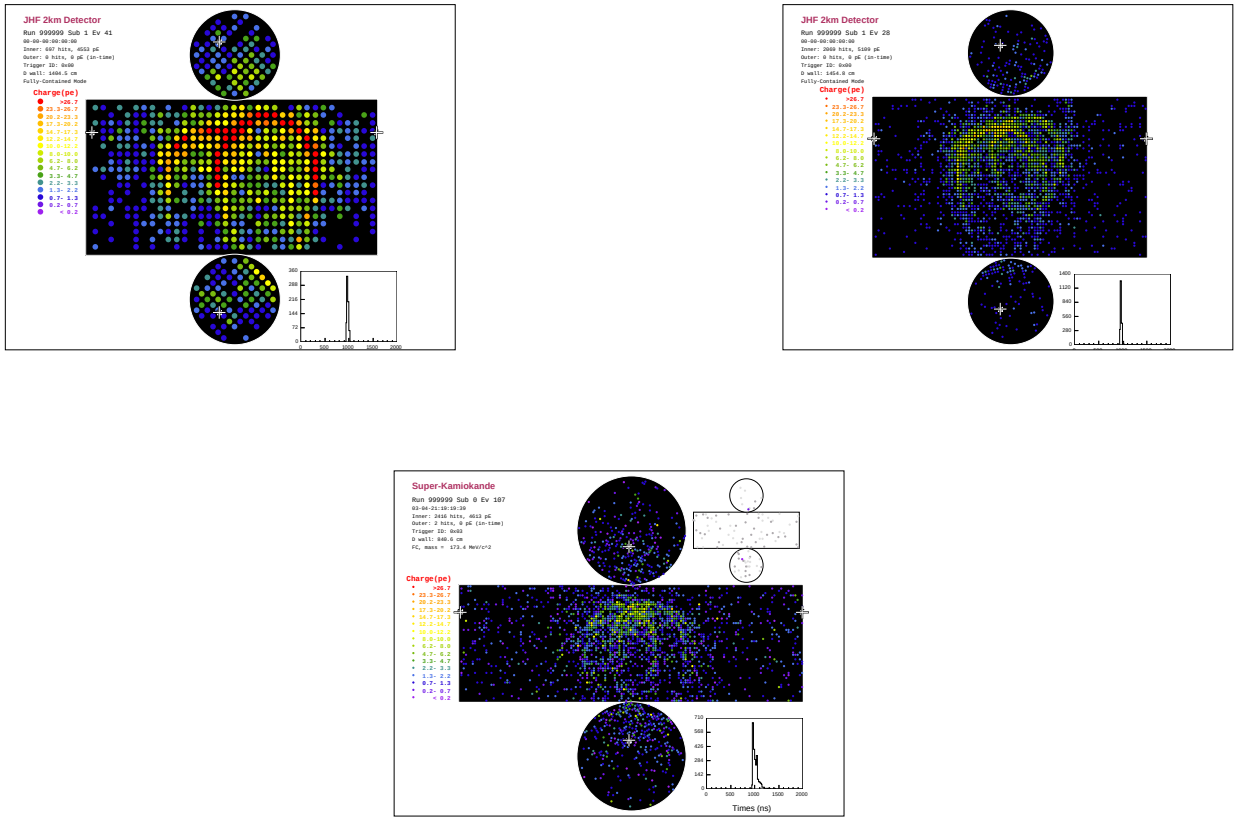


Figure 24: A simulated NC π^0 event in the 2KM WC detector with 20-inch PMTs (top left) and 8-inch PMTs (top right). A simulated NC π^0 event in the Super-Kamiokande detector is shown for comparison (bottom). Based on studies with this simulation, we have concluded that it is preferable to use a larger number of small 8-inch PMTs than a smaller number of 20-inch PMTs.

We have done quantitative studies to determine the optimum configuration for matching relevant Super-K resolutions and efficiencies. We have studied single-ring muon selection efficiency, ring-counting and particle identification (PID: classification into e-like (showering) or μ-like (non-showering) particles.) In order to apply this reconstruction software to a detector equipped with 8-inch PMTs, careful modifications had to be made to the reconstruction code. As an example, Figure 25 compares single-ring event selection efficiencies for T2K ν_μ interactions, which are summarized in Table 3: for reconstructing single ring muons, we can achieve an event selection efficiency the same as Super-Kamiokande's to within 1% for 8-inch PMTs. The difference is 5% if 20-inch PMTs are used.

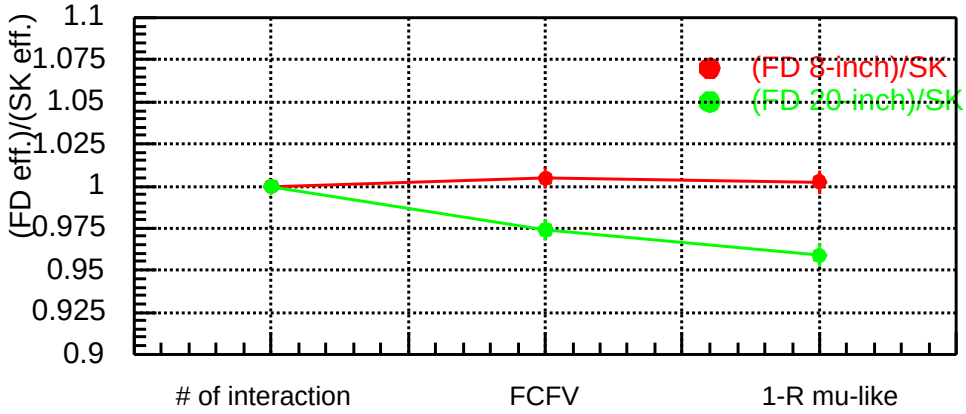


Figure 25: Comparison of efficiencies of ν_μ events in fiducial volume for each event selection step. Ratios of efficiencies to Super-K's are shown in lower figure (8-inch:red, 20-inch:green).

	8-inch	20-inch	Super-K
# of int.	100	100	100
FCFV	52.5	50.9	52.2
1-R μ-like	37.7	36.0	37.6

Table 3: Efficiency (percent) of ν_μ event selection in fiducial volume of water Cerenkov detectors (2KM detector and Super-K).

Figure 26 shows the PID likelihood distribution of muons produced in the fiducial volume of the Cherenkov detector. We used charged current quasi-elastic events generated for the T2K muon neutrino beam at the 2KM detector site. The distributions obtained for both the 8-inch and 20-inch PMT configurations are compared so as to reveal the shape difference of the distribution. The events for which the likelihood parameter value is less than zero are misidentified as electrons. Clearly, the tail of the distribution has a more sharply cut off tail, and fewer misidentified events than in the 8-inch case. Therefore, we conclude that better PID performance can be expected from the 8-inch configuration.

We conclude from these studies that a configuration with a larger number 8-inch PMTs is superior to one with fewer 20-inch PMTs.

10.1.3 Event Reconstruction Performance with Selected Configuration

After making the choice of 8-inch PMTs based on the above studies, further performance studies were done with this configuration. The results are given in this section.

Monoenergetic $e^-$and μ^-events ranging from 30 MeV/c (150 MeV/c for μ^-) to 1500 MeV/c, emitted isotropically from random vertices, were simulated and reconstructed using the Super-Kamiokande/K2K software suite.

All stages of the reconstruction were checked: first the vertex (and first ring) fitter finds the position of the vertex (and the direction of the most visible ring) using timing and charge information. Then, using the vertex position information, the ring counting program determines the number of Cherenkov rings and their directions by a maximum likelihood method. Rings are classified by the PID program which determines whether the ring is e-like (a showering particle) or μ-like (a non-showering particle) using another maximum likelihood method. Using this PID information the vertex of single-ring events is further refined. Throughout the entire process a ring separation program is used to apportion the charge of each PMT between the rings. The momentum of each track is then estimated from the amount of charge detected in a 70° half-opening angle around the reconstructed direction.

The performance of the vertex fitter is summarized in Figure 27, for T2K beam neutrino MC events. Ring counting efficiency was estimated for mono-energetic single track events, and also for quasi-elastic neutrino scattering events. Figure 28 demonstrates that our detector performs similarly to Super-Kamiokande. For the study of momentum resolution, single ring mono-energetic MC events were used. First we studied the momentum determination itself: Figure 29 shows the relation between the corrected amount of Cherenkov light and the true particle momentum. It is linear for e^-, but not μ^- because of the non-negligible muon mass. In Figure 30 the momentum resolution is also displayed, along with the best fit. In this study we estimate momentum resolution to be $\sim \pm 3.1\%$ for $\mu^-$and $\sim \pm(3.1 + 1.3/\sqrt{P(\mathrm{GeV})}\%$ for e^-.

In Figure 31, the PID misidentification probabilities of Super-Kamiokande and the 2KM detector (8-inch case) are compared. Electrons and muons were generated within the fiducial volume with a monoenergetic spectrum, then standard event reconstruction was applied. It is important to keep PID performance at the same level as Super-Kamiokande because the acceptance of muon neutrino events is then similar, as is the reduction of the background of $\nu_\mu \rightarrow \nu_e$ appearance measurement. Mis-identification probabilities are similar and less than about 1.5% for both detectors, for almost all energies.

10.2 Liquid Argon Simulation Results

The liquid argon simulation code is also based on Geant4. Further details on the reconstruction techniques described in this section can be found in references [29, 23].

10.2.1 Hit, cluster and track reconstruction

The liquid argon event reconstruction goal is to extract the physical information contained in the wires output signal, *i.e.* the energy deposited by the different particles and the point where such a deposition occurred. This allows us to build a complete three dimensional spatial and calorimetric picture of the event.

The basic energy deposition unit is the hit, defined as the segment of track whose energy is read by a given wire of the read-out planes. Therefore, the spatial and calorimetric information of the track segment is contained in the associated hit, and the sensitivity of the detector entirely depends on the hit spatial and calorimetric resolutions. Hits are grouped into clusters representing common charge composition distributions, such as tracks or showers. 3D hit reconstruction then determines the space coordinates of the ionizing particles traversing the LAr volumes. The 3D hit reconstruction performs most efficiently on events of low track multiplicity (which is the case for most of the events which will be recorded in the T2K beam).

10.2.2 e/π^0 separation

This section presents a Monte Carlo study of the e/π^0 separation capability by dE/dx and log-likelihood methods. The main decay mode of π^0 is $\pi^0 \rightarrow \gamma\gamma$, which may initiate an electromagnetic shower and fake an electron. Especially when the early decayed photon converts into a collimated electron and positron pair, a

pion may be mistaken as a single electron. However, before the shower starts, the minimum ionizing particle (mip) signal of the e^-e^+ pair should be twice as much than of the signal of a single electron. Therefore, a simple dE/dx measurement is expected to provide an efficient way to reject the π^0 background.

The electron/pion separation by the dE/dx method has been studied with 1000 electron and pion events produced by full simulation with digitization and noise inclusion at energies from 250 MeV to 2 GeV. Fig. 32 shows the typical ionization imaging of electron (top) and pion (bottom) in the collection view.

A separation method using the average dE/dx of the first 8 wires (2.4 cm of track length) was applied to electrons and pions with energies of 0.25 GeV, 0.5 GeV, and 2 GeV. We found that the fraction of surviving pions decreases as the incident energy increases This is due to the decrease of Compton scattering, the main source of the contamination, whose cross-section is approximately inversely proportional to the photon energy in this energy range. Fig. 33 plots the surviving pion fraction as a function of the incoming energy and the corresponding exponential fit.

In addition to the above discussed method, one can observe that the mean free path of a photon for pair production in liquid argon is 18 cm ($\lambda_{pair} \simeq \frac{9}{7} L_{rad}$ where $L_{rad} = 14$ cm). Therefore, if the vertex of the event is known, one can visually recognize a pion if it converts after more than 1 cm. After scanning, we find 5.4% of pions are confused as electrons. Combining this method with $\langle dE/dx \rangle$ method one can aim at an overall 0.2% pion efficiency by imaging.

10.2.3 Hadron identification

We discuss here results obtained with an automatic reconstruction procedure combined with a neural network to separate muons, pions, kaons, and protons that decay or stop inside the active detector volume. The information provided by the particle before and after it loses all its energy and decays or stops can be combined. The study of the hits recorded before (and close to) the parent particle decay/stopping vertex is essential. Due to the mass differences, for energies below the minimum ionizing value, each particle exhibits a distinct $\langle dE/dx \rangle$ behavior as a function of its kinetic energy. The study of the activity after the parent particle decay vertex can be helpful to disentangle harder (kaons) from softer (pions and muons) decaying particles. In the case of protons, the absence of decaying products gives an even more clear signature.

The four plots in Figure 34 show how muon, pion, kaon and proton events (from top to bottom, respectively) are classified as muons, pions, kaons and protons (from left to right, respectively) from the multi-layer perceptron neural network. The numbers inside the plots give the fraction of events tagged in each category. The detector offers excellent particle identification capabilities, with quoted efficiencies for protons, kaons and pions-muons above 99% and contaminations below 1%. The muon/pion inter-contamination is found to be at the level of $\sim 25\%$.

10.2.4 Event reconstruction, selection and classification

Neutrinos interacting inside the LAr detector give rise to different types of events. Figures 35, 36 and 37 show typical examples of ν_μ CC, ν NC and ν_e CC events, respectively. To discriminate these interaction types, we preliminary set up two fully automatic and computer-based procedures able to perform an event classification with high efficiency and low contamination of the events expected at T2K. Further studies are ongoing and improvements are still expected once the algorithms are perfected.

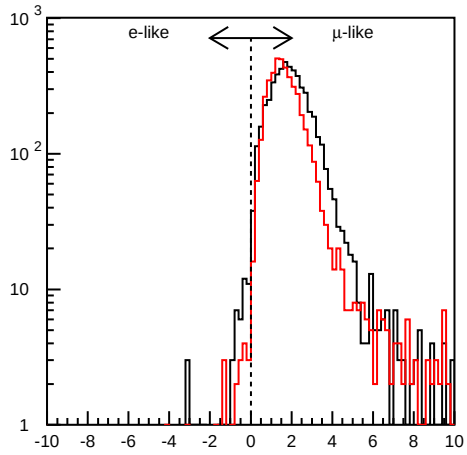


Figure 26: Likelihood parameter of particle identification estimated by muons produced in the 2KM Cherenkov detector. The distribution obtained with the 8-inch PMTs configuration (red) shows a sharper cutoff feature and smaller misidentification probability compared to 20-inch PMTs (black). These results support the choice of 8-inch PMTs.

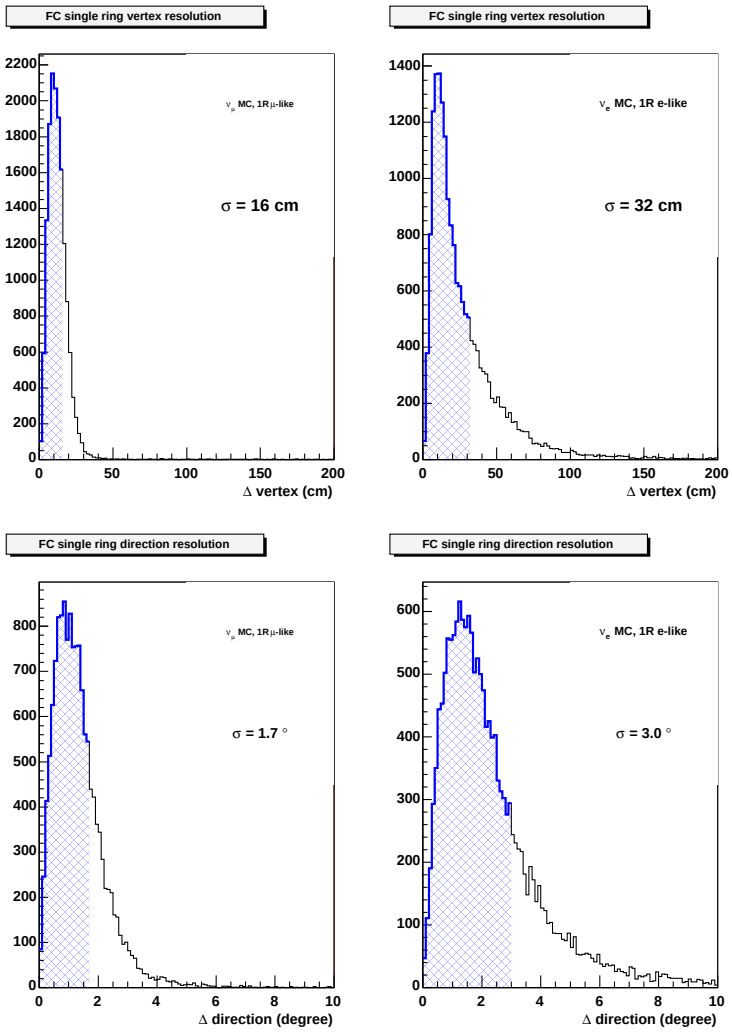


Figure 27: Vertex and angular resolution of the final vertex for 1 ring events for the 8 inch configuration. The hatched region corresponds to 68% of the events.

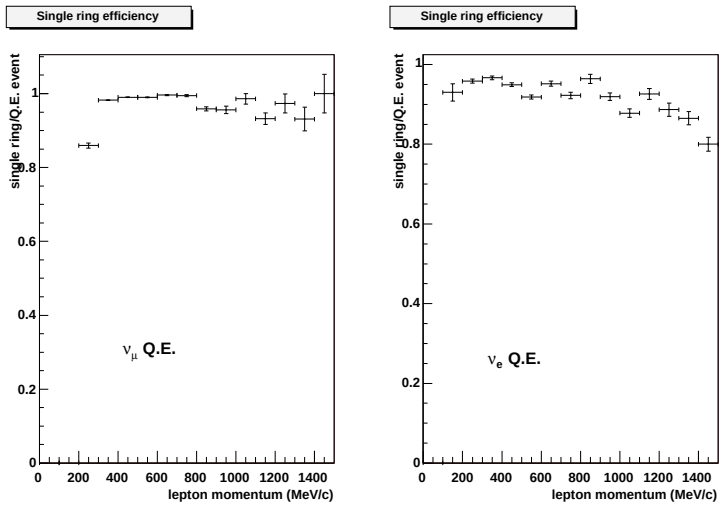


Figure 28: Ring counting efficiency for T2K beam charged current quasi-elastic ν_μ and ν_e events. The ring counting selection efficiency is close to 1 over the whole energy range, showing good performance of the ring counting software for the 2KM detector with 8inch PMTs.

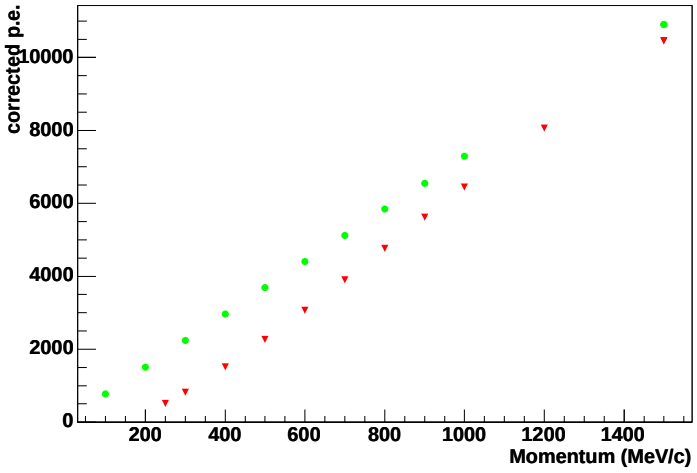


Figure 29: The relation between corrected Cherenkov light and momentum for single ring electron (green circle) and muon (red triangle) events.

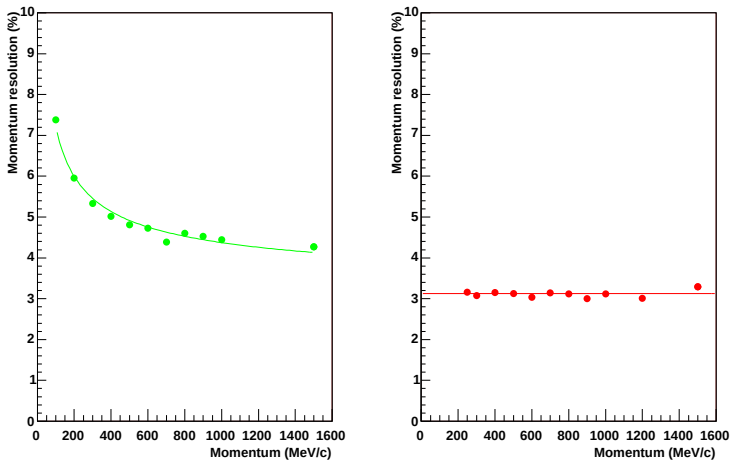


Figure 30: Momentum resolution for single ring fully-contained electrons (green) and muons (red).

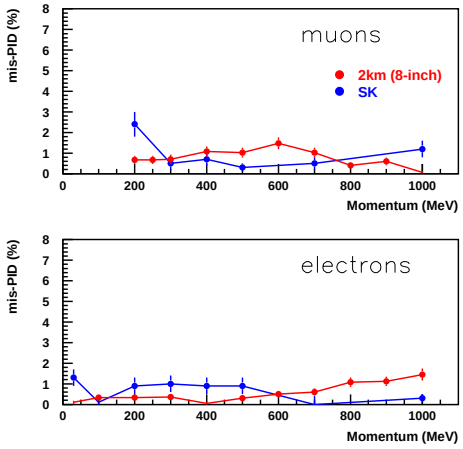


Figure 31: Mis-identification probabilities for the 2KM detector (8-inch PMTs case) and Super-Kamiokande for several energy ranges.

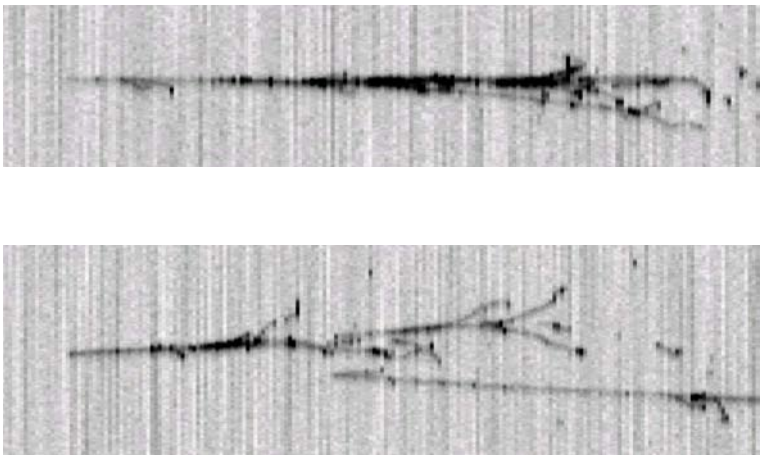


Figure 32: Simulated imaging of an electron (top) and a pion (bottom) for the collection view. The grey level measures the amount of deposited energy. The single mip track of the electron and the double mip track of e^-e^+ from π^0 decay are clearly distinguishable.

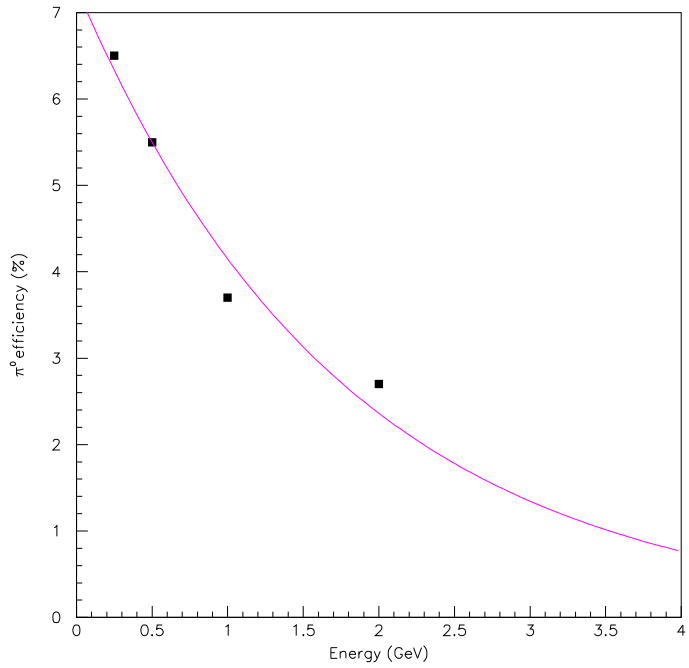


Figure 33: Survival π^0 efficiencies as a function of the incoming energy. The points are simulations and the curve is the result of an exponential fit.

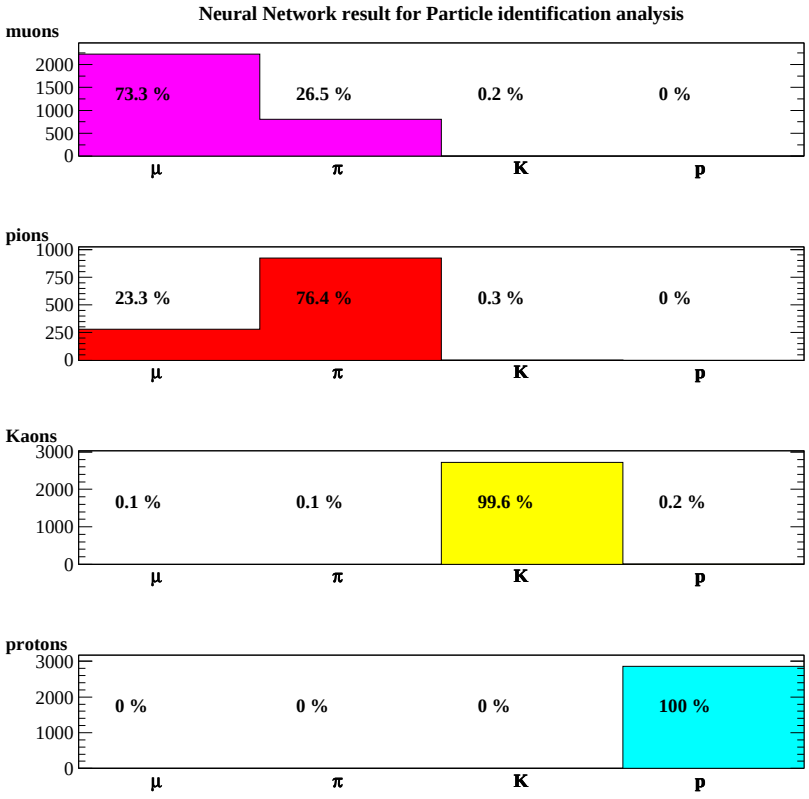


Figure 34: Multi-layer perceptron Neural Network analysis results on particle identification. The histograms (from top to bottom) show how each type of particle gets classified in different categories (bins from left to right).

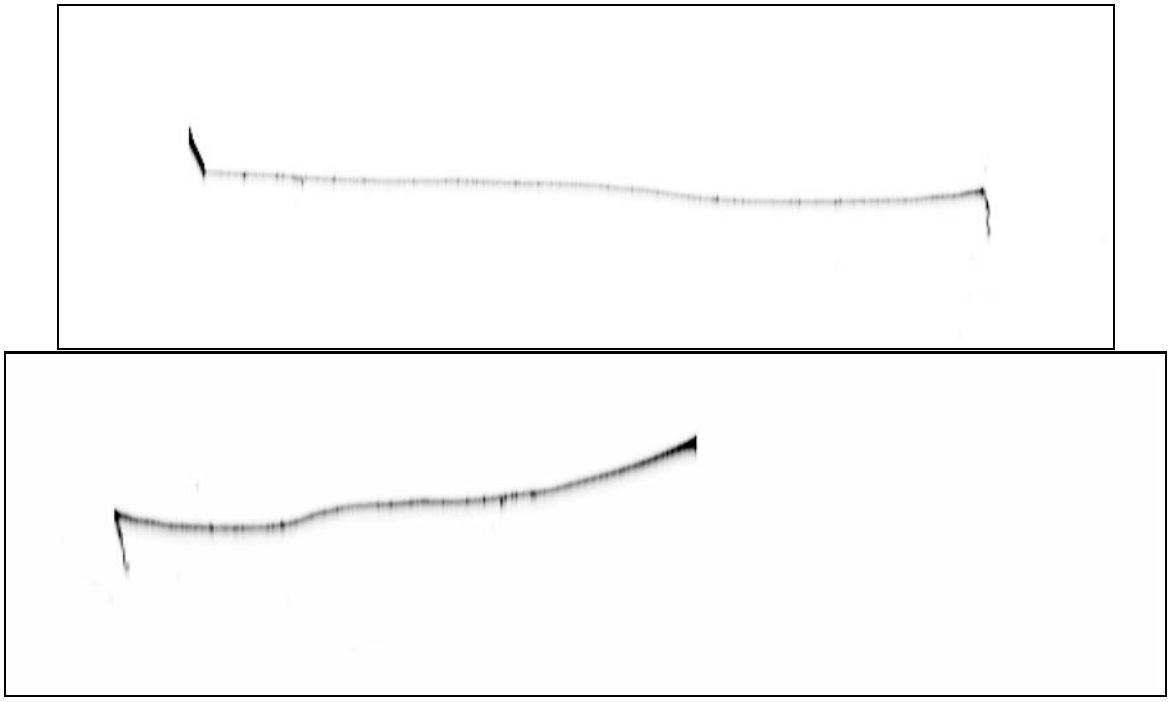


Figure 35: Example of ν_μ charged current event, in collection view and induction view. The energy of the original ν_μ is 811 MeV and the momentum of the μ is 735 MeV.

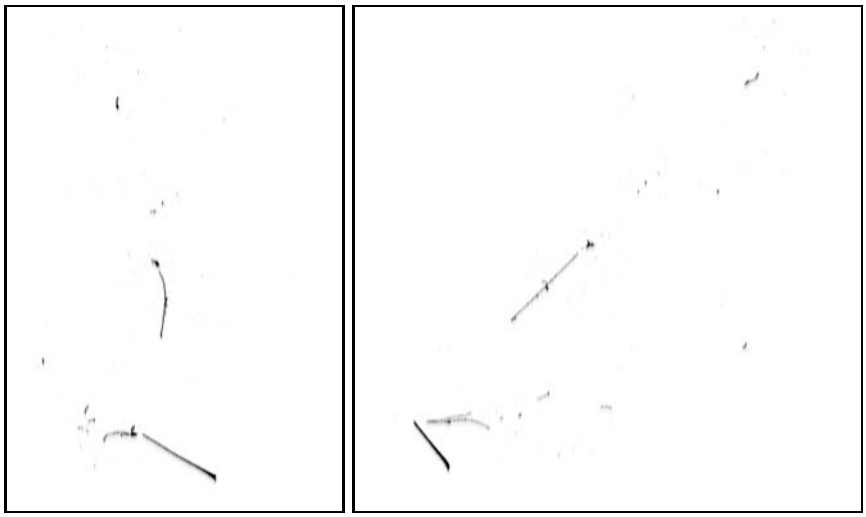


Figure 36: Example of ν_μ neutral current event, in collection view and induction view. The energy of the original ν_μ is 787 MeV. A proton and a π^0 are produced.

As mentioned, we have evaluated two independent methods applied for event classification: one method is a cut-based selection of muon charged-current quasi-elastic events using simple topological variables, and the other is based on the "Random Forest" method.

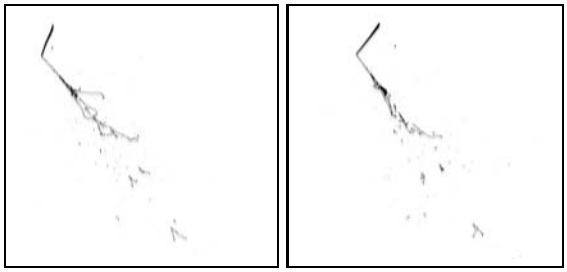


Figure 37: Example of ν_e charged current event, in collection view and induction view. The energy of the original ν_e is 755 MeV and the momentum of the electron is 603 MeV.

The results of the first cut-based method are shown in Figure 38. The criteria chosen to cut off the ν_μ NC background result in degradation of the efficiency at low energy, as can be seen in Fig. 38. On average, the cut efficiencies are 90.64% for QE ν_μ CC events and 4.05% for ν NC background. Normalizing to the expected flux of the neutrino beam at the 2 km site, this result implies that already with a simple cut analysis, it will be possible to select 110000 QE ν_μ CC events per year with only 1100 surviving ν NC events, corresponding to a 1% background.

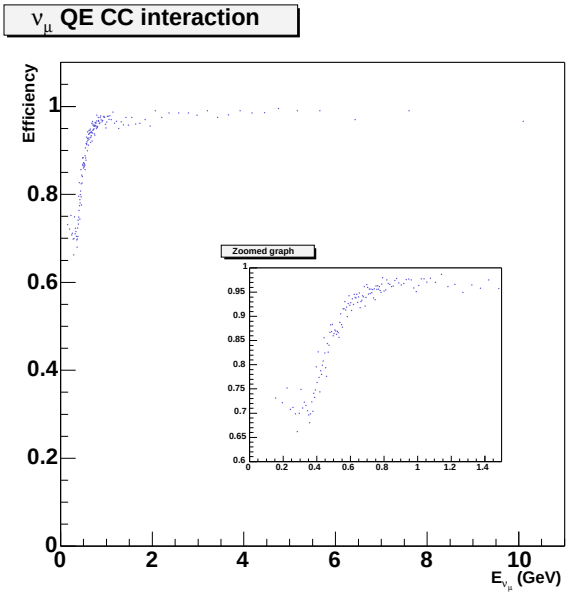


Figure 38: Efficiency for selecting QE ν_μ CC events as a function of the true neutrino energy.

The upper part of Table 4 shows the result obtained from a Random Forest analysis based on eight input variables. The algorithm clearly separates the two types of charged currents events. For example, the ν_μ CC sample gets correctly classified 86% of the time, while a lower efficiency is obtained for neutral current identification. This is not surprising since in this approach no kinematics information is used and no attempt is made to identify muons, pions, π^0, *etc.*

In a further Random Forest stage, kinematics and particle ID information are included. By using 3D hits, the event total transverse momentum is computed. This is expected to be large for neutral current events and small in the case of charged current interactions. In addition, the methods of Section 10.2.3 are

Table 4: Event classification results based on Random Forest analysis.

classification approach	original sample	events classified as: ν_μ CC	ν NC	ν_e CC
topology	ν_μ CC	86.0 %	10.9 %	3.1%
	ν NC	8.7 %	70.6 %	20.7%
	ν_e CC	3.7 %	11.5 %	84.8 %
topology + kinematics, PID	ν_μ CC	95.2 %	2.5 %	2.3 %
	ν NC	3.1 %	90.0 %	6.9%
	ν_e CC	1.8 %	3.6 %	94.5 %

applied to identify muons, pions and protons. These new variables are inserted in the Random Forest and the classification algorithm run once again over the same training and test samples. The results are shown in the lower part of Table 4. For neutrino charged current interactions, the proposed algorithm shows a 95% efficiency. The event misclassification and contamination from different samples is at the level of a few percent. ν_e CC events with prompt electrons, that are soft and therefore do not produce showers, constitute the largest fraction of events mistaken as ν_μ CC or ν NC events. In the case of ν_μ CC events, soft muons accompanied by π^0 showers wrongly taken as primary particles, are classified as ν_e CC.

The inclusion of kinematics and particle ID appreciably increases the efficiency for NC classification (the adopted approach predicts a 90% efficiency). For NC, the largest source of confusion comes from events where a photon induced shower is taken as a primary electron. This confusion is large because the algorithm concentrates on track reconstruction and contains a preliminary shower reconstruction package. Therefore, it does not incorporate the methods of Section 10.2.2 devised to distinguish electrons from π^0s, and further improvements are confidently expected.

Fig. 39 shows the classification efficiency as a function of the incoming neutrino energy. We see that the classification efficiency is essentially flat as a function of the energy. This is a crucial issue when trying to study muon disappearance oscillations.

These preliminary studies show that already at this stage it is possible to conceive fully automatic, computer-based reconstruction of bubble-chamber quality images. Hence, the quasi-online handling of the large number of events expected at T2K seems to be an achievable task.

10.2.5 Muon momentum resolution

In this section we discuss the stand-alone measurement of the track momentum via the multiple scattering method. In particular, this method can be effectively used for tracks escaping the detector. For example, prompt muons emerging from ν_μ CC interactions have momenta around 1 GeV. Since a mip particle deposits approximately 200 MeV per meter, a large fraction of those muons are only partially contained. On average the distance traveled in liquid argon will be several meters long. For escaping tracks, calorimetric techniques cannot be used to precisely measure the energy. However, the multiple scattering method can provide a good estimate of the momentum, even in absence of an external magnetic field. Of course, escaping muons will also be measured by the downstream WC detector.

In order to best employ the information coming from a multiple scattering measurement, an estimate of the muon momentum can be obtained by the fitting technique known as Kalman filtering (detailed discussions of the method can be found in [30, 31]). Taking into account the information provided by multiple Coulomb scattering, the Kalman filter technique allows to measure the muon momentum on a track-by-track basis. In order to evaluate the accuracy of the method, we have fully simulated and reconstructed 1000 muons for energies from 0.5 to 3 GeV. An example of the resolution study results is shown in Figure 40.

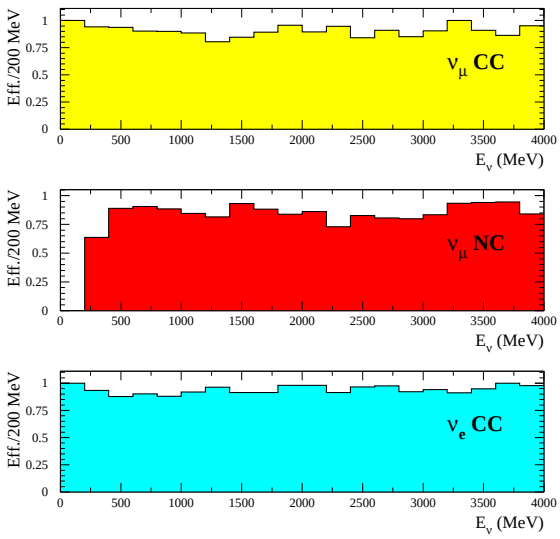


Figure 39: Classification efficiency as function of the incident neutrino energy.

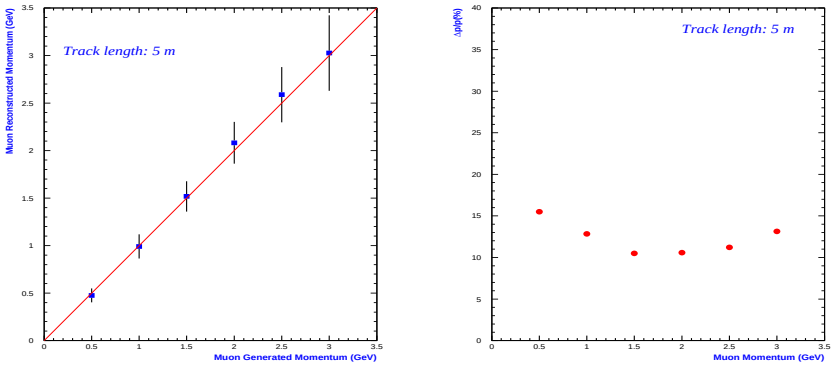


Figure 40: (left) measured momenta using the Kalman Filter versus the generated Monte Carlo momenta; (right) expected muon momentum resolution as a function of muon energy for a given track length.

From this study one can conclude that for a large fraction of the neutrino events taking place, the Kalman Filter technique is able to determine very accurately the momentum of individual tracks. Provided that tracks are long enough, one expects resolutions around 15%. This fact combined with the good resolution expected for the measurement of the hadronic system, means that a precise determination of the event kinematics can be obtained even for events where the muon is only partially contained. Combining this with the information from the WC detector will still improve the reconstruction.

10.2.6 Neutrino and hadron energy resolution

We discuss here the capability to derive the neutrino energy by using two different methods, and we compare the results. In order to infer the interacting neutrino energy one can use both a calorimetric and a tracking approach. The calorimetric approach simply consists in measuring the kinetic energy released in the detector. The tracking approach, instead, consists in identifying all particles and converting the deposited energy (kinetic energy) into momentum knowing the mass. This approach relies therefore on the capability to perform a good particle identification.

The two methods used to reconstruct the neutrino energy studied here are based on a tracking approach and consist in measuring only the muon energy and on measuring the muon and the hadronic energy, respectively. The former method is effective for QE events assuming a fixed kinematics (*i.e.* ignoring Fermi motion) and the neutrino energy can be calculated as

$$E_\nu^{rec} = \frac{m_N - \frac{m_\mu^2}{2}}{m_N - E_\mu + p_\mu cos\theta_\mu} \tag{5}$$

The latter method relies on conservation of momentum:

$$E_\nu^{rec} = |p|_\nu^{rec} = \sqrt{(\Sigma p_x)^2 + (\Sigma p_y)^2 + (\Sigma p_z)^2} \tag{6}$$

Fig. 41 shows the visible neutrino energy plotted against the true energy. It is evident that, by only measuring the muon there are many events where the reconstruction is not efficient; these are mainly non-QE (nQE) events. Fig. 42 shows the difference between the true neutrino energy and the reconstructed one, and the resolution on the reconstructed energy obtained using the two methods, where we have applied a cut on the visible energy of 1250 MeV (the relevant range for observing neutrino oscillation). The number of events where the reconstruction is not efficient is drastically reduced for the case of full reconstruction (*i.e.* measuring the hadronic energy) but it is still large in case of the muon standalone reconstruction. The conclusion is that, by measuring hadronic energy one can reconstruct the neutrino energy with a Gaussian resolution of $\sim 22\%$, whereas measuring just the muon energy degrades the resolution by $\sim 10\%$ and makes it non-Gaussian.

10.2.7 Event Kinematics Reconstruction

One of the goals of the proposed detector is the measurement of the QE/non-QE events ratio. To achieve it one has to study the kinematics of the events. In particular, one has to analyze the distribution of the 4-momentum transferred (Q^2) and the invariant mass of the hadronic system (W)

$$Q^2 = E_\nu E_\mu \sin^2 \frac{\theta}{2} \tag{7}$$

$$W^2 + Q^2 = 2M\nu + M^2 \tag{8}$$

$$\nu = E_{had} - M = E_\nu - E_\mu \tag{9}$$

In Fig. 43 the invariant mass distribution obtained from simulations (generator level) is compared to the distribution obtained after applying the reconstruction process. It is evident that for the case of QE

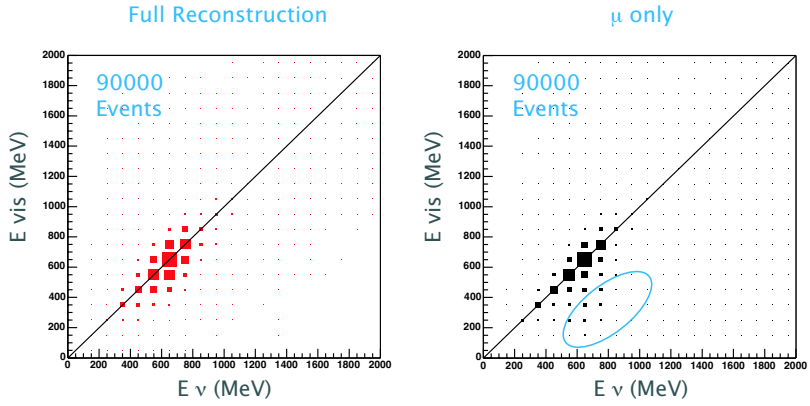


Figure 41: Visible energy *vs* true neutrino energy obtained by measuring both muon and hadronic energy (left) and only the muon energy (right). The region selected (right) contains mainly non-QE events not well reconstructed by only measuring the muon energy.

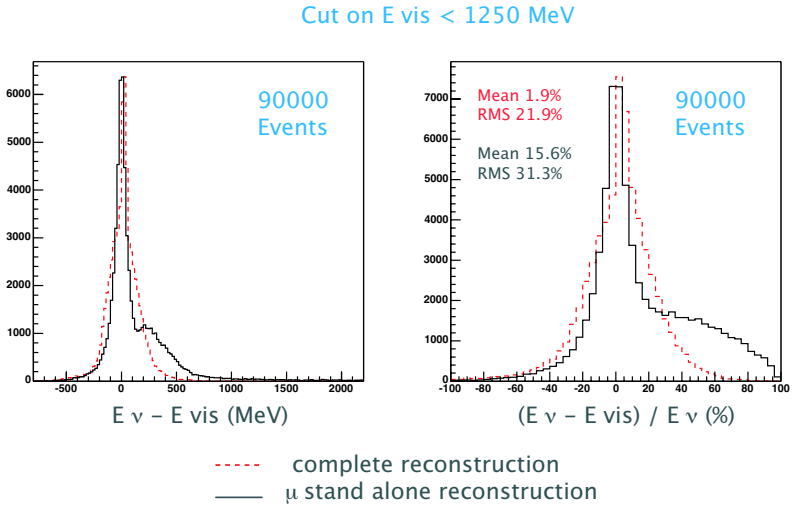


Figure 42: Difference between the true neutrino energy and the reconstructed one (left), and resolution of the reconstructed energy (right) after applying a cut of 1250 MeV on the visible energy. The solid gray line shows the results obtained measuring only the muon whereas the dashed red line shows the results obtained taking into account the hadronic energy.

events, the resolution on W is not affected at all by the reconstruction process, whereas it is slightly affected in case of non-QE events.

The same analysis has been carried out on the distribution of 4-momentum transferred. In Fig. 44 the distribution of Q^2 is shown with and without the effects of the reconstruction. Once again, for QE events the resolution is not affected by the reconstruction process, whereas for non-QE events it is slightly degraded. The conclusion is that given the resolution that we obtain on Q^2 ($\sim$16%) and W ($\sim$10%) the discrimination between QE and non-QE events seems quite promising. This study is on-going.

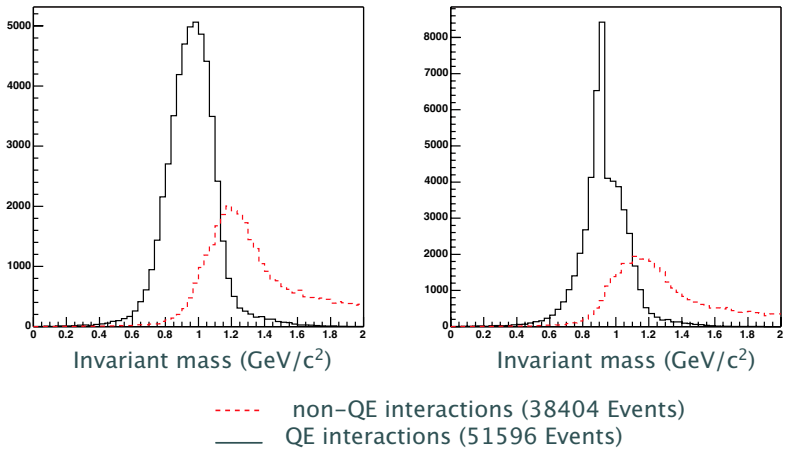


Figure 43: Invariant mass reconstructed from Monte Carlo events at the generator level (left) and after applying the reconstruction process (right). The solid grey line shows QE events whereas the dashed red line shows non-QE events.

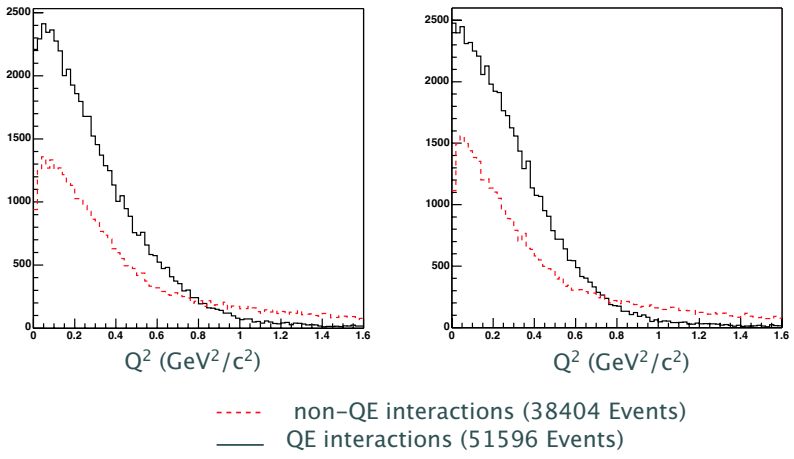


Figure 44: 4-momentum transferred reconstructed from Monte Carlo (generator level) (left) and after applying the reconstruction process (right). The solid grey line shows QE events whereas the dashed red line shows non-QE events.

10.2.8 Events in the Inner Target

In this section we present the capability of the proposed detector in reconstructing events that take place inside the inner (water) target. In particular, we estimate the fraction of the energy that different particles release inside the LAr volume. For this analysis 3000 QE events and 3000 resonance events have been generated. In these events Fermi motion has been accounted for, and reinteraction on oxygen has been included. These events have been generated at $x = 0$, $z = 0$ and y randomly chosen inside the target ($\pm$12.5 cm) with a flat distribution. The inner target is the parallel plate configuration in which $\sim$ 10240 ν_μCC events are expected to take place per year. For each particle generated in the neutrino interaction we define a factor f which is the ratio between the reconstructed and the true generated momentum:

$$f = \frac{|p|_{rec}}{|p|_{MC}} \tag{10}$$

In Fig. 45 the distribution of f for 3034 protons in QE events is shown. Almost 30% of the protons escape from the water target and release energy in the liquid argon volume making possible their identification. If we request that the energy released in the active volume be larger than 50 MeV, usual cut-off for proton identification, we reconstruct $\sim$ 22% of the interactions; this means that we would reconstruct $\sim$1450 QE interaction per year taking place in the inner target.

A similar analysis shows that the fraction of particles that can be reconstructed is $\sim$ 25% for protons and $\sim$ 85% for both π^+ and photons from π^0. After applying a cut-off on the released energy for protons (50 MeV) and π^+ (10 MeV), we fully reconstruct $\sim$ 17% of the interactions, which corresponds to $\sim$ 630 non-QE interactions per year. A 3D view of a QE event can be seen in Fig. 46.

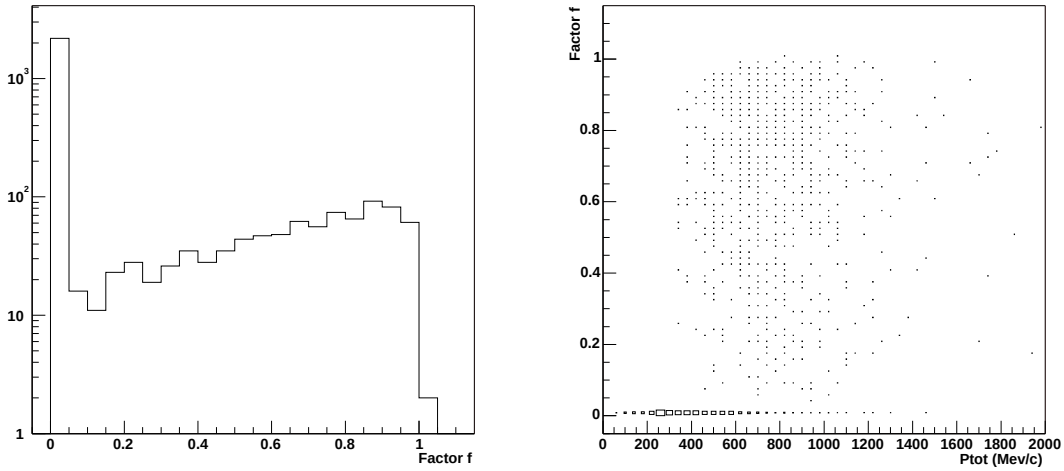


Figure 45: (left) factor f for protons in QE interactions; (right) the same factor is plotted against the total momentum of the proton, obtained form Monte Carlo at the generator level.

10.3 Muon Ranger Simulation Results

To study the performance of the MRD, charged-current neutrino events were simulated in the fiducial volume of the WC using the calculated T2K neutrino energy spectrum at a distance of 2 km from the

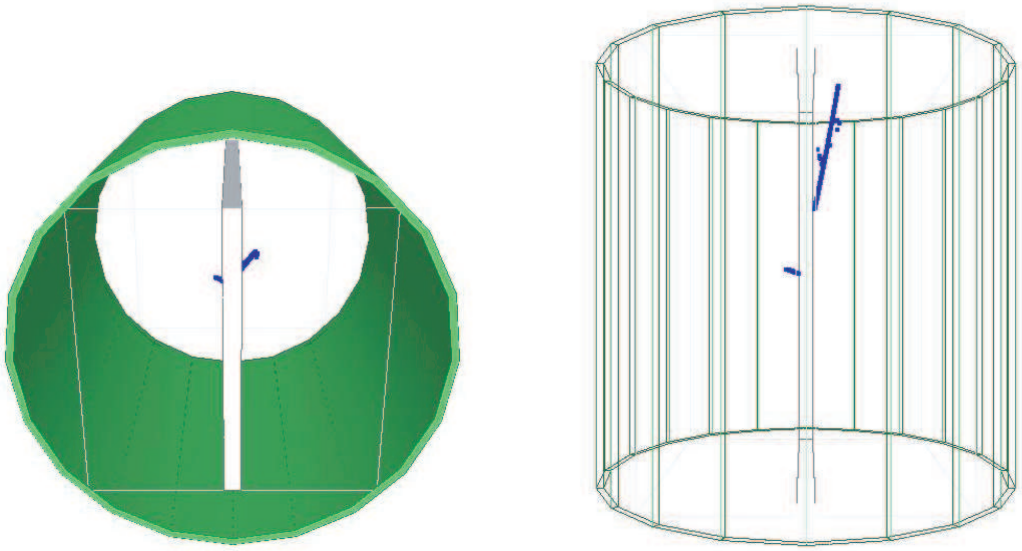


Figure 46: 3D view of a inner target QE event.

neutrino source. The spectrum of muons that penetrate into the MRD through the vertical wall of the Cherenkov detector (Fig. 47) have been used for the simulation of the MRD response.

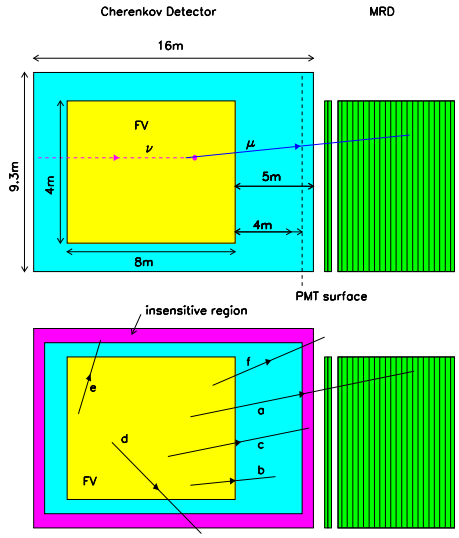


Figure 47: Sketch of the layout of water Cherenkov detector and muon ranger (top panel). Event types produced by neutrino in fiducial volume (bottom panel).

10.3.1 MRD Simulation

A 3D MC simulation of muon transport through the WC and MRD was developed. The code allows us to either consider the average ionization energy loss calculation along a tracking step, or to account for fluctuations either by explicit δ-ray production above a given energy out (in this simulation a δ-electrons energy cut of 1 MeV is used) or by a computed fluctuation function (Gaussian or an approximate Landau shape). Muon transport is performed with variable optimized steps. The program also performs a discrete sampling of bremsstrahlung, inelastic muon-nuclear interaction and pair production processes.

A special feature of this program is the 3D simulation of the muon tracks. A recent treatment of multiple Coulomb scattering of muons is used [32]. In this approach the muon angular distribution is similar to the Molière distribution after passing through a short thickness of material and moderate deflection angles. However, for thicker materials, the angular distribution is drastically changed by the influence of the nuclear form factor. Multiple scattering and lateral displacement are treated as continuous processes along the muon track.

10.3.2 MRD Track and Energy Reconstruction

The algorithm for the muon track and energy reconstruction is based on the least square method and described in [33, 34, 35]. It takes into account contributions from the position measurement error, energy loss and Coulomb scattering.

A scatter plot of the true muon energy at the point of entry into the MRD E_0 versus reconstructed energy E_{rec} is presented in Fig. 48. The discrete structure of the MRD can be seen in the relationship between E_0 and E_{rec}. The MRD can measure muon energies over the range 0.125 to 3.5 GeV.

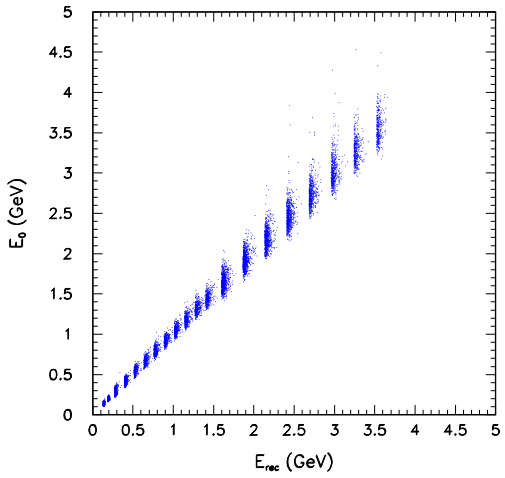


Figure 48: Muon energy E_0 at the entry into the MRD versus reconstructed energy E_{rec}.

Figure 49 (top panel) shows the dependence of the mean value of the energy resolution $\langle \Delta E/E \rangle$ on the muon energy, where $\Delta E = E_0 - E_{rec}$. The difference between the true muon direction and the reconstructed muon direction $\Delta\theta$ (angular resolution) is plotted in Fig. 49 (bottom panel). The vertical bars show $\sigma(\Delta E/E)$ and $\sigma(\Delta\theta)$ respectively. The energy resolution is $\sim$ 1% and $\sigma(\Delta E/E)$=5 to 7% at $E \leq$3.5GeV; $\Delta\theta$ decreases with muon energy from $\sim$6° down to 1°.

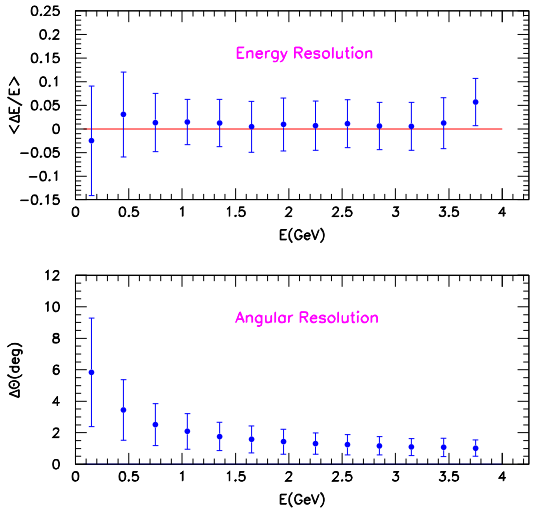


Figure 49: Energy (top panel) and angular (bottom panel) resolution of the MRD versus muon energy. The vertical bars show $\sigma(\Delta E/E)$ and $\sigma(\Delta\theta)$.

10.3.3 Combined WC/MRD Acceptance and Resolution

To estimate the efficiency of operating the WC and MRD in coincidence we considered the case when the water Cherenkov detector (size, layout and PMTs as in the case of the 1kt tank at K2K) is complemented by the MRD at a distance of 74 cm. A schematic view of the WC/MRD is shown in Fig. 47 (top panel).

A number of different muon event types are shown in Fig. 47 (bottom panel). They are summarized as:

(a) Stopping muons in the active MRD region

(b) Stopping muons in the sensitive WC region

(c) Stopping muons between the active water region and the active MRD region

(d) Penetrating muons through the barrel wall

(e) Stopping muons in the barrel side insensitive region

(f) Penetrating muons through the vertical wall of the WC.

The detection efficiencies of the different events as a function of the muon energy are shown in Fig. 50. For events of types (a) and (b) the minimum is $\sim$ 52% in the energy bin 1.8 to 2.1 GeV. Events of type (c) may be detected using the scintillator plane between the active water region of the WC and the active region of the MRD. Events of type (e) in principle may also be detected by a barrel-side outer detector; however the energy resolution will be worse in comparison with (a) and (b) type events. The efficiencies for events of the (a)+(b)+(c) and (a)+(b)+(c)+(e) type are also shown in Fig. 50. In the last case the minimal efficiency is equal of 75% in the energy bin 2.4 to 2.7 GeV.

The energy reconstruction method for muon events of type (a) is described in reference[35].

The multi-detector reconstruction performance is presented in Figs. 51 and 52. The scatter plot of (E_{rec}, E_0), is shown in Fig. 51, where E_{rec} is the reconstructed and E_0 is the actual muon energy. The energy $\langle\Delta E/E\rangle$ and angular $\Delta\theta$ resolutions of the WC and MRD are given in Fig. 52 as functions of the

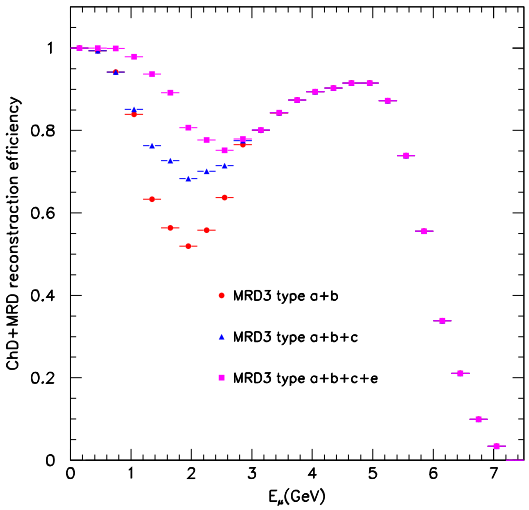


Figure 50: WC/MRD reconstruction efficiency as a function of muon energy.

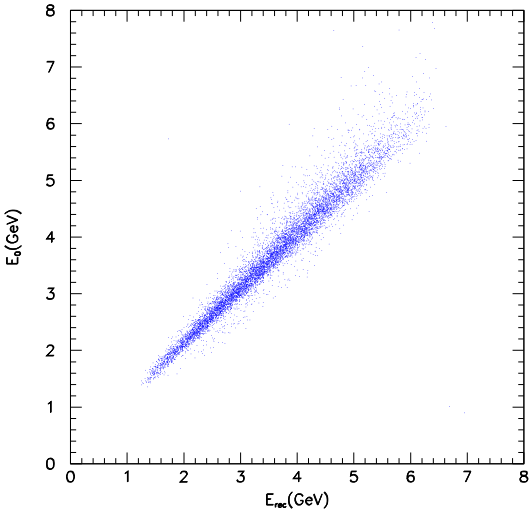


Figure 51: Muon energy at production, E_0, as a function of reconstructed energy E_{rec}.

muon energy, where the vertical bars show the $\sigma(\Delta E/E)$ and $\sigma(\Delta\theta)$. The energy resolution $\sigma(\Delta E/E)$ equals to $5-6\%$ and does not depend on muon energy in the region 1.2-6 GeV. The angular resolution $\Delta\theta$ decreases with energy from $\sim 3^\circ$ up to $\sim 0.7^\circ$.

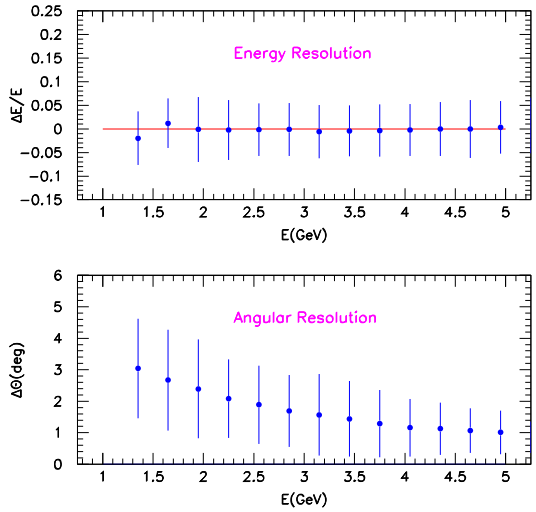


Figure 52: Energy (upper) and angular (lower) resolutions of the WC/MRD system versus muon energy. The vertical bars show the $\sigma(\Delta E/E)$ and $\sigma(\Delta\theta)$.

11 Physics with the Intermediate Detector

This section describes the role of the 2KM detectors in characterizing the flux and interactions of neutrinos at the Super-Kamiokande far detector. The primary concerns are prediction of the background for the ν_e appearance search and prediction of the ν_μ flux for the disappearance measurement. The goal of the 2KM detector is to control systematic uncertainties and provide a direct comparison of the unoscillated event rate, independent of Monte Carlo prediction.

11.1 Measurement of the Background for ν_e Appearance

When searching for ν_e appearance in Super-K there will be both an irreducible intrinsic ν_e background and a background due to event misidentification. Figure 53 shows an example of the optimistic case where a large ν_e appearance signal is found just below the current best experimental limit.

In this case the background is a relatively small fraction of the signal. However, if there is no observed signal, or the signal is quite small, the error or sensitivity will be dominated by how well we can determine the background to the search. Figure 54 shows this effect as a function of exposure for Super-K with several errors on the total background normalization assumed.

As can be seen, if the total background uncertainty is allowed to approach 20% the θ_{13} sensitivity flattens out after 5 years of T2K running as the result becomes systematics-limited. Therefore our goal is to control the total uncertainty to 10% and individual uncertainties to 5%. The leading uncertainty is in the rate of NC single-π^0 interactions on water which fake a single-ring electron. The 2KM water Cherenkov detector will provide a direct measurement of these interactions using a detector with nearly identical response. Approximately 700 NC-π^0 will be misidentified as ν_e background in the 2KM, contributing to a prediction of the background rate at Super-Kamiokande. Another 20000 NC-π0 will be successfully reconstructed, allowing us to explore the way in which these events become misidentified as well as to develop improved reconstruction algorithms that can be applied in the far detector.

Also shown in Fig. 54 is the situation for the proposed second phase of T2K with an upgraded neutrino beam and approximately 20 times the fiducial volume (known as Hyper-Kamiokande). In this case the

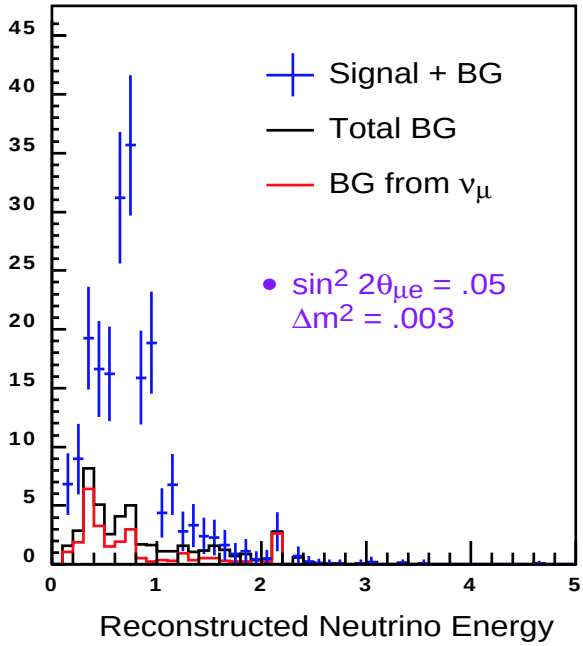


Figure 53: Expected ν_e signal in Super-K at the current best experimental limit with a nominal background.

result is completely systematics-limited and the total uncertainty needs to approach the 1% level.

11.1.1 Neutral Current π^0 Backgrounds

Neutral current π^0 events are a major source of background for ν_e-appearance at SK. In a water Cherenkov detector, a π^0 should produce two e-like rings events corresponding to the electromagnetic showers from $\pi^0 \rightarrow \gamma\gamma$. If the Cherenkov ring from one EM shower is missed, the event would be misconstrued as single-ring e-like and then may fall in the acceptance window for ν_e appearance. We can predict the rate of these events by applying the same selection criteria used at SK to the 2KM data.

Certain selection criteria have been implemented to directly address the π^0 background. First, we expect that some π^0 production comes from coherent neutrino scattering off of the oxygen nucleus. In this case there is very little momentum transfer and the π^0 is produced following the neutrino direction. For the case where the π^0 decays asymmetrically and only the high energy photon in the forward direction is identified, the single e-like ring will also closely follow the neutrino direction. To reduce this background we restrict the angle between the e-like ring and the neutrino direction to have $\cos\theta < 0.9$. Figure 55 shows the angle between the π^0 direction and the neutrino beam direction for events in which the π^0 was successfully reconstructed with two e-like rings. The contribution from coherent π^0 production is overlaid as a hatched region, showing the sharper forward scattering peak. The statistics plotted correspond to the 5-year T2K run, and are clearly suitable for studying this process by an analysis of the shape of this distribution (or others such as q^2).

In order to remove the remaining NC events, a special π^0 fitter is used, based on a maximum likelihood method to test the π^0 hypothesis against the e^- hypothesis. The idea is that some π^0 decays are not found by the standard ring counting algorithm because the low energy second γ cannot be easily distinguished from scattered/reflected light. The PMT light pattern is fit twice, first assuming that the light pattern comes from a single electron track, then assuming that the light pattern was produced by two showering tracks. This program returns the likelihood ratio for these hypotheses as well as the $\gamma\gamma$ invariant mass from the 2-track fit. The NC-π^0 background peaks at the π^0 mass, while the ν_e signal does not; events

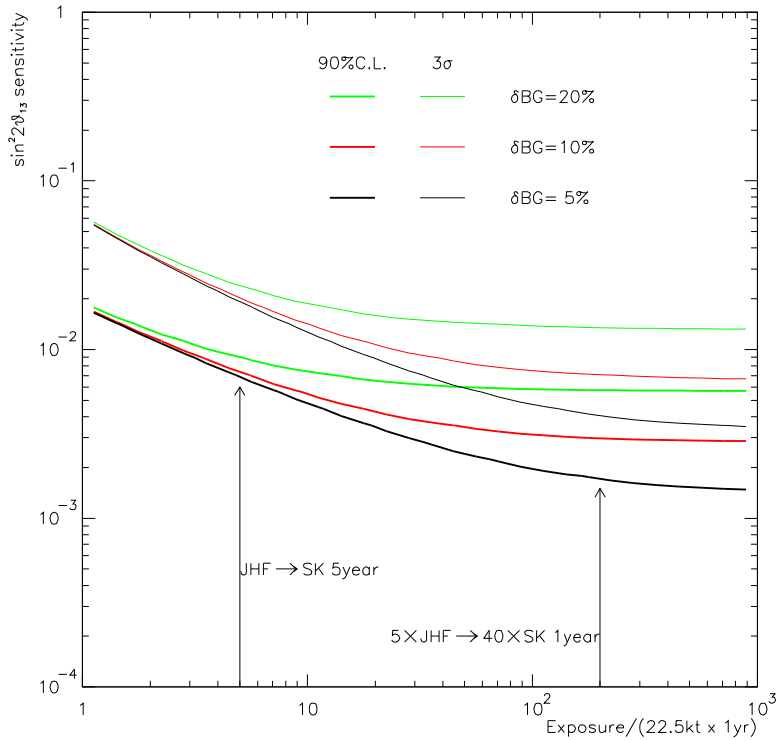


Figure 54: Sensitivity to θ_{13} as a function of exposure for three uncertainties in the background prediction. The first arrow is the exposure for a five year T2K run, the second for five years of a upgraded J-PARC beam with Hyper-Kamiokande as the target.

with a computed invariant mass larger than 95 MeV/c^2 are rejected. The likelihood ratio is also used for e/π^0 separation: events with high L_{π^0}/L_e are more likely to be π^0.

Figure 56 shows the three special variables used to reduce NC-π^0 background. In each panel the distribution of the parameter is plotted, with the upper row for the case of ν_μ interactions (mostly NC), and the lower row is for the case of ν_e. All analysis cuts other than the one plotted have been applied, including the 1-ring e-like requirements and the neutrino energy window. One can see that the responses of the 2KM detector and SK far detector are very similar and the effectiveness of these cuts can readily be studied.

11.1.2 Intrinsic Beam Electron Neutrinos

The second major contribution to ν_e appearance background is ν_e interactions from the intrinsic ν_e flux component of the T2K beam. These neutrinos originate from three main sources: muon decay, $Ke3$ decay of K^+ and $Ke3$ decay of K^0_L. Within the ν_e appearance window of $350 < E_\nu < 850$ MeV, the dominant contribution (89%) is muon decay. The intrinsic ν_e background will be an irreducible component of the total background measurement by the 2KM detector. Figure 58 shows the shape of each contribution as a function of neutrino energy as measured by a 5-year exposure of the 2KM detector. Although the ν_e background is irreducible, it is possible to study and limit this contribution by considering the superposition of the predicted shape of each background source.

The smaller contribution (11%) from $Ke3$ decay to intrinsic ν_e background may be indirectly studied by measuring the rate of high energy muons at 2KM. High energy muons typically exit the WC and range out in the MRD. For muons with energy greater than 2.5 GeV, as shown in Fig. 57, the parent neutrino

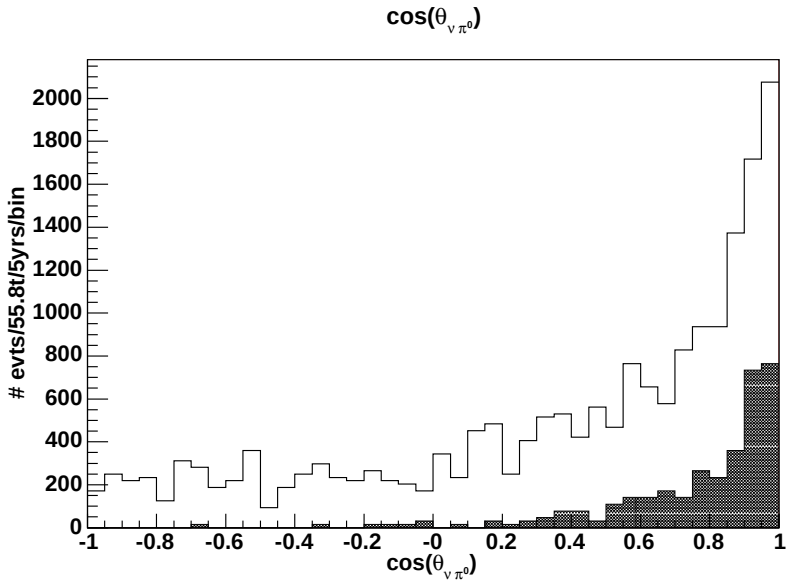


Figure 55: The distribution of $\cos\theta_{\nu\pi^0}$ for successfully reconstructed π^0 events in a 5-year run of the the 2KM water Cherenkov detector. The upper histogram is for all events, and the lower histogram is the predicted contribution from coherent π^0 production.

is predominantly from kaon decay, based on our Monte Carlo estimate. In a 5-year exposure at 2KM we will measure 85000 such interactions. Assuming we understand the acceptance of our detector, this can be extrapolated into an 0.5% estimate of the contribution of K^+ in the beam flux.

11.1.3 Misidentified Charged Current Background

The final background component – misidentification of CC-ν_μ interactions – is smallest. Although these interactions should look very different than ν_e interactions, there is a very high rate of CC-ν_μ interactions. Single-ring μ-like events are distinguished from single-ring e-like events by a particle identification algorithm as shown earlier in Fig. 31. We estimate that this algorithm is better than 98% efficient in rejecting muons from being classified as e-like.

When searching for ν_e appearance using the 2KM water Cherenkov detector and Super-K a series of event selection cuts, that aim at selecting CC QE ν_e induced events, is applied: we select fully contained 1 ring e-like events, with a visible energy over 100 MeV, and no decay electron. We also select events with a reconstructed ν_e energy between 0.35 GeV and 0.85 GeV. After all cuts (including the π^0cuts defined below) the remaining CC ν_μ contamination is estimated to be 0.05% in the 2KM water Cherenkov detector. At SK the corresponding contamination is 0.03% (neutrino oscillations naturally reduce this background). The good e^-/μ^-separation performance of the water Cherenkov detectors is necessary to reduce this source of background.

11.1.4 Prediction of the Background for ν_e Appearance at Super-K using the 2km detector.

Using the water Cherenkov detector we will measure the total background for the ν_e appearance search. We apply the same set of cuts to 2KM data as will be applied to the SK far detector data. Table 5 lists the event rates after each cut is applied, broken down by the three categories of background: NC-π^0, beam ν_e, and CC-ν_μ misidentification. The statistics quoted are for a 5-year exposure of the T2K beam assuming 10^{21} protons-on-target per year. We expect in total approximately 2000 events at SK (see also Fig. 58).

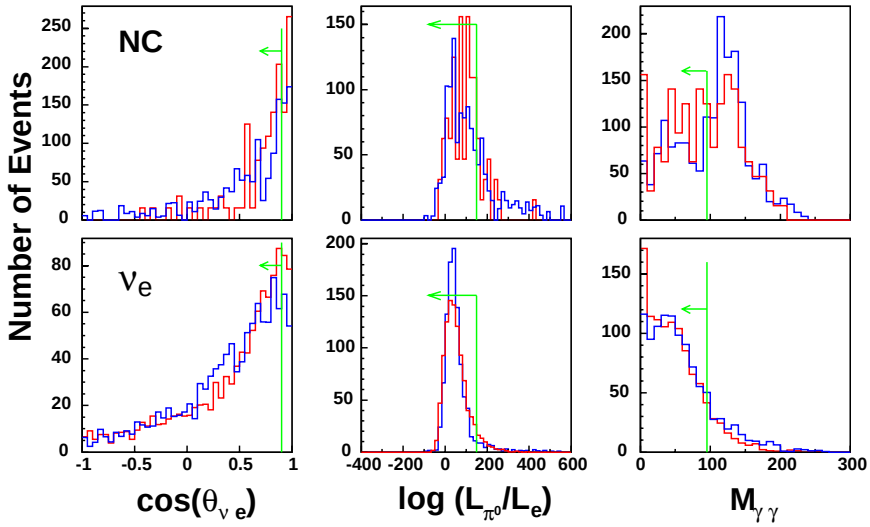


Figure 56: Distributions of the NC-π^0discriminating variables. The first column is the opening angle between the single e-like ring and the neutrino direction; the second column is the likelihood ratio from the π^0-fitter; the third column is the reconstructed invariant mass. The top row is for beam ν_μ, and is therefore mostly NC after applying the analysis cuts. The bottom row is for beam ν_e and is therefore mostly charged current ν_e. The distributions from SK (blue) and from the 2KM water Cherenkov detector (red) are overlaid.

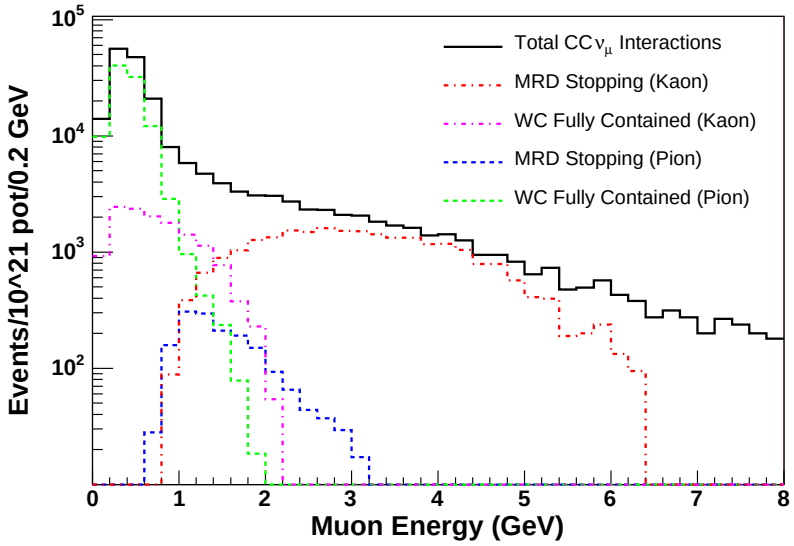


Figure 57: The spectrum of reconstructed muon energy at 2KM. The event sample requires either containment in the WC or for the muon to stop in the MRD. The parent neutrino component from π^+ and K^+ decay is separately identified. Above 2.5 GeV, the parent neutrino is predominantly from K^+ decay; almost all of these events exit the WC and stop in the MRD.

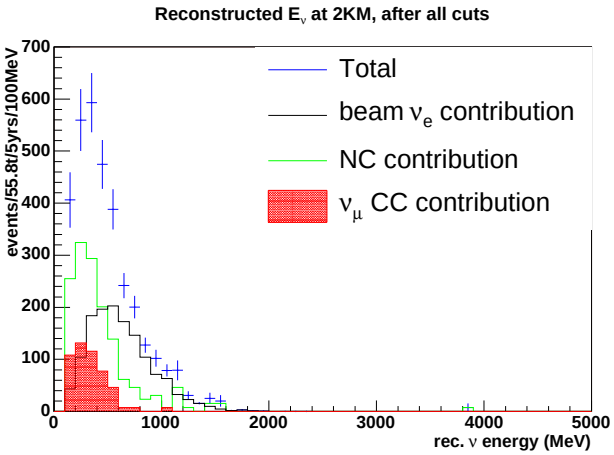


Figure 58: Measured ν_e background at 2KM (water Cherenkov), with contributions from the three different background sources. The beam ν_e background becomes dominant above approximately 600 MeV.

	NC	beam ν_e	CC-ν_μ
1) FCFV, E_{vis} >100 MeV	53847	10997	325969
2) 1-ring e-like	10843	5454	10604
3) no decay-e	10187	4575	2009
4) 0.35 GeV < $E_{\nu e}^{rec}$ <0.85 GeV	3476	1409	649
5) e/π^0separation	641	879	216

Table 5: Number of events in the 2KM water Cherenkov detector (5 yr exposure, 55.8t fiducial volume) after the standard cuts applied in the ν_e appearance analysis.

The background for ν_e analysis at Super-Kamiokande, may be extrapolated from the measurement at 2KM using a simple scaling method:

$$N_{SK} = N_{2km} \times \left(\frac{L_{SK}}{L_{2km}}\right)^2 \times \frac{M_{SK}}{M_{2km}} \times \frac{\epsilon_{SK}}{\epsilon_{2km}}, \tag{11}$$

where L is the distance from the detector the neutrino source and M the fiducial mass used in the analysis. For CC-ν_μ it is necessary to include the oscillation "survival" probability in the estimate (thereby reducing the background from misidentified ν_μ CC events). For this study we chose $\Delta m^2_{23} = 2.5\,10^{-3}\text{eV}^2$ and $\sin^2 2\theta_{23} = 1.0$ to describe the oscillation.

It is possible to obtain a preliminary, simple, and conservative estimate of the systematic errors on this measurement. In the following study, the ratio of efficiencies $\frac{\epsilon_{SK}}{\epsilon_{2km}}$ in equation 11 is assumed to be equal to 1. For each analysis cut the efficiency difference between SK and 2km $\epsilon_{2km} - \epsilon_{SK}$ is taken as the systematic error. The systematic error for all cuts is found by adding all the errors in quadrature[7]. We then take into account systematics on the fiducial volume and the energy scale, which we conservatively set to 4% and 3% respectively (based on K2K 1kton experience [36]). The systematic error on the volume is the same for all three background categories; therefore it is added in quadrature in the total systematic estimate to avoid overcounting. In table 6 the efficiency differences between SK and 2KM are listed. Applying this method,

[7]In the full analysis the efficiency differences would be corrected for and the systematic uncertainty on the differences would be separately estimated.

	NC	beam ν_e	CC-ν_μ
1)1 ring	6.3%	4.6%	-2.7%
2)e-like	-2.3%	2.1%	1.2%
3)no decay e-	-1.5%	2.5%	0.05%
4)$\cos\theta < 0.9$	-2.3%	1.5%	0.03%
5)$M_{\gamma\gamma} < 95$ MeV	-0.3%	0.4%	0.06%
6)$\Delta \log L < 150$	1.5%	1.7%	0.04%

Table 6: $\epsilon_{2km} - \epsilon_{SK}$ for each cut. As a starting point we use fully-contained events in the fiducial volume, with 100 MeV $< E_{vis} <$ 1000 MeV.

we obtain a predicted background of 23.4 events with a statistical uncertainty of 0.6 events and a systematic uncertainty of 1.6 events. The total error is approximately 7.5%, within our 10% goal. The extrapolated background is plotted in Figs. 59 and 60, where it is compared with the fully simulated and reconstructed background at Super-Kamiokande. There is good agreement between the two shapes inside the signal window, demonstrating that this simple scaling method is well-suited to predict the background at SK. The above analysis was performed assuming 5-year exposure of the T2K beam with 10^{21} protons-on-target per year. After one year of exposure the total error using the same technique would be approximately 8.7%, still within our 10% goal.

	NC	beam ν_e	CC-ν_μ
1) Monte Carlo estimate	8.4	14.1	0.4
2) Extrapolated from 2KM	9.6 ± 0.4 ± 0.8	13.2 ± 0.5 ± 1.0	0.6 ± 0.04 ± 0.03

Table 7: The number of background events for the ν_e appearance search at Super-Kamiokande, based on 5 years of running at $10^2$1 pot/yr. The first row was obtained with the T2K beam simulation, Super-Kamiokande neutrino interaction Monte Carlo, detector simulation, and reconstruction. The second row was deduced from Table 5 by the geometrical scaling method, assuming the ratio of efficiencies is equal to 1. The uncertainties listed first are statistical, derived from the event rate at 2KM. The second uncertainties are systematic, estimated as described above. The systematic uncertainty of the fiducial volume are not included in these numbers.

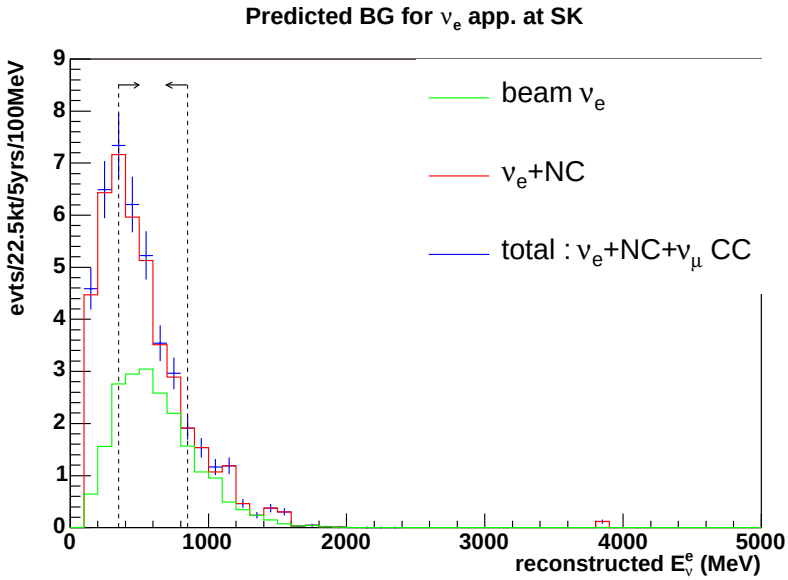


Figure 59: Extrapolated background for ν_e appearance at SK, using the scaling procedure described in the text. The reconstructed energy window is indicated by the dashed lines.

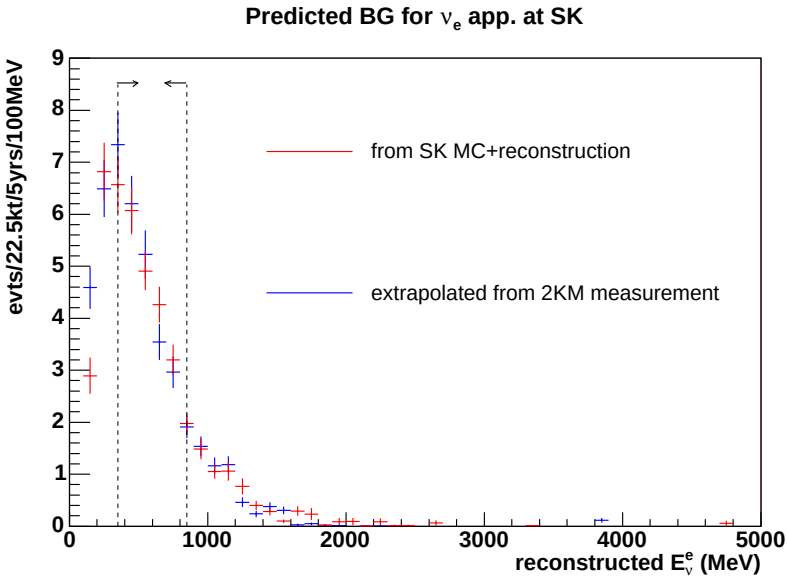


Figure 60: Total background for ν_e appearance at SK. The red points correspond to the results of the full T2K simulation and reconstruction at Super-Kamiokande. The results from the 2KM extrapolation are shown in blue. The shapes are consistent within the signal window.

11.2 Measurement of the ν_μ Neutrino Spectrum

By measuring ν_μ CC interactions at 2KM, we have a reference for measuring the distortion at Super-K due to neutrino oscillations. This allows us to measure the parameters Δm^2_{23} and θ_{23}. Figure 61 shows the percentage difference of the fluxes at 2KM and Super-K as a function of neutrino energy, using the T2K beam Monte Carlo. As expected, this ratio is reasonably flat with a spread of less than $\pm 5\%$ over all energies. Further quantitative studies of the effect on the disappearance experiment and the measurement of the mixing parameters is underway.

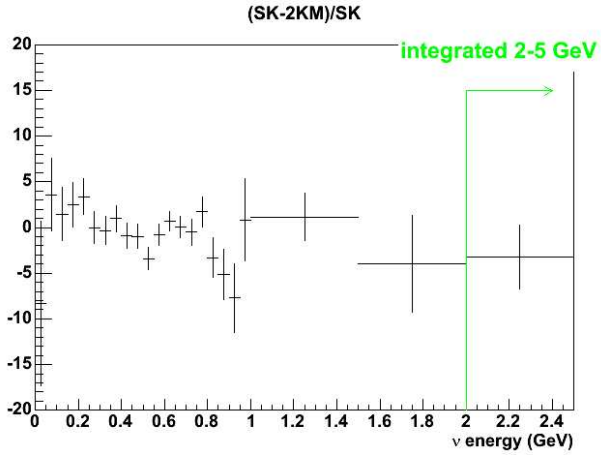


Figure 61: $\frac{F_{SK} - \left(\frac{L_{SK}}{L_{2km}}\right)^2 \times F_{2KM}}{F_{SK}}$ (in %) as a function of true ν_μ energy (where is F is the ν_μ flux).

In order to reconstruct the energy of the incoming neutrinos from the outgoing interaction products we must assume that we know the type of neutrino interaction that took place in the event, so we can describe the kinematics. To do this, cuts are performed on the data to obtain a sample with as high a QE purity as possible. If the event comes from a QE interaction then its kinematics can be easily described and the energy of the neutrino can be reconstructed using only the outgoing lepton.

There is always some background in a QE-selected sample arising from other types of neutrino interactions. These events, when reconstructed with QE kinematics, will give an incorrect neutrino energy. For this reason, we need to carefully characterize the number of non-QE interactions in our beam. Since the expected event rate is approximately 120,000 QE ν_μ CC interactions per 100 tons per 10^{21} protons-on-target and 70000 non-QE ν_μ CC interactions per 100 tons per 10^{21} protons-on-target, the event rate in both the water Cherenkov and liquid argon detectors will be high enough to make careful studies of these backgrounds.

The two detector elements complement each other. Since the 2KM detector is made of water, it has the same target material as Super-K and any nuclear target effects should be the same between the two detectors. The liquid argon detector will have a comparable event rate on argon, and due to its exceptionally fine granularity, will make exclusive measurements of the non-QE reactions.

Since the target nucleus in the LAr is different than that of Super-K, we are investigating the option of embedding a frozen water target between the cathode planes of the LAr detector, as was described in more detail in sections 8.2.2 and 10.2.8. By observing tracks which are initiated in the water target but are reconstructed in the liquid argon, we can compare the differences in our beam between water and argon targets and make any corrections necessary, even without input from external measurements. Even a small frozen water target will have a sizeable number of reconstructed interactions, as shown in Tab. 8.

	Size 1	Size 2	Size 3
mass of target (ton)	2.69	5.37	10.74
width of target (cm)	12.5	25	50
total number of QE interaction	3278	6556	13112
QE protons	50%	30%	19%
QE full reconstruction	36%	22%	14%
number of QE full reconstructions	1178	1440	1832
total number of non-QE interactions	1853	3706	7412
non-QE protons	32%	22%	16%
non-QE π^+	94%	85%	71%
non-QE π^0	95%	85%	76%
non-QE full reconstructions	27%	17%	9%
non-QE full reconstructions	500	630	670

Table 8: The number of neutrino interactions in the water target of the LAr detector for three possible water target sizes. Reported event rates are per 10^{21} pot.

11.3 Physics in the 2nd Phase T2K Experiment with the 2KM Detector

As was just shown, measuring the total total background to the ν_e search is important at about the 10% level for T2K and perhaps at the 1% level for a possible next generation experiment. For this reason, building a detector approximately 2 km away from the neutrino production point is highly desirable for the T2K experiment and most likely essential for a next generation experiment.

A site has already been chosen where a suitable detector can be built, and the land rights for this site negotiated with local government officials. The land will be given for the use of T2K with no purchasing cost. The T2K beam is aimed two degrees below both Super-K and the future proposed site for the Hyper-K experiment. This is illustrated in Fig. 62.

The proposed site for the 2 km detector complex is in line with the portion of the beam that would be seen by the Hyper-K experiment. We will rely on the beam's azimuthal symmetry (as measured 280 meters away from the production point) to predict the flux and the Super-K position. The choice of this position is partly driven by cost, since hills in the line of site of SK would increase the depth of drilling of the experimental hall.

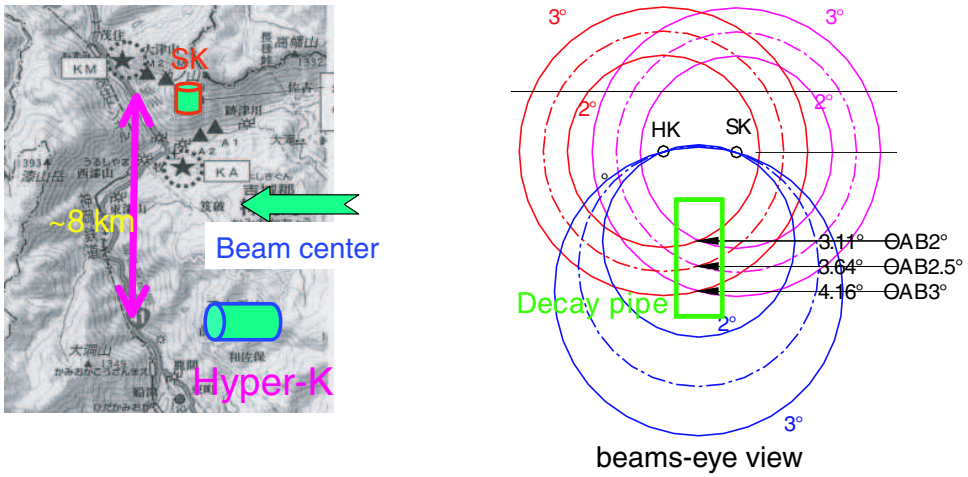


Figure 62: The position of the T2K neutrino beam relative to both Super-K and Hyper-K. The beam angle can be tuned by moving the beam up and down vertically. In this configuration both detectors are off-axis to the beam.

References

[1] Super-Kamiokande, Y. Fukuda *et al.*, Evidence for oscillation of atmospheric neutrinos, Phys. Rev. Lett. **81**, 1562 (1998), hep-ex/9807003.

[2] Super-Kamiokande, S. Fukuda *et al.*, Determination of solar neutrino oscillation parameters using 1496 days of super-kamiokande-i data, Phys. Lett. **B539**, 179 (2002), hep-ex/0205075.

[3] SNO, Q. R. Ahmad *et al.*, Direct evidence for neutrino flavor transformation from neutral-current interactions in the sudbury neutrino observatory, Phys. Rev. Lett. **89**, 011301 (2002), nucl-ex/0204008.

[4] KamLAND Collaboration, Measurement of neutrino oscillation with KamLAND: Evidence of spectral distortion, (2004), hep-ex/0406035.

[5] K2K, E. Aliu *et al.*, Evidence for muon neutrino oscillation in an accelerator- based experiment, Phys. Rev. Lett. **94**, 081802 (2005), hep-ex/0411038.

[6] LSND, C. Athanassopoulos *et al.*, Evidence for $\bar{\nu}_\mu \to \bar{\nu}_e$ oscillation from the LSND experiment at the Los Alamos Meson Physics Facility, Phys. Rev. Lett. **77**, 3082 (1996), nucl-ex/9605003.

[7] MiniBooNE, J. Monroe, Latest results from the MiniBooNE experiment and updated $\nu_\mu \to \nu_e$ sensitivity, (2004), hep-ex/0406048.

[8] J. Burguet-Castell, M. B. Gavela, J. J. Gomez-Cadenas, P. Hernandez, and O. Mena, On the measurement of leptonic CP violation, Nucl. Phys. **B608**, 301 (2001), hep-ph/0103258.

[9] D. Perkins, *Introduction to Particle Physics* (Addison Wessley, Menlo Park, California, 1987).

[10] S. F. King, Neutrino mass models, Rept. Prog. Phys. **67**, 107 (2004), hep-ph/0310204.

[11] M. Gell-Mann, P. Ramond, and R. Slansky, Complex spinors and unified theories, Print-80-0576 (CERN).

[12] T. Yanagida, Horizontal gauge symmetry and masses of neutrinos, In Proceedings of the Workshop on the Baryon Number of the Universe and Unified Theories, Tsukuba, Japan, 13-14 Feb 1979.

[13] M. Fukugita and T. Yanagida, Baryogenesis without grand unification, Phys. Lett. **B174**, 45 (1986).

[14] K2K, M. H. Ahn *et al.*, Indications of neutrino oscillation in a 250-km long- baseline experiment, Phys. Rev. Lett. **90**, 041801 (2003), hep-ex/0212007.

[15] NOvA, I. Ambats *et al.*, NOvA: Proposal to Build an Off-Axis Detector to Study muon- netrino $\to$ electron-neutrino Oscillations in the NuMI Beamline, (2004), FERMILAB-PROPOSAL-0929.

[16] P. Huber, M. Lindner, and W. Winter, Synergies between the first-generation JHF-SK and NuMI superbeam experiments, Nucl. Phys. **B654**, 3 (2003), hep-ph/0211300.

[17] Long Baseline Neutrino Oscillation Experiment BNL E889 proposal, (1995).

[18] M. Apollonio *et al.*, Search for neutrino oscillations on a long base-line at the CHOOZ nuclear power station, Eur. Phys. J. **C27**, 331 (2003), hep-ex/0301017.

[19] Y. Itow *et al.*, The JHF-Kamioka neutrino project, (2001), hep-ex/0106019.

[20] Y. Fukuda *et al.*, The Super-Kamiokande detector, Nucl. Instrum. Meth. **A501**, 418 (2003).

[21] H. G. Berns and R. J. Wilkes, GPS time synchronization system for K2K, IEEE Trans. Nucl. Sci. **47**, 340 (2000).

[22] M. Antonello *et al.*, Detection of Cherenkov light emission in liquid argon, Nucl. Instrum. Meth. **A516**, 348 (2004).

[23] S. Amerio *et al.*, Design, construction and tests of the ICARUS T600 detector, Nucl. Instrum. Meth. **A527**, 329 (2004).

[24] A. Badertscher, M. Laffranchi, and A. Rubbia, Development of a novel high-sensitivity LAr purity monitor based on an alpha-source, (2004), physics/0412166.

[25] W. F. Schmidt, Trans. Electrical Insulation **E1-19**, 389 (1984).

[26] M. Laffranchi, Diploma thesis (ETH) (2000), http://neutrino.ethz.ch/diplomathesis.html.

[27] A. Badertscher, M. Laffranchi, A. Meregaglia, and A. Rubbia, First operation of a liquid argon TPC embedded in a magnetic field, New J. Phys. **7**, 63 (2005), physics/0412080.

[28] Super-Kamiokande, Y. Ashie *et al.*, A measurement of atmospheric neutrino oscillation parameters by Super-Kamiokande I, (2005), hep-ex/0501064.

[29] J. R. Bueno A. and A. Rubbia, Spatial and Calorimetric Reconstruction of the ICARUS T600 Data, ICARUS-TM Report No. 02-03, 2002 (unpublished).

[30] R. E. Kalman, Trans. AMSE, J. Bas. Eng. **82D** (1960).

[31] R. Fruhwirth, Nucl. Instrum. Meth. **A262**, 444 (1987).

[32] A. V. Butkevich, R. P. Kokoulin, G. V. Matushko, and S. P. Mikheyev, Comments on multiple scattering of high-energy muons in thick layers, Nucl. Instrum. Meth. **A488**, 282 (2002), hep-ph/0108016.

[33] A. P. Thomas J. and D. Tovee, The Principle of Muon Tracking in MINOS, NuMi Report No. L-301, http://www-numi.fnal.gov/cgi-bin/notePublicPrint.

[34] Review of track fitting methods in counter experiments, CERN Report No. 81-06, 1981 (unpublished).

[35] A. V. Butkevich, MC study of 2km muon range detector for JHF neutrino experiment, http://neutrino.kek.jp/jhfnu/internal/2km/report/butkevich-mrd.ps.

[36] M. H. Ahn *et al.*, Search for electron neutrino appearance in a 250-km long-baseline experiment, Phys. Rev. Lett. **93**, 051801 (2004), hep-ex/0402017.

A Schedule

The schedule of the construction of the 2 km facility and the detectors has been estimated in detail. The underground facility must be excavated first, which will take about 12 months. At this stage, there will be no surface buildings.

After the excavation of the underground hall, large equipment can be lowered through the 8.5 meter diameter vertical shaft. After that, when the surface building is constructed, installation of large equipment whose size is close to 8 meters will no longer be possible. Furthermore, since the bottom of the underground hall has a dead end, the order of the installation of the large equipment will be determined by the order of the detectors. According to the baseline detector configuration design, the installation must be done in the following order: MRD, water Cherenkov, then liquid argon TPC. Since the facility will not have any permanent elevators at this stage, the installation time must be minimized in order to minimize the access to the underground.

The MRD will be installed first. The support structure of the MRD will be constructed first, and then the MRD will be installed. Because of the structure of the MRD, the scintillator plates must be installed at the same time as the steel plates. Each steel plate will weigh less than 40 tons, so they can be lowered by a 100 ton truck crane. It will take about 3 months to complete the MRD part, including the support structure.

The construction of the water Cherenkov detector will follow the MRD installation. The enclosure will be constructed underground. It is expected that the construction will take about 5 months. At this stage, however, we will not install the PMTs and the electronics; these will be installed later.

The liquid argon detector will be assembled at a separate location on the surface[8], moved to the 2 km site and lowered to the underground. The weight of the pre-assembled liquid argon detector will be about 100 tons. Therefore, a 300 ton truck crane will be used to lower the detector. It is expected that it will take about 7 months (including 2 months of contingency) to install the pre-assembled liquid argon detector. Some preparation work for the liquid argon detector installation can be done while the water detector construction work is in progress. Also, some part of the surface facility construction can start after lowering the liquid argon detector to the underground hall.

After the installation of these detectors, the surface facilities and the elevators that connect to them will be constructed. It is estimated that this construction will take about 9 months.

All the remaining installation work, such as the installation of the PMTs (for water Cherenkov detector), the front end electronics (for liquid argon detector, water Cherenkov detector and MRD), and the gas and water piping will then be done. We expect it will take about 4 months to complete this installation.

At the same time, the water system, the argon handling facility and the online data acquisition system will be constructed and installed at the surface facility. The work will also take about 4 months.

Finally, the 300 ton detector will be filled with liquid argon, and 1000 tons of pure water will be produced to fill the underground water detector. After filling, the purification of the water and liquid argon will be gradually improved by the water and liquid argon purification systems, respectively. It is expected that both the liquid argon and water will be sufficiently purified after 2 months.

During most of the construction period, it is essential that the proper pre-assembling space is available outside of the 2 km facility, preferably somewhere in the J-PARC facility. See Fig. 63 which shows the construction schedule at the 2 km site and at the other site.

In total, it will take 3 years to complete the detector construction. Adding 2 months for the water and liquid argon filling, there will be 38 months from the start of the excavation to first data-taking. Figure 63 summarizes the expected schedule of the 2 km facility and detector complex construction, assuming that the construction will start on the first month of Year 1.

[8] We will need an assembly hall at the J-PARC site.

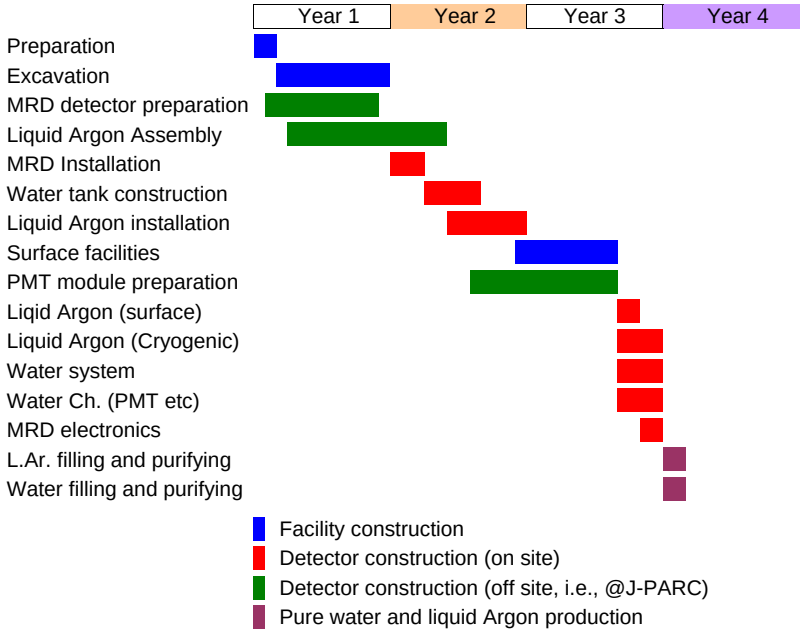


Figure 63: Expected schedule of the 2 km facility and detector complex construction. It is assumed that the construction will start on the first month of Year 1.

B Budget

The costs of the 2KM complex including the costs for civil construction, support facilities, as well as the three main detector sub-systems have been estimated. They are outlined below. In the following tables all costs have been converted into U.S. dollars. The exchange rates used were 107 Japanese Yen/dollar and 1.26 Dollars/Euro. None of these costs contain contingency. The costing of the water Cherenkov detector is already well understood based on our recent experience of building Super-K and the K2K 1kton detector. In other cases we have used either our best estimates or vendor/company quotations.

B.1 Facilities and Civil Construction

The costs for the facilities include the cost of excavation for the underground cavity and also all of the support surface buildings. This includes support for water purification and liquid argon storage. In addition, the costs of installation and materials for the cranes and elevators necessary to transport people and equipment in and out of the underground hall has been estimated. These costs are summarized below and are based on detailed engineering designs and quotations.

ITEM/SYSTEM	TOTAL COST
Hall Excavation/Construction	9.63 US M$
Surface Buildings	0.77
Air-Conditioning, Water and Services	0.50
Power Facilities	0.68
Cranes	0.08
Elevator	0.23
TOTAL	11.9 US M$

B.2 Water Cherenkov Detector

The detailed cost estimates for the Water Cherenkov(WC) detector are given below. All of these costs are based on previous or recent experience in building the IMB, Kamiokande, Super-Kamiokande, and K2K 1kton detectors.

B.2.1 Water Enclosure and Mechanical Support

The costs for both the materials and construction of the water enclosure of the water Cherenkov detector and also the material and construction costs for the PMT support structure of the water Cherenkov detector are detailed below. These costs are based on company quotations.

ITEM/SYSTEM	TOTAL COST
Water Enclosure	
Detailed Enclosure Design	0.04 US M$
Enclosure elements (Liner, steel plates, H beams ..)	0.15
Pre-assembly at Factory	0.06
Transportation to 2KM site	0.01
Onsite Enclosure Construction	0.40
Safety and Onsite Construction Management	0.14
PMT Support Structure	
Detailed Support Design	0.04
PMT Support Elements (Steel Beams etc)	0.13
Pre-assembly at the factory	0.08
Transportation to 2KM site	0.02
Onsite PMT support Construction	0.45
Safety and Onsite Construction Management	0.15
Single PMT Support Frame	0.20
Calibration System + Structure	0.14
TOTAL	2.00 US M$
TOTAL + 5% tax	2.10 US M$

B.2.2 PMTs and Cables

The PMTs will be purchased pre-assembled from Hamamatsu. We will supply the cables. The costs below are based on a quotation for 5660 Hamamatsu R5912MOD PMTs and their associated cables, bases and connectors.

ITEM/SYSTEM	TOTAL COST
5660 8" PMTs	3.79 US M$
5660 25m cables	0.10
5660/2 SHV connectors	0.13
TOTAL	4.02 US M$

B.2.3 Water System

The cost estimates for the 2KM WC Water purification system is based on the experience of building the IMB, K2K and Super-K water purification systems. This estimate assumes no reuse of previous equipment.

ITEM/SYSTEM	TOTAL COST
25 gpm Reverse Osmosis Unit	$ 25,500
Pre Treatment Equipment	15,500
Post Filters	15,000
Ultraviolet Sterilizers	5,000
Make up Tank System	5,000
Chiller and Heat Exchanger	50,000
Monitors and Controls	45,000
PLC Control	30,000
Install materials	60,000
Install Labor	50,000
Engineering	5,000
Estimated freight to Japan	15,000
TOTAL	0.32 US M$

B.2.4 Water Cherenkov HV System and Readout Electronics

The costs for the WC HV power supply and distribution system are given below. These costs are based on the costs for building the Super-K outer detector systems. As discussed in section 7.4.2 we envisioning duplicating the new Super-K electronics and DAQ system currently under development and estimate no more than $200/channel cost. This cost is included in the following table.

Qty	Description	Unit Cost	Total cost
4	HV Mainframe (16 slots each)	$12,760	$51,000
45	HV Module (12 channels each)	1,895	85,300
27	9U VME crate (20 cards each)	200	5,400
520	Paddle Card	345	179,400
14	Power supply for paddle cards	490	6,900
27	remote controller card (1/crate)	400	10,800
14	19" electronics rack (1/2 crates)	1,000	14,000
520	20' HV cable with SHV	60	31,200
520	12-channel custom data cables	70	36,400
1	Linux PC for control	1,500	1,500
–	Mobilization, shipping	–	2,500
5660	Custom Readout Electronics	200	1,132,000
	Total (including spares)		1.56 US M$

B.2.5 GPS System

The costs for the GPS time synchronization system required to correlate event times between the 2KM and J-PARC sites along with a fiber optic cable for fast triggering to the JPARC site are given below. Note that GPS systems for Super-K are budgeted elsewhere.

Item	Qty. req.	Unit price	Item Total	Total
Commercial equipment:				
Primary GPS Clock	1	$6,000	$6,000	
Secondary GPS Clock	2	300	600	
Ru-stabilized oscillator	1	2,600	2,600	
Fiber optic cable, 2.5km	1	3,100	3,100	
VME crate	1	3,100	3,100	
VME-PC interface	1	2,000	2,000	
Racks, Antennas, cabling	1	1,400	1,400	
Host/control Linux PC	1	1,900	1,900	
SUB-TOTAL				20,700
Custom electronics (LTC boards)				
Prototype engineering	-	-	2,800	
PCB etching, drilling	-	-	1,200	
PCB setup and testing	-	-	600	
All other parts	-	-	5,000	
Board assembly labor	400 hr	15	6,000	
SUB-TOTAL				15,600
System integration				
Integration and testing			5,600	
Mobilization, shipping			3000	
SUB-TOTAL				8,600
TOTAL				0.04 US M$

Combining the costs from all of the above tables, the total cost of the water Cherenkov detector is 8.34 US M$.

B.3 Muon Range Detector

The costs for building the MRD system are based on vendor quotes and our experiences building the K2K MRD and SciBar detector.

B.3.1 MRD Steel and support structure costs

The costs for the material, delivery and construction of the MRD steel and support structures are as follows:

ITEM/SYSTEM	TOTAL COST
Detailed MRD Support Design	0.06 US M$
Japanese Steel, inc. beams for support	0.91
Pre-assembly factory	0.23
Transportation to 2KM site	0.08
Onsite Construction Cost	0.68
Safety and Onsite Construction Management	0.42
TOTAL	2.37 US M$
TOTAL + 5% tax	2.49 US M$

B.3.2 MRD Detector Costs

The budget MRD active detector elements and electronics is based on the costs of building the K2K SciBar detector.

ITEM/SYSTEM	TOTAL COST
Scintillator	0.23 US M$
WLS Fiber	0.36
64 Channel Multi-Anode PMT	0.22
Front End Board (FEB)	0.16
ADC with FEB controller	0.13
TDC	0.01
VME Crates	0.02
HV Systems	0.09
DAQ Systems	0.01
Cables	0.03
TOTAL	1.28 US M$

Combining the costs from the structure and detector elements results in a total MRD cost of 3.76 US M$.

B.4 Liquid Argon Detector

A precise costing of the liquid argon detector is ongoing and goes beyond the scope of this document. The overall cost of the subdetector facility is currently estimated at the level of 10 Million Euros or 12.6 US M$. Precise costing will be the subject of a dedicated document.

B.5 Total Project Cost

The overall cost of the 2KM complex and detector suite is summarized in the table below. The cost of the entire project is estimated to be approximately 36 US M$.

Item	Total
Civil Construction	11.9 US M$
Water Enclosure	2.10
PMT Costs	4.02
Water System	0.32
WC HV System + Electronics	1.56
Timing System	0.04
MRD Steel	2.49
MRD Detector Elements	1.28
LAr Detector	12.6
TOTAL	36.3 US M$